# Thermoelectric property studies on nanostructured N-type Si-Ge Bulk Materials

Author: Xiaowei Wang

Boston College

The Graduate School of Arts and Sciences

Department of Physics

# THERMOELECTRIC PROPERTY STUDIES ON NANOSTRUCTURED N-TYPE Si-Ge BULK MATERIALS

a dissertation

by

Xiaowei Wang

submitted in partial fulfillment of the requirements

for the degree of

**Doctor of Philosophy**

June 2009

# THERMOELECTRIC PROPERTY STIDIES ON NANOSTRUCTURED N-TYPE Si-Ge BULK MATERIALS

by

Xiaowei Wang

Advisor: Professor Zhifeng Ren

## Abstract

SiGe alloys are the only proven thermoelectric materials in power generation devices operating above 600 ℃ and up to 1000 ℃ in heat conversion into electricity using a radioisotope as the heat source. In addition to radioisotope applications, SiGe thermoelectric materials have many other potential applications, for example, solar thermal to electricity energy conversion and waste heat recovery. However, traditional SiGe alloy material shows low ZT values of about 0.93 at 900 ℃, thus, 8% is the highest device efficiency for commercial SiGe thermoelectric devices.

Recently, many efforts have been made to enhance the dimensionless thermoelectric figure-of-merit (ZT) of SiGe alloys. Among them, the nano approach has been recognized as an effective mechanism to obtain thermoelectric materials with good performance. In this approach, dense bulk samples with random nanostructures with high interface densities are synthesized through ball milling and a direct current hot press, leading to an enhancement ZT through reduced phonon thermal conductivity. Such a practical technique produced samples of nanostructured p-type dense bulk bismuth antimony telluride with a peak ZT of 1.4 at

1000 ℃ from either alloy ingot or elemental chunks. However, the generality of this approach has not been demonstrated. Here, we applied the same technique in SiGe system in order to fabricate a nanostructured n-type SiGe alloy with enhanced thermoelectric properties.

In this thesis, numerous nanostructured n-type SiGe alloy samples were successfully pressed. The structure of these nanostructured samples was investigated via XRD, EDS, and TEM. It has been confirmed that many nano grains exist in our nanostructured samples. The thermoelectric measurements showed that the thermal conductivity of nanostructured n-type $Si_{80}Ge_{20}$ samples can be reduced to be about 2.5 W/m*K, much lower by a factor of 2 than that of the conventional bulk alloys with the same overall alloy composition, with only a relatively small reduction in the electrical conductivity, leading to a peak ZT of about 1.3 at 900 ℃. Additionally, the detailed experimental data of as-made SiGe nano samples with different Si/Ge ratio, different doping level, different press conditions, and different inclusions are discussed to determine the optimal conditions of n-SiGe nano thermoelectric material.

The second part of my thesis discusses the luminescence of a single ZnO nanowire. ZnO is a large band-gap semiconductor with several desirable properties for nanowires laser diodes and LEDs because of its high exciton binding energy. Although, extensive studies have been made on ZnO nanowires system, many of them are carried out on large numbers of nanowires simultaneously by defining a metallic contact on a thin film of nanowires. In our study, we construct the first ZnO single-nanowire light-emitting diode, which directly shows the potential of ZnO nanowires as an electroluminescent material.

## Acknowledgements

It is a pleasure to thank the many people who made this thesis possible.

First of all, I would like to express my deepest gratitude to my Ph. D. supervisor, Dr. Zhifeng Ren, for his support and advices during my graduate education. He is one of the best advisors and teachers I have ever seen. With his enthusiasm, his inspiration, and his great talent to explain things clearly and simply, he helped me in the struggle for my own understanding of thermoelectric and experimental set ups. On the personal side, he treats his students as a part of his family. When students did great research work, he felt happy in his heart. And he taught us how to be responsible men and how to work and live happily. Without him, I would have been lost in my Ph. D pursuit.

I would like to specially thank my co-worker at MIT, Mr. Hohyun Lee. It was wonderful having many fruitful discussions with him regarding measurement and theories. Also, I am glad to have the great opportunity to obtain cutting edge knowledge and advice from Prof. Gang Chen and Prof. Millie S. Dresselhaus. For every group meeting with them, I learned lots of fundamental theories and experimental skills.

I give my sincere thanks to Prof. Rein Uritam and my dissertation committee members, Prof. Michael Graf, Prof. David Broido, and Prof. Cyril P. Opeil. Their insightful opinions and extremely valuable advice for my thesis proposal are greatly appreciated.

I give my special thanks to Dr. Dezhi Wang, who helped me to solve many problems during sample preparation and his support in countless situations in the lab.

I am indebted to my many student colleagues for providing a stimulating and fun environment in which to learn and grow. I am especially grateful to Dr. Yucheng Lan, Mr. GaoZhu Hua, Mr. Giri Raj Joshi, Mr. Jian Yang. Without them, all of my samples would have ended as useless half-samples. I also owe thanks to the following people, who contributed to my daily research work: Dr. Bed Poudel, Mr. Yi Ma, Mr. Xiao Yan, Mr. Bo Yu, Mr. Hui Wang.

Lastly, and most importantly, I wish to thank my parents. They raised me, supported me, taught me, and loved me. To them, I dedicate this thesis.

Xiaowei Wang

June 2009

# Contents

| Abbreviation | Meaning |
|---|---|
| DC hot press | Direct current induced hot press |
| EDS | Energy dispersive spectroscopy |
| HRTEM | High-resolution TEM |
| IR | Infra-red |
| LED | Light emitting diode |
| PF | Power factor |
| RTG | Radioisotope thermoelectric generator |
| SAED | Selected area electron diffraction |
| SEM | Scanning electron microscopy |
| TC | Thermocouple |
| TE | Thermo-electric |
| TEM | Transmission electron microscopy |
| VLS | Vapor-liquid-solid |
| VS | Vapor-solid |
| XRD | X-ray diffraction |

| Symbol | Meaning |
|---|---|
| Z | Figure-of-merit |
| ZT | Dimensionless-figure-of-merit |
| T | Absolute temperature |
| S or α | Seebeck coefficient |
| Π | Peltier coefficient |
| b | Thomson coefficient |
| $E_f$ | Fermi energy |
| Pf | Power factor |
| σ | Electrical conductivity |
| k | Thermal conductivity |
| τ | Scattering time |
| e | Electronic charge |
| η | Device efficiency |
| μ | Mobility |
| θ | Debye temperature |
| n | Carrier concentration |
| m* | Effective mass |
| $k_L$ | Lattice thermal conductivity |
| $R_H$ | Hall coefficient |
| *q"* | Heat flux |
| λ | Wavelength |
| ρ | Resistivity |
| $t_{1/2}$ | Half time |
| α | Diffusivity |
| $C_p$ | Specific heat capacity |
| ϕ | Band bending potential |
| ε | dielectric constant |
| J | Current density |

# Lists of Figures and Tables

## Chapter 1



## Chapter 2

## Chapter 3

## Chapter 4

## Chapter 5

# List of Publications

1. "Enhanced Thermoelectric Figure-of-Merit in Nanostructured n-type Silicon Germanium Bulk Alloy", **X. W. Wang**, H. Lee, Y. C. Lan, G. H. Zhu, G. Joshi, D. Z. Wang, J. Yang, A. J. Muto, M. Y. Tang, J. Klastsy, S. Song, M. S. Dresslhaus, G. Chen, and Z. F. Ren, *Appl. Phys. Lett*., **93**, 193121 (2008)

2. "Enhanced Thermoelectric Figure-of-Merit in Nanostructured *p*-type Silicon Germanium Bulk Alloys", G. Joshi, H. Lee, Y. C. Lan, **X. W. Wang**, G. H. Zhu, D. Z. Wang, R. W. Gould, D. C. Cuff, M. Y. Tang, M. S. Dresselhaus, G. Chen, and Z. F. Ren, *Nano Letters* **8**, 4670 (2008).

3. "Increased Phonon Scattering by Nanograins and Point Defects in Nanostructured Silicon with a Low Concentration of Germanium", G. H. Zhu, H. Lee, Y. C. Lan, **X. W. Wang**, G. Joshi, D. Z. Wang, J. Yang, D. Vashaee, H. Guilbert, A. Pillitteri, M. S. Dresselhaus, G. Chen, and Z. F. Ren, *Phys. Rev. Lett.*, **102**, 196803 (2009).

4. "Nanostructured Thermoelectric Skutterudite", Q. Y. He, Q. Hao, **X. W. Wang**, J. Yang, Y. C. Lan, X. Yan, B. Yu. Y. Ma, B. Poudel, G. Joshi, D. Z. Wang, G. Chen, and Z. F. Ren, *J. Nanosci. Nanotechnol.* **8**, 4003 (2008).

5. " The great improvement effect of pores on ZT in $Co_{1-x}Ni_xSb_3$ system " , Q. Y. He, S. J. Hu, X. G. Tang, Y. C. Lan, J. Yang, **X. W. Wang**, Z. F. Ren, Q. Hao, and G. Chen, *Appl. Phys. Lett*. **93**, 042108 (2008).

6. "Chemical Thermoelectric property studies on bulk $TiO_x$ with x from 1 to 2", Q. Y. He, Q. Hao, G. Chen, B. Poudel, **X. W. Wang**, D. Z. Wang, and Z. F. Ren, *Appl. Phys. Lett*. **91**, 052505 (2007).

7. "Near-Infrared Photoluminescence in Germanium Oxide Enclosed Germanium Nano and Micro-Crystals", W. Z. Wang, K. D. Wang, D. X. Han, B. Poudel, **X. W. Wang**, D. Z. Wang, B. Q. Zeng, and Z. F. Ren, *Nanotechnology*, **18**, 075707 (2007).

8. "Broadband ZnO single-nanowire light-emitting diode", J. M. Bao, M A. Zimmler, F. Capasso, **X. W. Wang**, and Z. F. Ren, *NanoLetters* **6**, 1719 (2006).

# Chapter 1

# Introduction

Thermoelectric effects can be described as the direct conversion between thermal energy and electricity, and can be used either for cooling applications or as power generators. The first thermoelectric effect, i.e. the Seebeck effect, was discovered by Seebeck in 1821 [1], but little effort was put into the field because of the lack of high thermo power materials until Ioffe (1957) found out that semiconductor materials performed much better as thermoelectrics than metals or semimetals. As a result, thermoelectric refrigeration became practicable [2]. Since then, a tremendous amount of research activity was put into the field of thermoelectric materials, and a lot of research work on alloy based semiconductor materials was done during 1950s-1980s, in particular, on BiTe or SiGe systems [3-6]. However, after the 1980s, research on thermoelectric began to diminish due to a lack of significant achievement in further studies.

As of the 1990s, however, there has been a rebirth of interest in the field of thermoelectric materials, which were brought out by the energy crisis and environmental issues associated with traditional energy materials, especially such as oil and coal. High performance thermoelectric materials can be treated as a new alternative energy source. Compared to traditional vapor compression refrigeration or power generators, thermoelectric devices have some revolutionizing features. They are more reliable, and have a long life time

without maintenance [7]. More importantly, they have the potential to be used in many waste heat recovery applications. Waste heat recovery from automobile engines and exhaust, could help to alleviate the green house effect [8]. Over the past few decades, many efforts were made in the search for new materials or structures with phonon glass electron crystal properties, as described by Slack [9]. One such material is the skutterudites [10], such as CoSb. This class has a large unit cell and empty space inside the unit cell. This structure allows researchers to reconstruct the phonon spectrum by filling the empty space with other atoms called “rattlers”, such that phonon thermal conductivity is reduced. A very high ZT of 1.6 at 700 degree C was reported at ITS 2008. Not only new materials, but many new ideas have been proposed in the thermoelectric field. In the 1990s, a nano-approach was proposed to enhance thermoelectric performance [11-13]. By using nano-structured materials, the thermo power or electrical conductivity was enhanced due to quantum effects and energy filtering, and enhanced phonon scattering at grain boundaries still helped to reduce thermal conductivity, even if the dimension of the nano-structured materials were not in the range of quantum size effect leading to a high ZT. This theory was soon experimentally realized in superlattice $Bi_2Te_3/Sb_2Te_3$ [14] and quantum dot superlattice $PbSe_{0.98}Te_{0.02}/PbTe$ [15]. More recently, distribution of electron states was modified by adding Tl into PbTe, increasing mobility and thermo power due to energy filtering, and leading to a high ZT of 1.5 at 400 degree C [16].

Although there have been many of achievements on nano-structure based

thermoelectric materials, the fabrication technique for those nanostructures, molecular beam-epitaxy, is too expensive and not scalable for mass production. However, A detailed study on the correlation of structure and properties suggests that superlattice structure is not needed for reducing thermal conductivity, any samples with large interface densities, as in the case of superlattice, would be good enough to have low thermal conductivity [17]. Therefore, our group developed a new technique to synthesize a large quantity of nanostructured thermoelectric materials. Recently, such a practical technique for making nano-structured dense bulk samples of $Bi_{0.4}Sb_{1.6}Te_3$ with a peak ZT of 1.4 was reported. This is about 40% higher than the state of the art [18]. In this thesis, we applied the same technique to a silicon germanium system, which is extensively used in NASA spacecrafts. In this chapter, a brief review of thermoelectric phenomenon, current challenges, and our approach for thermoelectric materials with a better performance will be discussed.

## 1.1. Thermoelectric Background

When a material is subjected to a temperature gradient, an electrical potential is created across the material, because of net electron flow from the hot to the cold side. Conversely, when electrical current is passed through the material, heat is transported too. These phenomena are called thermoelectric effects. Although these effects were discovered in the early $19^{th}$ century, it took hundreds of years for researchers to realize the significance of those effects and their potential to be applied to thermoelectric generation and refrigeration.

These effects and the physical principles behind it will be briefly discussed here as an introduction.

## 1.1.1 Thermoelectric Effects

### 1.1.1.1. The Seebeck Effect

The first thermoelectric effect was discovered by Seebeck in 1821, thus called the Seebeck effect. It was found that an electric field appears when two different metals are connected, and a temperature difference is established at two junctions, as shown in Fig. 1.1.1 [3]. This effect has been used to measure temperature for over a century. It is also the principle of power generation since heat can be transferred to electricity via the Seebeck effect. However, an actual junction is not necessary for Seebeck phenomena, it is an intrinsic property of any individual material. A material that is subject to a temperature gradient generates an electrical field. For small temperature differences the relationship is linear, and the ratio of the voltage to the temperature difference is called the Seebeck coefficient S

$$S = -\frac{dV}{dT}.$$

The sign of S depends on the type of carriers, it is positive for hole carriers and negative for electron carriers.

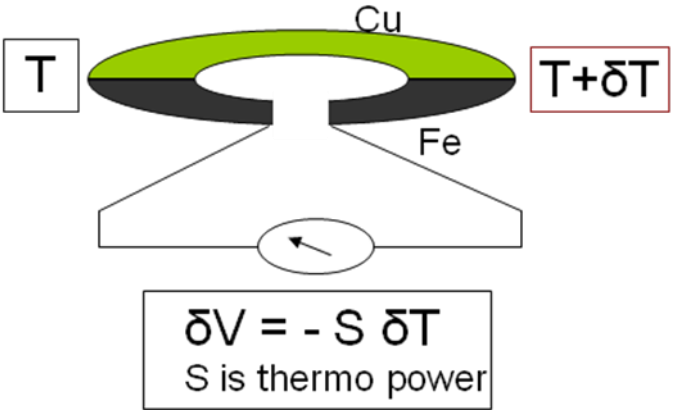


**Fig. 1.1.1.** A sketch for Seebeck thermoelectric phenomena.

The basic physical principle behind Seebeck effect is that electrons can transport thermal and electrical energy simultaneously. From a classical view, when there is a temperature difference across a conducting rod, the charge carriers at the high temperature end have a high thermal energy, and thus high velocities. This creates a net carrier flow through the conductor until there is large electrical field generated to stop the diffusion. From a modern quantum view, the Fermi level at the hot temperature side is higher than the one at low temperature side, leading to a net carrier flow until there is sufficient carrier resided at low temperature side to push the Fermi level to the same as the hot side.

The Seebeck coefficient is sometimes refered to as thermo power, since it is the basic principle of power generators. It represents the maximum electrical energy that you can obtain from a temperature gradient. This is why lots of research is being carried out to enhance the Seebeck coefficient [19-20]. However, in a real device, other thermoelectric parameters need to be optimized to obtain a better performance, which is the topic of next

few paragraphs.

#### 1.1.1.2. The Peltier Effect

In 1834, Peltier discovered another thermoelectric effect when the reverse situation of Seebeck's experiment was considered with an external emf source applied across two conductors [21]. The Peltier coefficient $\Pi_{ab}$ of a pair of materials at a junction is defined as the ratio of heat flow Q to current flow I.

$$\Pi_{ab} = \frac{Q}{I}$$

The Peltier coefficient represents how much thermal energy can be transported along with carrier flow. From a thermo dynamic view, whenever carriers pass through the junction, they must either release or absorb thermal energy from the lattice because carriers have different energy states in different materials.

Since heat is absorbed at one junction, the Peltier effect can be used to transfer heat from one junction to another; which is the principle of thermoelectric cooling. However, in a typical thermoelectric device, heat loss needs to be as small as possible. The cooling efficiency of a real device will be discussed later in this chapter.

#### 1.1.1.3. The Thomson Effect

The last of the thermoelectric effects, the Thomson effect [22] relates to the rate of generation of reversible heat q from the passage of a current through a portion of a single

conductor along which there is a temperature difference. When the difference is small, the relation is linear as shown in the following formula,

$$q = -bJ\frac{dT}{dx} \quad .$$

where *b* is the Thomson coefficient, which has same units as the Seebeck coefficient.

#### 1.1.1.4. The Kelvin Relationships

If we look carefully at these three effects, they all represent how thermal energy can be exchanged with electrical energy, so naturally there should be a relationship between these three coefficients [23]. Indeed, by using irreversible thermodynamics, the following formula can be derived

$$\Pi = S \bullet T \quad \text{and } b = \mathrm{T}\left(\frac{dS}{dT}\right).$$

As we can see, those three effects are highly related with each other, they all depend on one intrinsic thermoelectric property, i.e. Seebeck coefficient.

#### 1.1.1.5. Thermoelectric Devices

The semiconductor has two types of electrical carrier (electrons and holes). The basic component of thermoelectric device is the module, which includes p and n legs. When the majority of the carrier are holes, the material is called p-type, and conversely, when the majority are electrons, it is n-type. With one pair of p and n type material, thermal and electrical energy can be exchanged successfully, since a completed current flow circuit is

formed. Fig. 1.1.2 shows the schematic of two typical devices, a power generator and a thermoelectric cooling device, which use the Seebeck effect and the Peltier effect respectively [4].

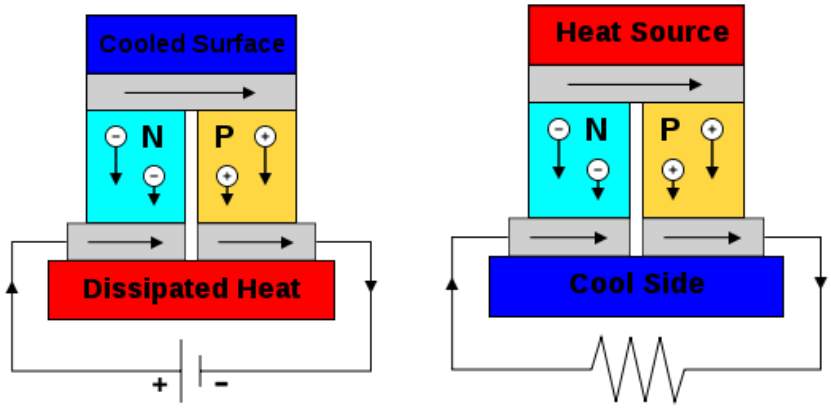


**Fig. 1.1.2**. Schematic of a thermoelectric cooler (left) and power generator (right).

Although, high thermo power is necessary for performance, in a real device, other transport properties need to be considered as well. This is because high thermo power indicates low electrical conductivity, which causes large joule heat (heat loss), leading to a low device efficiency. As a result, all thermoelectric transport properties, including electrical conductivity, and thermal conductivity must be investigated.

## 1.1.2. Thermoelectric Transport Properties

### 1.1.2.1. Electrical Conductivity

In the thermoelectric field, semiconductors are commonly used materials since so far only semiconductors have reasonable thermo power and Seebeck coefficients. The following

formula shows electrical conductivity of a typical semiconductor, when certain assumptions were made. These include isotropy, a parabolic energy band and a Fermi distribution function.

$$\sigma = \frac{e^2}{4\pi^3}\int \tau\vec{v}(\vec{k})\vec{v}(\vec{k})\frac{\partial f_0}{\partial E}d^3k$$

As we can infer from the formula, the electrical conductivity mostly depends on effective mass and relaxation time. The effective mass is the second derivative of dispersion function of the carrier around the Fermi level, which is related to the materials intrinsic properties. These include atomic mass, electron structures, crystalline structure, and artificial structures like nano-dots, quantum wells, and superlattices. Relaxation time corresponds to scattering processes, as indicated by the following:

$$\frac{1}{\tau_{total}} = \frac{1}{\tau_1} + \frac{1}{\tau_2} + \cdots \frac{1}{\tau_i}$$

where $\tau_i$ refers to the relaxation rate due to the i$^{th}$ scattering mechanism. In heavily doped semiconductors, the most important scattering mechanism is actually electron-phonon transport scattering. Depending on the temperature, different types of phonons will join the scattering process, for example, acoustic phonons at low temperatures and optic phonons at high temperatures.

#### 1.1.2.2. Seebeck Coefficient

By using quantum mechanics with some simplified assumptions, a general form for

the Seebeck coefficient can be obtained as follows,

$$S = \frac{1}{eT}\frac{\int \sigma(E)(E - E_F)dE}{\int \sigma(E)dE}\alpha(E - E_F)$$

clearly the Seebeck coefficient is proportional to the expectation value of the energy difference of the carriers around the Fermi surface. So it is interesting to point out that the Seebeck coefficient can be significantly enhanced if we can engineer the materials in a way that low energy carriers are cut off. This is called energy filter phenomena, and has been reported elsewhere [24]. For our nano approach, it will have a similar effect when the grain size is roughly equal to the Bohr radius of the corresponding materials. More recently, Ohio State University researchers have found out the electron energy spectrum of PbTe can be dramatically modified by adding Tl, so that Seebeck coefficient is almost doubled.

#### 1.1.2.3. Thermal Conductivity

When electrical carriers pass through a material, they not only transport electrical energy but also thermal energy. In addition, thermal energy can be transferred through quasi particles, i.e. phonons. Thus the total thermal conductivity is composed of two parts, one is the electrical thermal conductivity, and the other is lattice thermal conductivity.

##### 1.1.2.3.1. Electronic thermal conductivity

In most cases, the electronic thermal conductivity of a metal is proportional to

electrical conductivity, as indicated by the Wieldmann-Franz law. Hence, it is very difficult to to achieve a high ZT by modifying the electronic component of the thermal conductivity, in heavily doped semiconductors, the Wieldmann-Franz constant is lower than that of metals [25].

**1.1.2.3.2. Lattice thermal conductivity**

The usual lattice contribution to thermal conductivity can be expressed generally as the following by using the Boltzmann equation:

$$k_l = \frac{C_v V_s l}{3}.$$

Where $C_v$, $V_s$, and $l$ stand for the specific heat at constant volume, the average velocity of phonons, and mean free path respectively. From the formula, it is obvious that there are two ways to obtain low thermal conductivity. The first way is to construct the phonon spectrum in such a way that it produces a low group phonon velocity because the first brillouin zone is much smaller in nanostructure materials. The second way is to reduce the phonon mean free path by creating artificial boundaries inside the thermoelectric materials, leading to a low lattice thermal conductivity.

For good semiconductor thermoelectric materials currently employed in industry or in NASA spacecraft, the operation temperature is from room temperature to 1000 degree C. In this temperature range, the lattice thermal conductivity is still the dominant thermal transport mechanism. Thus, reducing lattice thermal conductivity is a viable option to obtain

high thermoelectric performance materials.

#### 1.1.2.4. Scattering Mechanisms in Semiconductors

In general, several scattering mechanisms may be responsible for limiting the mean-free path of the particles, i.e. reducing the lattice thermal conductivity. The net effect of various processes is usually taken into consideration by assuming the additive of inverse rates just as in the case of electrical scattering, where $\tau_i$ refers to the relaxation time due to the i$^{th}$ scattering mechanism, as shown in the following formula:

$$\frac{1}{\tau_{total}} = \frac{1}{\tau_1} + \frac{1}{\tau_2} + \cdots \frac{1}{\tau_i}.$$

The major phonon scattering processes in thermoelectric materials are phonon-phonon, phonon-electron, phonon boundary, and phonon defects scattering.

##### 1.1.2.4.1. Alloy Scattering

A proven approach to reduce thermal conductivity is through alloying, in fact, alloy scattering is a typical example of phonon-phonon scattering mechanism. Abeles et. al have described this effect both experimentally and theoretically [26]. The alloying effect is greatly enhanced in alloys where all the components have similar crystal structures. For example, in SiGe alloy materials, lattice thermal conductivity is reduced by almost an order of a magnitude by this mechanism compared to pure Si or Ge.

#### 1.1.2.4.2. Phonon Boundary Scattering

Boundary scattering is also an important scattering mechanism in semiconductor thermoelectric materials. Although boundaries may also scatter electrons, and thus lower the mobility, overall, the thermal conductivity reduction outweighs the loss of electrical conductivity due to lower mobility, leading to a further enhancement of the performance of thermoelectric materials.

In general, boundary scattering relaxation time is expressed as the following

$$\frac{1}{\tau_B} = \frac{\nu}{D}(1-p).$$

where D is the grain diameter, $\nu$ is the group velocity of the phonon, $p$ is a parameter which describes the possibility of undergoing specular scattering at the interface, and 1-p stands for the probability of the phonon that undergoes diffusive scattering.

For a SiGe system, the mean free path for electrons and phonons are different, they are in the range of 5-10 nm and 10-500 nm respectively for heavily doped materials at room temperature. Thus only when the typical grain sizes are down to 10-20 nm, a significant improvement can be observed. Research has shown that when the grain size is down to micro size, even though thermal conductivity is reduced by 40%, the electrical conductivity drops by about 35%, which leads to only a slightly better thermal performance [27].

### 1.1.2.5. Thermoelectric Device Efficiency

A thermoelectric converter is a heat engine which obeys the laws of thermo-dynamics. Here, we only consider the ideal case, i.e. no heat loss. The efficiency of a thermo device is defined as the ratio of output energy to the input energy of the system. More specifically, the efficiency of a thermoelectric generator is defined as the ratio of the electrical power delivered to the load to the heat absorbed at the hot junction. The performance of any thermoelectric refrigerator is expressed by the cooling power produced divided by the rate at which electrical energy is supplied.

In the case of a generator, Ioffe (1957) showed the highest efficiency is given by

$$\eta = \frac{(T_H - T_C)}{T_H} \frac{(1+ZT)^{1/2} - 1}{T_C / T_H + (1+ZT)^{1/2}}$$

where T is taken to be average temperature of the device, i.e. the mean temperature of the hot and cool sides. The first part is actually the efficiency of an ideal Carnot machine and it is essentially the upper limit for any thermal device. The quantity Z is given by $Z = \frac{S^2\sigma}{K}$, where S is the Seebeck coefficient, $\sigma$ is the electrical conductivity. Similarly, the optimized performance of a thermoelectric refrigerator is expressed as the following,

$$\Phi = \frac{T_C[(1+ZT)^{1/2} - T_H / T_C]}{(T_H - T_C)[(1+ZT)^{1/2} + 1]}.$$

It is obvious from those two formulas that the performance of any thermoelectric device is directly related to one inherent property of the materials of the legs. This property is called the dimensionless figure of merit, ZT. Fig. 1.1.3 shows plots of efficiency versus the

dimensionless figure of merit for thermoelectric generators corresponding to fixed a $T_h/T_c$ value of 2. Clearly, a high ZT gives a better performance. But this value has increased by only a few percent from the 1950s until the 2000s, when new concepts, like quantum structures, and new materials, like skutterudites, were introduced. Our group has developed a simple and cost-effective method to greatly enhance the figure of merit of existing thermoelectric materials, which was first realized on a BiSe-BiTe system. Now we are trying to extend the same approach to a Si-Ge system, another commonly used thermoelectric material, especially in high temperature ranges. This is the major topic of this thesis.

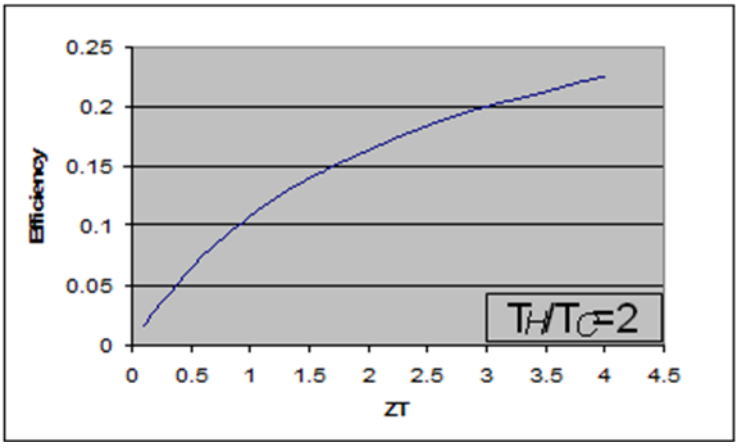


**Fig. 1.1.3.** Theoretical power generator efficiency as a function of ZT.

### 1.1.2.6. Thermoelectric Figure of Merit

As we have discussed, the performance of any thermoelectric device is mainly dependent on one parameter, called the dimensionless figure of merit ZT, defined as, $Z = \frac{S^2\sigma}{K}$, where S is the Seebeck coefficient, $\sigma$ is the electrical conductivity, k is the

thermal conductivity, often dominated by the contribution from the lattice vibration, and T is the operation temperature.

If we examine the above formula carefully, good thermoelectric materials require a high Seebeck coefficient (more power can be generated through a temperature gradient), a high electrical conductivity (less joule heating loss), and a low thermal conductivity (less thermal leakage from hot to cool side). However, in bulk materials, all of the three thermoelectric properties are related to each other, so it is very difficult to enhance one property without affecting others. For example, increasing the carrier concentration not only enhances the electrical conductivity, but also thermal conductivity. Also, the Seebeck coefficient is inversely proportional to carrier concentration. Fig. 1.1.4 is an illumination of the three properties as a function of carrier concentration [4]. It is clear that metals have the highest electrical conductivity, but also highest thermal conductivity and low Seebeck coefficients [28]. On the other hand, insulators have very low thermal conductivity and their electrical conductivity. So far, the best thermoelectric materials are found in semiconductors. An advantage of semiconductors is that the carrier type can be easily changed by adding different doping agents. In addition, because the contribution of electrons to thermal conductivity is not large in semiconductors, a change in doping concentration has little effect on thermal conductivity.

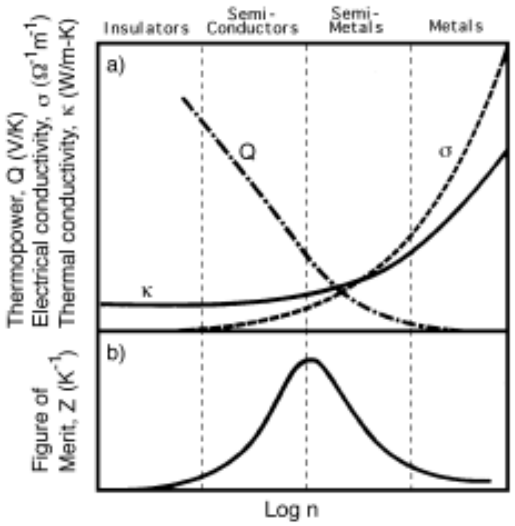


**Fig. 1.1.4.** Thermoelectric properties as a function of carrier concentration.

## 1.2. Thermoelectric Materials

In order to carry out a systematic search of good thermal materials, the three transport parameters need to be expressed by more fundamental properties, such as, energy gap, carrier concentration, effective mass, relaxation time or scattering parameters, and so on. For example, in 1986, Goldsmid found that a good thermoelectric material should has a high value of β, as defined by the following formula $\beta = (\frac{k}{e})^2 \frac{\sigma_0 T}{\lambda_L}$ [28], where $\sigma_0 = 2e\mu(\frac{2\pi m^* kT}{h^2})^{3/2}$. This shows that the preferred semiconductors for thermoelectric materials are those with high carrier mobility, large effective mass, and low lattice conductivity. It is also necessary that their energy gap be large enough for the concentration

of the minority carriers to be negligible in the operation temperature range when the Seebeck coefficient is optimized.

One of the most useful rules for selecting thermoelectric materials has been based on the observation that the lattice thermal conductivity falls with increasing mean atomic weight. However, there is a tendency for semiconductors of high atomic weight to have large mobility, which are often associated with small values for the energy gap. Thus some high atomic weight materials are satisfactory for use in thermoelectric refrigeration but cannot be used at the higher temperatures that are usually employed in thermoelectric power generation. A good example is bismuth telluride alloyed with antimony telluride or bismuth selenium or both.

Bismuth telluride is a semiconductor with a relatively small energy gap of about 0.15 eV. This allows the Seebeck coefficient to reach a value of 260 or 300 S/m at room temperature when appropriate doping agents are added. The thermal conductivity of the optimized materials is of the order of 2, of which about 1.5 is due to the lattice contribution. However, lattice conductivity can be reduced when a solid solution, or an alloy, is formed. For p-type $Bi_{0.5}Sb_{1.5}Te_3$, the lattice contribution falls to below 1 while power factor, which is defined as $Pf = S^2\sigma$, is increased, and a similar improvement was found in n type alloy $Bi_2Te_{2.7}Se_{0.3}$ too. So far, the commercial BiSe or BiTe materials can reach a ZT value of about one.

At temperatures (300 $^oC$) that are just above those for which BiTe can be used, the

preferred materials are based on lead telluride PbTe, Ioffe first studied this material for thermoelectric applications in 1957 [2], PbTe has a high mean atomic weight and a multi-valley band structure, which can provide a large Seebeck coefficient in excess of 300 S/m. Both p-type and n-type samples can be produced either by making a non stoichiometric compound or by adding metals as acceptors or halogens as donors. Also recent development on PbTe suggest that when adding Tl into PbTe, the electron energy spectrum can be changed. A sharp peak appears in the electron density of states curve. Thus, the Seebeck coefficient was greatly enhanced, leading to a ZT value of 1.5, which is about 50% higher than that of commercial PbTe.

In the middle temperature range, another type of promising thermoelectric materials, called skutterudites, has emerged as prospective candidates for achieving figures of merit well in excess of one [29]. A realistic prospect of a significant reduction in the lattice thermal conductivity has attracted great attention. The basic binary skutterdite has 2 empty positions in its crystal unit cell, which allows researchers to add different materials to reduce thermal conductivity. In most cases, materials with high atomic weights were used as fillers. Recently, Prof. Jihui Yang and other researchers found the thermal conductivity can be further reduced by filling two types of atoms into the skutterdite, thus the phonons in nearly the whole phonon spectrum range can be scattered, leading to even lower thermal conductivity [30].

At temperature ranges above 600 $^{o}$C, only silicon germanium is a proven thermoelectric material. Compared to pure silicon and germanium, the lattice thermal

conductivity of SiGe alloy falls by an order of magnitude because of alloy scattering. SiGe based thermoelectric modules have been extensively used in the radioisotope thermoelectric power generators for space missions, although ZT values for practical SiGe materials is below 1. As a summary, Fig. 1.2.1 shows the ZT values for the state-of-the-art thermoelectric materials [7].

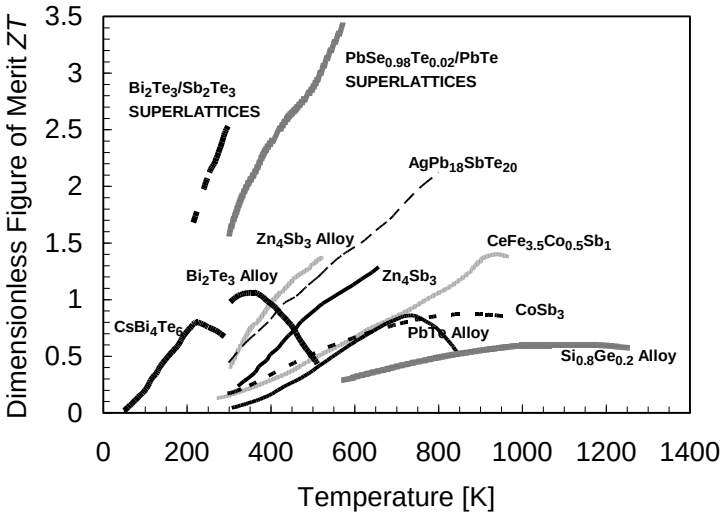


**Fig. 1.2.1.** Temperature dependence of ZT values of state-of-the-art thermoelectric materials.

## 1.3. New Developments

Tremendous efforts have been made in thermoelectric materials research from the late 1950s to 1970s after Ioffe first proposed the investigation of semiconductor materials for application in the thermoelectric field. However, by the 1980s, research on thermoelectric materials almost vanished because of a lack of progress. Until the 1990s, there has been a rebirth of interest in the thermoelectric field because of a new class of materials and new

concepts.

The best thermoelectric materials can be summarized as “phonon-glass electron-crystal”, which means that the materials should have a low lattice thermal conductivity as in a glass, and a high electrical conductivity as in crystals. There are two ways to enhance the thermoelectric performance, i.e ZT. One is to increase the power factor. For example, when quantum structures are used, Prof. Dresselhaus proposed that a high thermo power or high mobility could be obtained due to enhanced density of states, leading to high ZT [11-12]. Soon it was experimentally confirmed that in BiTe/BiSe supperlattice [14], ZT can be increased from 1 to 2.5, and in PbTe supperlattices [15], ZT can be greatly enhanced from 0.7 to 3. Recently the Hack group found that the thermo power could be greatly increased by adding Tl into PbTe. Another approach is to reduce the thermal conductivity through various new concepts, for example, Si/SiGe supperlattice shows lower thermal conductivity because of boundary scattering [13]. More recently, researchers demonstrated that silicon nanowires with rough surfaces have a tremendously lower lattice thermal conductivity of 1.2 W/m*K, which is almost close to the amorphous limit of Si system [31-32].

Another approach is to reduce the thermal conductivity through various new concepts, for example, Si/SiGe supperlattices show lower thermal conductivity because of boundary scattering [13]. More recently, researchers demonstrated that silicon nanowires with rough surfaces have a lower lattice thermal conductivity of 1.2 W/m*K, which is almost

close to the amorphous limit of the Si system [31-32].

In bulk materials, the major concept developed is the use of “phonon rattlers” to reduce the thermal conductivity. These phonon ratters are normally interstitial atoms inserted into empty spaces in the host materials. Because of different atomic weights, those rattlers will scatter the phonons in the original lattices. In this manner, several classes of new materials have been discovered or re-investigated, notably skutterudites and clathrates. By adding Yb or Ba into basic binary skutterudites, ZT values can reach 1.3, which is about twice of the ZT value of original skutterudites [33].

## 1.4. Our approach

As discussed in the previous sections, in low dimensional systems, for example, in BiSe/BiTe or Si/SiGe superlattice, the enhancement of ZT mainly comes from the reduction of thermal conductivity. There are two main explanations for the reduction of thermal conductivity in low dimensional systems. The first treats phonons as quasi particles. Low dimensional nano-systems modify the spectrum of the original phonons in corresponding bulk materials, leading to a low phonon group velocity. However, experimental results show a larger decrease in thermal conductivity than simulation results. So modulation of phonon spectrum alone cannot explain the reduction of thermal conductivity in low dimensional systems. Another explanation is that the reduction of thermal conductivity is a classic size

effect. This suggests that reduction mainly comes from phonon scattering at enhanced boundaries. Phonons can be easily scattered away when the size of nano-structure is in the range of the wavelength of phonons. On the other hand, the electrical conductivity is not significantly affected by boundary scattering since the wavelength for electrons is in the range of several nanometers, which is much larger than the boundary roughness. Using an approach that incorporates partially diffuse and partially specula interface scattering, modeling studies match well with experimental results. Hence, the critical factor for reduced thermal conductivity is the increased number of boundaries which scatter more phonons than electrons.

Although, a high ZT has been realized in superlattice or nanowire systems, there is a disadvantage for low dimensional systems. This lies in the fact that the fabrication technology is too expensive for large scale production, which is an important consideration for industrial application. So, a new approach is required to produce thermoelectric materials with enhanced boundaries at low cost for large scale production.

Our group has developed a cost and time effective method to produce materials with large boundary densities. By using a ball milling method, nano powder was produced. Followed by a direct current hot-press, a bulk sample with lots of nano grains was created. Such a practical technique for making samples of nanostructured p-type dense bulk bismuth antimony telluride with a peak ZT of 1.4 at 100 C, from either alloy ingot or elemental chunks was reported. However the generality of this approach has not been demonstrated.

Even though extensive work has been done pursuing small grained SiGe alloy to reduce thermal conductivity, it was found that when the grain size is reduced below microns, accompanying the thermal conductivity reduction is a similar reduction in electrical conductivity leading to a degradation of ZT. For P-type SiGe, a grain-size in the range of 2-5 micrometers was found to be optimal with a maximum of 20% improvement in ZT, leading to a ZT increase from 0.5 to 0.6. For n-type SiGe, no improvement in ZT was ever observed. In our project, we are trying to produce nano grains in order to maintain the same level of electrical conductivity as bulk samples while reducing thermal conductivity, specifically, phonon conductivity.

The major goal of my work is to apply the nano approach to n-type SiGe materials, and also to understand the underlying physics on these new nano-structured SiGe materials. Experimental results will be included in Chapter 2 and 3 for nano-structured SiGe samples. Chapter 2 deals with the characterization of our nano sample, including structure property and measurement of thermoelectric properties. Chapter 3 discusses the synthesis of SiGe nano powder and the consolidation of such powder. Chapter 4 presents optimization of n-type SiGe nanosamples, as is experimental data regarding the introduction of heavy impurities into n-type SiGe nanomaterials.

The second part of my thesis deals with the luminescence of a single ZnO nanowire. ZnO is a large band-gap semiconductor with several desirable properties for nanowires laser diodes and LEDs [34]. In particular, the high exciton binding energy, the result of the strong

coulomb interaction between electrons and holes, causes an enhancement of radioactive transition rate in the ultraviolet part of the spectrum. Furthermore, the electronic and optical properties of ZnO nanowires can be easily tailored by altering the growth conditions. In addition, a single ZnO nanowire can form a resonant cavity with two naturally faceted hexagonal end faces acting as reflecting mirrors. Although, extensive studies have been made on ZnO nanowires system, many of them are carried out on photoluminescence and electroluminescence properties of large numbers of nanowires simultaneously by defining a metallic contact on a thin film of nanowires [35]. In our project, we construct the first ZnO single-nanowire light-emitting diode (LED), which shows the potential of ZnO nanowires as an effective electroluminescence material.

## 1.5. References


1. T. J. Seebeck, *Magnetizche Polarization der Metalle und Erzedurch Temperatur-Differenz,* Abhand Deut. AKAD. Wiss. Berlin, 265 (1822).
2. A. F. Ioffe, *Semiconductor Thermoelements and Thermoelectric Cooling*, Infosearch, London, 1957.
3. H. J. Goldsmid, *Thermoelectric Refrigeration*, Plenum Press, New York, 1964.
4. *CRC Handbook of Thermoelectrics,* edited by D. M. Rowe, CRC Press, Boca Raton, FL, 1995, 157.
5. C. M. Bhandari, D. M. Rowe, Contemp. Phys **21**, 219 (1980).
6. C. B. Vining, *J. Appl. Phys*. **69**, 331 (1991).
7. M. Dresselhaus, G. Chen, M. Tang, R. Yang, H. Lee, D. Z. Wang, Z. F. Ren, J. P. Fleurial, and P. Gonga, *Adv. Mater*. **19**, 1 (2007).
8. J. Lagrandeur, D. Crane, and A. Eder, Deer Conference, Chicago, 2005.
9. G. A. Slack, M. S. Hussain, *J. Appl. Phys.* **70**, 2694 (1991).
10. B. C. Scales, D. Mandrus, and R. K. Williams, *Science*, **34**, L19 (2005).
11. Hicks, L. D.; Dresselhaus, M. S. *Phys. Rev. B* **47,** 16631 (1993).
12. Hicks, L. D.; Dresselhaus, M. S. *Phys. Rev. B* **47**, 12727 (1993).
13. G. Chen, *Phys. Rev. B* **57**, 14958 (1998).
14. R. Venkatasubramanian, E. Siivola, T. Colpitts, and B. O'Quinn, *Nature*, **413**, 597 (2001).

15. T. C. Harman, P. J. Taylor, M. P. Walsh, and B. E. LaForge, *Science*, **297**, 2229 (2002).

16. J. P. Heremans, V. Jovovic, E. S. Tobere, A. Saramat, K. Kurosaki, A. Charoenphakdee, S. Yamanaka, G. J. Snyder, *Science*, **321**, 554, (2008).

17. G. Chen, 2001 "Phonon Heat Conduction in Low-Dimensional Structures," Semiconductors and Semimetals, Recent Trends in Thermoelectric Materials Research, Vol. 71, pp. 203-259, Ed. T. Tritt, Academic press, San Diego.

18. B. Poudel, *et al. Science*, **320**, 634 (2008).

19. J. P. Heremans, C. M. Thrust, and D. T. Morelli, *J. Appl. Phys*, **98**, 60703 (2005).

20. O. Yamashita, H. Odahara, *J. Mater. Sci.* **41**, 7437 (2006).

21. J. C. Peltier, *Ann. Chem.*, LVI, 371, (1834).

22. W. Thomson, *Proc. Roy. Soc. Edingburgh.* 91 (1851).

23. H. Resis, J. M. Koper. Cronin, *J. Phys. Chem.*, **99**, 7837 (1995).

24. J. P. Heremans, C. M. Thrush, and D. T. Morelli, *Physical Review B*, **70**, 115334 (2004).

25. G. D. Mahan, and M. Bartkowlak, *Appl. Phys. Lett.* **74,** 953 (1999).

26. B. Abeles, D. S. Beers, G. D. Cody, and J. D. Dimukes, *Physical Review,* **152,** 44 (1962).

27. C. B. Vining, W. Laskow, J. O. Hanson, V. D. Beck, P. D. Gorsuch, *J. Mater. Chem.* **69**, 4333 (1990).

28. H. J. Goldsmid, *Electronic Refrigeration*, London 12**2** (1986).

29. Heikes, P. R.; Ure, R. W. *J. Thermoelectricity: Science and Engineering; interscience:* New York, P.20 (1961).

30. J. H. Yang, D. Zhang, S. Q. Bai, Z. Mei, and L. D. Chen, *Appl. Phys. Lett.* **90**, 192111 (2007).

31. Cu-nanofluid paper, submitted to JAP.

32. S. U. Son, I. K. Park, J. Park and T. Hyeon, *Chem. Commun.* 778 (2004)

33. Internal Research Results.

34. Y. Huang, and C. M. Lieber, *Pure Appl. Chem.* **76**, 2051 (2004).

35. R. Konenkamp, R. C. Word, and M. Godinez, *Nano Lett.* **5**, 2005 (2005).

# Chapter 2

# Characterization of Thermoelectric Materials

## 2.1. Introduction

For thermoelectric materials research, in order to characterize the thermoelectric performance, one must accurately measure the thermoelectric properties of bulk materials at different temperatures [1-3]. These properties include electrical conductivity, Seebeck coefficient, the thermal conductivity, and more fundamental parameters, such as carrier mobility and carrier concentration (both by hall measurement).

One important aspect of accurate measurements is the contact issue [4]. For the electrical conductivity measurement, an excellent electrical contact to the material is essential. For the measurement of the Seebeck coefficient, in addition to good electrical contact, excellent thermal contact is required to obtain accurate voltage and temperature data. Thus the material of the thermocouple and the buffer layer between the sample and thermocouple need to be carefully chosen to prevent any Seebeck voltage padding from the wires of thermal couple or the buffer materials. For thermal conductivity measurements, there are several measurement techniques, including the radial flow method, laser flash method, and the pulse-power method. For each method, careful experimental procedures are needed. For example, laser flash technique requires a thin coating of graphite to the sample surface in

order to obtain uniform adsorption of the laser light on the sample surface. If good adhesion is not achieved, this coating procedure can potentially be a source of significant error.

Another mistake that is often made results from calculating ZT using values of the various thermoelectric properties as measured from different samples. Thermoelectric materials have been proven notoriously inhomogeneous even among samples taken from the same batch or process. Therefore it is best to take all measurements on the same sample. In addition, in order to eliminate sample deterioration effects, such as, precipitation of phosphorus in n-type SiGe [5], a reset process needs to be done before any measurement. In a typical reset process, the sample was annealed at 1050 degree C for 15 minutes in an oven without any gas flow.

In general, electrical and thermal transport properties of thermoelectric materials can be very dependent on crystallographic directions. In certain cases they can vary by orders of magnitude. Thus, when working with single crystals or oriented polycrystalline materials it is important to measure thermoelectric properties in the same direction, or to make sure there is a little effect of crystal orientation on thermoelectric properties. When possible, it is also better to measure more than one sample of a given material.

In our measurements, we use commercially available equipment (ZEM-3) to measure electrical conductivity and Seebeck coefficient simultaneously from room temperature up to 900 degree C. Thermal conductivity is measured by using commercial laser flash equipment (Netzch Instruments). Carrier concentration and carrier mobility are

measured by commercial Hall measurement system (Lake Shore Cryotronics, Inc). All will be summarized in this chapter.

For nano-structured samples, microstructure plays an essential role on thermoelectric properties. Therefore, transmission electrons microscopy (TEM) equipment is used to characterize the microstructure of the materials. In addition, a build-in energy dispersive spectroscopy (EDS) system is applied to detect the composition of alloyed thermoelectric materials.

## 2.2. Structure Characterization

In the thermoelectric field, many potential materials are semiconductor alloys, such as BiSe/BiTe, and Si/Ge. Thus, it is very important to detect when the alloy process is complete. Here the XRD spectrum is applied to check the alloy process. As we wrote in the previous chapter, Mechanical alloy powder was made through ball milling [6]. During the ball milling process, separate peaks from individual elements in solid solution will merge into one single peak. A typical XRD spectrum of SiGe alloy powder after 25 hrs ball milling is shown below (Fig. 2.2.1). Clearly after 25 hrs high energy ball milling at 1080 rpm, only SiGe alloy peaks appear in the spectrum.

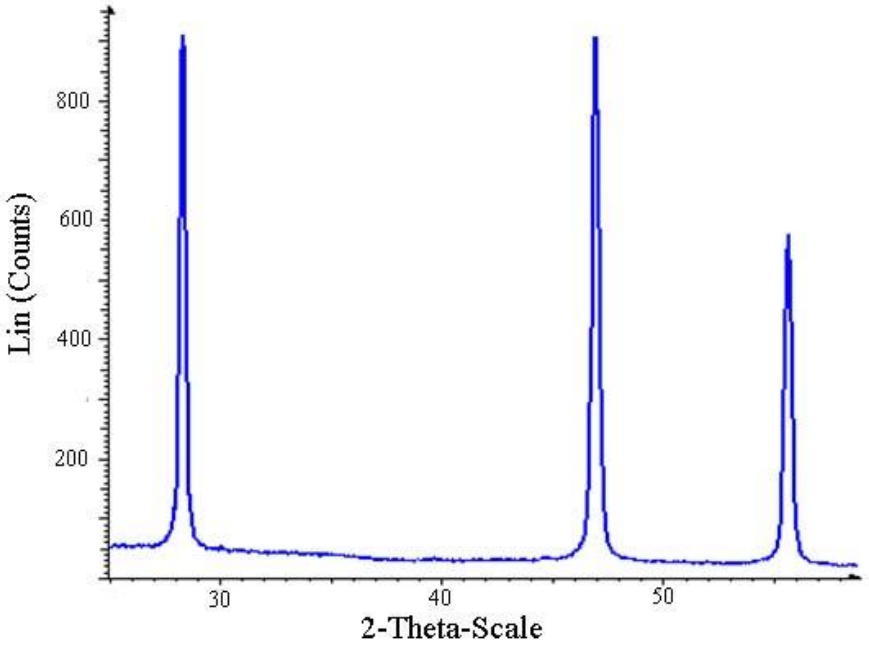


**Fig. 2.2.1.** A typical XRD spectrum of SiGe alloy powder

There is another important aspect of XRD technique. In 1956, Williamson proposed that the peak position and peak angle contains the information about the average grain size and the stress inside the grain if any [7]. This is shown in the following formula, $\beta\cos\theta/\lambda = 1/d + \xi 2\sin\theta/\lambda$, where $\beta$ is the spectral integral breadth of the diffraction peaks, $\Theta$ is the bragg diffraction angle, $\lambda$ is the incident x-ray source wavelength, which is 1.54 Å, $d$ is the average grain size and $\xi$ the lattice stress in the sample. For the size calculation, we plot $\beta\cos\theta/\lambda$ vs. $2\sin\theta/\lambda$, and then obtain the average grain sizes from the intercept on the y-axis. The slope represents the strength of the stress in the sample.

Although the XRD spectrum can provide average grain size information, if more detailed structure information of individual grain is needed, TEM is useful. This technique

can provide information on the microstructure of the sample, such as the uniformity of size of grains, crystal orientation of each grain, and the structure of grain boundaries. For our project, field emission TEM from JEOL was used to investigate structure properties of SiGe alloys. In addition, a build-in EDS system was applied to check the composition of the alloy samples.

## 2.3 Electrical Conductivity Characterization

In general, the four probe method is one of the most widely used technique for the measurement of the resistivity of a semiconductor. For thermoelectric materials, this is a challenge, because a temperature gradient between two current probes is generated when an electrical current is passed, which will produce an additional $V_o$ [8]. In order to minimize the effect of the Seebeck induced voltage, the measurement should be made relatively fast. In addition, by switching the current direction, one can subtract out the Seebeck voltage. Therefore either AC or fast switching DC current is required. There are also other issues related to an accurate determination of correct voltage. These include oxide layers, non-ohmic contact, etc. Therefore, polishing needs to be done before the sample is inserted into the measurement chamber. We have measured electrical conductivity using two independent methods in order to confirm the results. These two are: (1) a commercial ZEM-3 system, (2) a Hall measurement system which will be described in the following sections.

### 2.3.1 Electrical Conductivity Measurement (ZEM-3)

In our project, a high-speed and high-resolution current switching DC measurement

equipment, ZEM-3 (Ulvac, Inc.) is utilized to determine electrical conductivity. Fig. 2.3.1 provides a simple sketch of the method used for the electrical measurement and Fig. 2.3.2 shows a picture of an actual sample mounted on the sample holder. The sample holder is surrounded in an isothermal nickel radiation can to provide a relatively uniform temperature environment and shorten the time it takes for the sample to reach thermal equilibrium. The nickel can and the sample holder are enclosed in a furnace, which is heated by infrared light during measurement. Helium gas is loaded at 10 kPa absolute pressure in order to provide the thermal media to transport heat across the sample. As shown in the Fig. 2.3.2, the sample is held in place by two jaws with moderate pressure. The lower jaw contains an electrical resistance heater to generate a temperature gradient across the sample for Seebeck measurement and a constant current passes from the upper jaw to the lower jaw, and the voltage is measured by two probe thermocouples which are held against the sample by a light spring force. Good alignment provides a uniform and constant force will be uniformly applied to the sample from the two thermocouples. The two thermal couples are of chrome-alume (Type K) and use two channels of a Keithley 2010 digital multi-meter. The chrome leads are used to measure the voltages of two probes.

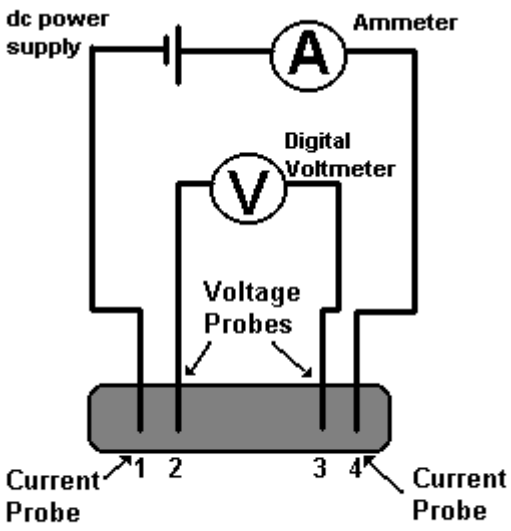


**Fig. 2.3.1**. Schematic of four probe electrical conductivity measurement.

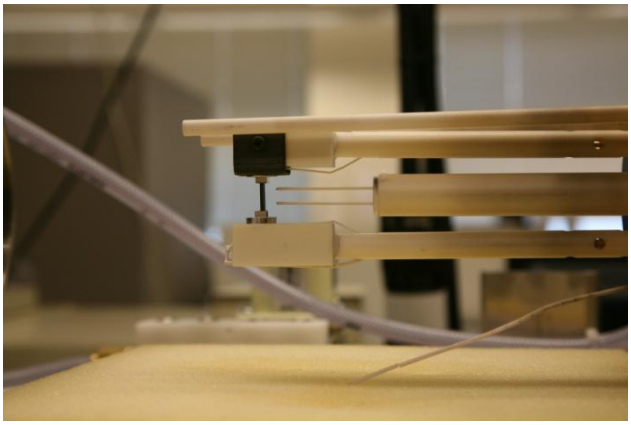

**Fig. 2.3.2.** A picture of a sample mounted in ZEM-3 unit.

The principle behind the electrical conductivity measurement is the four probe current switching method [9]. Electrical current is injected from top or bottom electrodes and passed through the whole sample as the voltage is obtained by two probes as shown in

Fig.2.3.2. A V-I plot before the measurement is used to check the contact. If a linear plot and small contact resistance are recorded, the measurement may start, otherwise, proper adjustments must be made. Data acquisition and analysis are fully processed by the software. From the plotted V-I curve, resistance is determined at various temperatures of interest, and is converted to resistivity with the help of the sample dimension. In order to eliminate the small steady state Seebeck voltage, two measurements are taken under opposite current polarity. In addition, fast current injection and fast voltage measurement is utilized to minimize the voltage by a transient temperature differential.

It is worth noting that initially as there is no equipment in ZEM-3 unit to actually measure the distance between the two probe thermocouples, and we assumed it is 6 mm. Over time, this actual distance varied significantly. Sometimes the deviation was about 0.5 mm, which increased uncertainty to about 10%. Therefore an optical camera was installed to measure the probe distance before the actual measurement.

### 2.3.2. Hall Measurement

As we explained in the previous chapter, the power factor of a thermoelectric material varies significantly with carrier concentration. Thus it is necessary to measure the carrier concentration by a Hall measurement [10]. When a current carrying conductor is put into a magnetic field, the Lorentz force deflects moving charge carriers to one side of the sample and generates an additional electric field perpendicular to both the current direction

and the magnetic field. From the measurement data, the hall coefficient, which is the ratio of the perpendicular electric field to the product of current density and magnetic field, and the resistivity are calculated, thus carrier mobility is obtained as well, which is the product of the hall coefficient and electrical conductivity. In our project, a commercial Hall measurement 7604 from Lake Shore Cryotronics was also applied to measure carrier concentration and carrier mobility.

#### 2.3.2.1 Hall Measurement Theory

In general, there are two commonly used sample geometries: (1) long, narrow Hall geometries and (2) nearly square or circular van der Pauw geometries. In both types, a Hall voltage is developed perpendicular to the current and the applied magnetic flux.

Hall bar geometries: The hall voltage developed across the sample with contacts numbered as shown in Fig. 2.3.3, is:

$$V_h=V_{24}=R_HBI/t$$

where $V_{24}$ is the voltage measured between the opposing contacts numbered 2 and 4, $R_H$ is the Hall coefficient of the material, B is the applied magnetic flux density, I is the current, t is the thickness of the sample. The Hall coefficient is complicated for a two-carrier system. However, in heavily doped semiconductor (as in the case of good thermoelectric materials), only one type carrier is dominant. For a single carrier system, the Hall coefficient can be expressed by $R_H=1/ne$ [11]. After obtaining the Hall coefficient, together with resistivity, the carrier mobility can be calculated by $R_H/\rho$. The electrical resistivity can be measured by

applying a current between contacts 5 and 6 of the sample shown in Fig.3.3.3 and measuring the voltage between contacts 1 and 3, then using the formula: $\rho(B) = \frac{V_{13} wt}{I_{56} b}$, where w is the width , t is the thickness, and b is the distance between contacts 1-3. Although, the Hall bar is a good geometry for making resistance measurement, it is really difficult to make good voltage measurement contacts, and various techniques are needed to negate the contact effect and the Etiingshausen Effect [12]. To avoid these disadvantages, we choose Van Pauw geometry method.

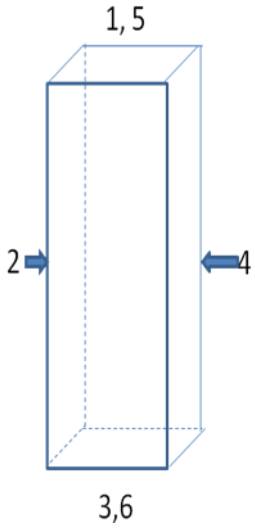


**Fig. 2.3.3**. Bar geometry for Hall measurement.

Van der Pauw geometry: Perfect Van der Pauw sample geometry is shown in Fig. 2.3.4, the resistivity of a Van der Pauw sample is given by the expression:

$$\rho = \frac{\pi t}{\ln(2)} \frac{V_{43}}{I_{12}} + \frac{V_{14}}{V_{23}}.$$

For the Hall coefficient, the same expression is used as in the case of the Hall bar geometry.

Only four contacts are required, which makes it easy to use pressure contact. There is no need to measure sample widths or distances between contacts, which are common sources of errors in the case of the hall bar geometry. Although the clover-leaf is the preferred hall geometry, the circle geometry is sufficient enough to obtain reliable data and it is much easier to make such specimens.

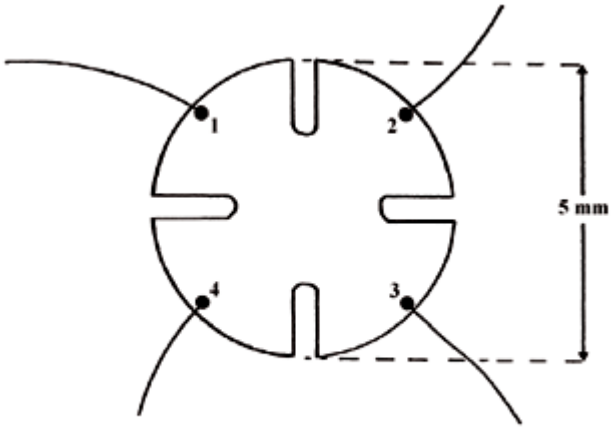


**Fig. 2.3.4.** A schematic of perfect Van der Pauw sample geometry.

### 2.3.2.2 Van der Pauw Measurement

The Van der Pauw structure is probably the most popular Hall measurement geometry, primarily because it requires fewer geometrical measurement of the sample. In 1958, Van der Pauw solved the general problem of the potential in a thin conducting layer of arbitrary shape [13]. His solution allowed Hall and resistivity measurements to be made on any sample of uniform thickness, provided that the sample was homogeneous and there were

no holes in it. In Van der Pauw technique, two voltage readings are required as explained in last section.

In the Fig. 2.3.4, the four contacts made to the sample are numbered counter-clockwise in the ascending order when the sample is viewed from above with the magnetic field perpendicular to the sample and pointing toward the observer. First, the two resistivities are calculated as following:

$$\rho_A = \frac{\pi f_A t}{\ln(2)} \left( \frac{V^+_{12,43} - V^-_{12,43} + V^+_{23,14} - V^1_{23,14}}{I^+_{12} - I^-_{12} + I^+_{23} - I^-_{23}} \right)$$

$$\rho_B = \frac{\pi f_B t}{\ln(2)} \left( \frac{V^+_{34,21} - V^-_{34,21} + V^+_{41,23} - V^1_{41,23}}{I^+_{34} - I^-_{34} + I^+_{41} - I^-_{41}} \right).$$

Here $V^+_{ijkl}$ indicates a voltage measured across terminal *k* and *l*, with *k* positive while a positive current flows into terminal *i* and out of terminal *j*, $f_A$ and $f_B$ are geometrical factors, determined by resistance ratios $Q_A$ and $Q_B$ respectively, as shown in the following formula,

$$Q_A = \left( \frac{V^+_{12,43} - V^-_{12,43}}{I^+_{12} - I^-_{12}} \right) \left( \frac{I^+_{23} - I^-_{23}}{V^+_{23,14} - V^-_{23,14}} \right)$$

$$Q_B = \left( \frac{V^+_{34,21} - V^-_{34,21}}{I^+_{34} - I^-_{34}} \right) \left( \frac{I^+_{41} - I^-_{41}}{V^+_{41,23} - V^-_{41,23}} \right).$$

If $Q_A$ and $Q_B$ are greater than one, then use the reciprocal instead. The relation between *f* and *Q* is expressed by the transcendental equation, which can be solved numerically. The two resistivities should agree to within 10%, if they do not, then the sample is too inhomogeneous, or anisotropic or has other problem. If they do agree, the average resistivity is given by $\rho = \frac{\rho_A + \rho_B}{2}$.

Two sets of hall coefficient can be calculated by the following:

$$R_{HC} = \frac{t}{B}\frac{V^{+}_{31,42}(+B) - V^{-}_{31,42}(+B) + V^{-}_{31,42}(-B) - V^{+}_{31,42}(-B)}{I^{+}_{31}(+B) - I^{-}_{31}(+B) + I^{-}_{31}(-B) - I^{+}_{31}(-B)}$$

$$R_{HD} = \frac{t}{B}\frac{V^{+}_{42,13}(+B) - V^{-}_{42,13}(+B) + V^{-}_{42,13}(-B) - V^{+}_{42,13}(-B)}{I^{+}_{42}(+B) - I^{-}_{42}(+B) + I^{-}_{42}(-B) - I^{+}_{42}(-B)}.$$

Again these two should agree to within +10%, if they do not, a new sample is needed to make a second measurement. If they do agree, then the average hall coefficient can be calculated and hall mobility is given by $\mu_H = \frac{R_{HC} + R_{HD}}{2\rho}$.

In Hall measurement 7604 system, all above calculations are automatically done by the company software. However, the sample itself needs to meet certain requirement, such as uniformity of the sample thickness and symmetry of the sample. A subtle polishing system is utilized to maintain the uniformity of the sample thickness, the details of this system will be discussed in the next chapter. Also during our sample preparation, a commercial graphite die is used, so a perfect circular sample is obtained for each hot press.

## 2.4 Seebeck Measurement

Unlike the electrical measurements, Seebeck coefficient measurement is independent of geometric parameters. The Seebeck coefficient is defined as the ratio of the electrical potential difference V to the temperature difference T. Although Seebeck coefficient measurement is not sensitive to heat loss, unsteady heat loss is not desirable for

accurate results. In order to minimize conductive heat loss though the thermocouple wire, thermocouples with a diameter of 0.003 inches are utilized.

In order to minimize the temperature fluctuation by convection, measurement is usually done in partial vacuum under 100 torr since a small amount of inert gas is needed to transport heat and provide the temperature gradient across the sample. An electrical heater is utilized to produce the temperature gradient. Several data points are collected and used to make the plot between temperature and voltage. The Seebeck coefficient is acquired from the slope of the plot by compensating for the Seebeck coefficient from thermocouple wires.

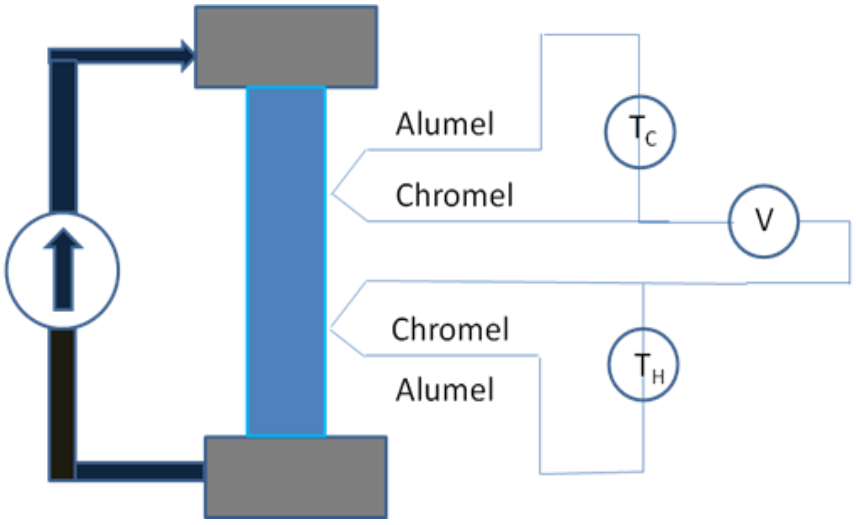


**Fig. 2.4.1.** Schematic of Seebeck measurement for ZEM-3 unit.


**Fig. 2.4.2.** A picture of ZEM-3 unit.

In the ZEM-3 system, during the Seebeck measurement, no current passes through the samples. The only source of EMF is from the Seebeck effect in the sample and probe leads. The Seebeck voltage is detected from two voltage probe leads. Together with the temperature signal from the same two thermal couples, Seebeck coefficient is determined. Fig.2.4.1 shows a detailed schematic of the Seebeck measurement configuration. The actual equipment for the Seebeck measurement is shown in Fig. 2.4.2. Moreover, since Si or Ge easily reacts with most metals especially at high temperatures, a buffer layer between the SiGe sample and thermocouple is needed in order to prevent this reaction. After examining the phase diagram between SiGe and typical metals, Nb foil and graphite sheet were the only choices we can use as buffer layer. However, there was too much heat loss through Nb foil during measurement, while the graphite sheet provided a relative small heat leakage. The measurement results of standard samples with or without graphite agreed within 5 percent. Thus, for SiGe sample measurements, a graphite sheet with the thickness of 75 microns was

always inserted between the sample and the thermocouple.

The Seebeck coefficient of the sample is determined from the measured temperature and voltage differentials. The following equation is used to calculate the Seebeck coefficient, $S = -\frac{\Delta V}{\Delta T} + S_{tc}$, where $S_{tc}$ is the correction due to thermocouple Seebeck coefficient. In order to remove the systematic error, a linear regression method is always applied. From the slope of V-T plot, the Seebeck coefficient is obtained after compensating for the thermocouple Seeback coefficient, which is incorporated in the ZEM-3 software. A typical Seebeck computation plot is shown in Fig. 2.4.3. The measured Seebeck value at room temperature for constantan agrees well with well established data within 5%. This demonstrates the reliability of the measurement.

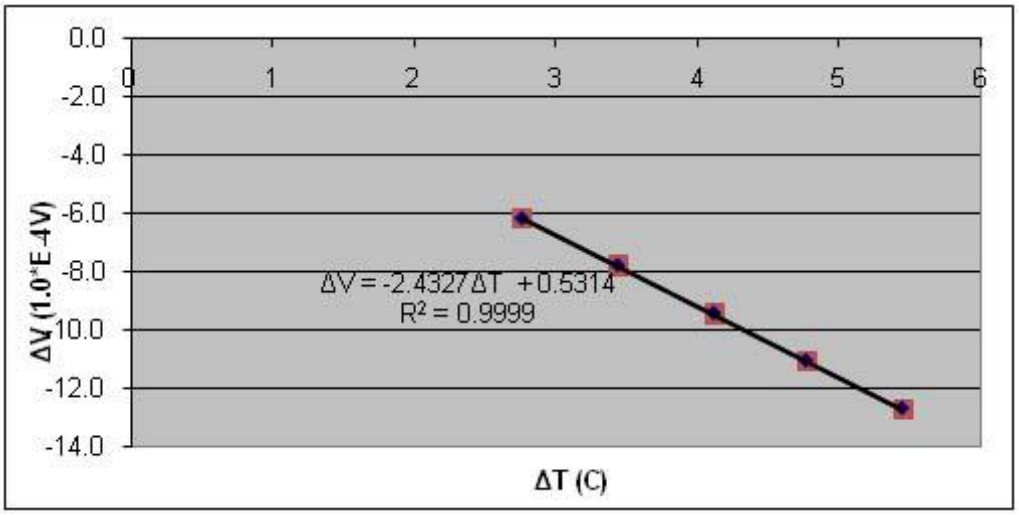


**Fig. 2.4.3.** A typical Seebeck computation plot.

In principle, the V-T plot should have a zero intercept. However in practice, this is not always the case. There are unknown sources of EMF, which cause a non-zero intercept,

or dark EMF. In ZEM-3 unit, a dark EMF is calculated at each temperature point, one should note that the measurement result is reliable only if the dark EMF doesn't exceed 10% of the Seebeck voltage signal. ZEM-3 uses a temperature stability parameter to decide when the system is in thermal equilibrium state, however, if the temperature stability is very small, a much longer measurement time is required.

## 2.5. Thermal Conductivity Measurement

The thermal conductivity k is defined as the ratio of heat flux q to the temperature gradient T caused by the heat flux k=q/T, the same schematic we used for the Seebeck coefficient measurement can be applied to the thermal conductivity. Due to radioactive or convective heat loss or the loss from unstable thermal contact between the sample and the heater, minimizing unwanted heat flow is the critical factor for the thermal conductivity measurement. The laser flash method has been developed to correctly determine thermal conductivity of varieties of bulk materials with the formulation first deduced by Parker in 1961 [14] and reviewed by many researchers [15-17]. In this method, no thermal contact is needed since a laser flash serves as the heat source. In addition, the heat loss through sample boundaries and radiation is minimized by sufficient measurement time. Fig. 2.5.1 shows the sketch of laser flash method. An IR detector monitors the temperature rise versus time profile of the rear surface of the sample and the thermal diffusivity is calculated from this temperature profile. The picture of an actual measurement system is shown in Fig. 2.5.2.

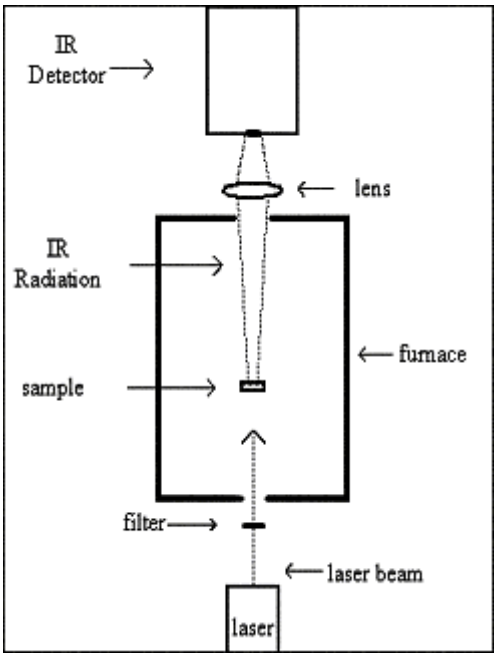


**Fig. 2.5.1.** The schematic of laser flash method.

**Fig. 2.5.2.** A picture of laser flash apparatus LFA 457.

The thermal conductivity is related to the thermal diffusivity by the following formula: $k = C \cdot d \cdot \rho$, where $d$ is the thermal diffusivity, $C$ is the heat capacity, and $\rho$ is the sample density. Thermal diffusivity represents how fast a body can dissipate thermal energy. or in other words, how fast a body can change its temperature when there is a heat flow through it. Specific heat capacity is the measure of the heat energy required to increase the temperature of a unit quantity of a substance by a certain temperature interval. Sample density can be measured from standard Archimedes' method [18].

By solving the one dimensional thermal diffusion transport equation with an initial temperature distribution of T(x,0) as follows,

$$T(x,0) = \frac{Q}{\rho C_P g}, \quad \text{for } 0<x<g$$

$$\text{and} \quad T(x,0) = 0, \text{ for } g<x<L$$

where Q is the laser pulse of energy, and g is the deepest length laser energy can be absorbed [19]. Temperature distribution at any time is given by the following equation,

$$T(x,t) = \frac{1}{L}\int_0^L T(X,0)dx + \frac{2}{L}\sum_{n=o}^{\infty} \exp\left(\frac{-n^2\pi^2\alpha t}{L^2}\right) \times \cos\frac{n\pi x}{L}\int_0^L T(x,0)\cos\frac{n\pi x}{L}dx.$$

Because g is always small (since the duration time for laser pulse is less than 1 msec), this equation can be simplified to:

$$V = 1 + 2\sum_{n=0}^{\infty}(-1)^n \exp(-n^2 w),$$

where $V = T(L,t)/T_M$, $w = \pi^2\alpha t / L^2$ and $T_M$ is the maximum temperature at the rear surface.

Further analysis shows these two parameters are correlated. In particular, when V equals 0.5 ($t=t_{1/2}$), w is equal to 1.38, as shown in Fig. 2.5.3. With these values, thermal diffusivity can be rewritten as $\alpha = 0.138L^2 / \pi^2 t_{1/2}$.

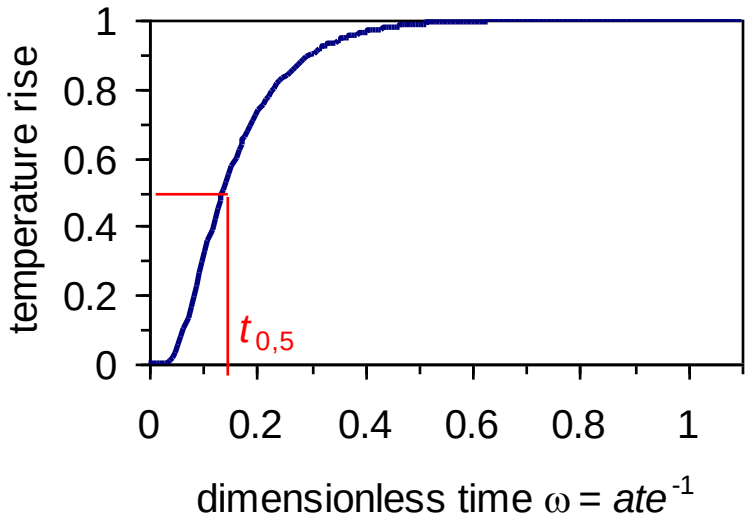


**Fig. 2.5.3.** Temperature rise curve plotted again dimensionless time ω.

By theoretical calculation, the specific heat can be obtained for any element materials and its alloys, but the laser flash system has the power to measure the specific heat directly. The amount of energy of heat flow needs to be considered to calculate heat capacity as shown in the following formula:

$$C_p = Q / \rho L T_M .$$

this exact energy amount is hard to determine due to energy loss. An alternative method is to compare the temperature rise with a standard sample. Assuming that laser pulse energy and its coupling with the sample remain unchanged, the specific heat of the sample can be

calculated by the following formula:

$$C_{P(sample)} = (mC_p\Delta T)_{ref} / (mC_P\Delta T)_{sample}.$$

$C_P$ measurement data from laser flash system always contains large errors, in some cases, 5-10% deviation is observed. As a result, specified equipment (DSC 200 F3) from Nestch is used to determine the actual specific heat for each type of nanostructured sample.

In an actual measurement, a disc sample of ~12.7 mm diameter with the thickness of 1 or 2 mm is put into an argon environment furnace, and aligned between the laser beam and an indium Antimonide (InSb) IR detector. A thermocouple in contact with the sample is used to control the temperature of the sample. In order to minimize errors, three sets of data are collected on each temperature point. In addition, a graphite coating provides relatively uniform absorption of laser energy and emission of thermal energy, which is very important in specific heat measurements.

Fig. 2.5.4 is a typical experimental curve of IR signal vs. time. It is not as smooth as the theoretical curve, mainly due to the following issues. The first is that the heating of the front surface can't be considered instantaneous relative to the time it takes to diffuse through the sample. Other issues are related to heat loss and non-uniform heating. In the laser flash system, there are many built in models which take these issues into account, and we can choose the one which best fits our experimental conditions and sample properties. After correction, the thermal diffusivity measurement data has the accuracy of about 2%, coming primarily from thickness measurement uncertainty.

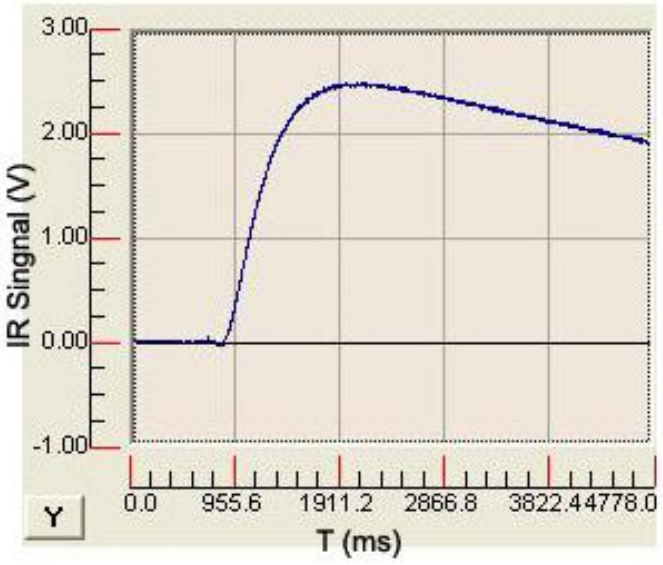


**Fig. 2.5.4.** Typical Experimental curve of IR signal vs. Time for each laser shot.

## 2.6. Special Heat Measurement

As we explained in the previous section, the $C_p$ results from the laser flash system generally have a large deviation of about 5-10% percent even for samples with same SiGe composition. In order to measure the exact $C_p$ value of our nano SiGe samples, a specified DSC 200 F3 equipment from Nestch is utilized to measure specific heat.

The principle behind the measurement is differential scanning calorimetry [20], which is a thermoanalytical technique in which the difference in the amount of heat required to increase the temperature of a sample and a reference are measured as a function of temperature. Both the sample and the reference are maintained at nearly the same temperature throughout the experiment. Generally, the temperature program for a DSC

analysis is designed so that the sample holder temperature increases linearly as a function of time. The reference sample should have a well-defined heat capacity over the range of temperatures to be scanned. In our system, the maximum temperature is 600 degree C, and the standard sample is a sapphire disc.

For practical experiments, a sample with a diameter of about 5.5 mm and a thickness of 0.5-1.0 mm is utilized. Optimum sample thickness is dependent on the thickness of the standard sapphire disc [21]. Generally, three measurements need to be done before calculating specific heat of a sample. Those three measurements are for the baseline, the sapphire disc and the sample. The specific heat of a material can be calculated from three measurements, as shown in the following formula:

$$C_P = \frac{signal \quad difference \quad (sample - baseline)}{sample \quad mass \bullet heating \quad rate \bullet sensitivity},$$

where the sensitivity is obtained from the sapphire measurement, as shown in the following,

$$sensitivity = \frac{signal \quad difference \quad (sapphire - baseline)}{mass(sapphire) \bullet heating \quad rate \bullet theoret. \quad C_P(sapphire)}$$

Actual measured DSC data for typical SiGe sample is shown in Fig. 2.6.1. From those DSC data, by applying ratio method, the $C_p$ value of the sample is calculated, as shown in Fig. 2.6.2.

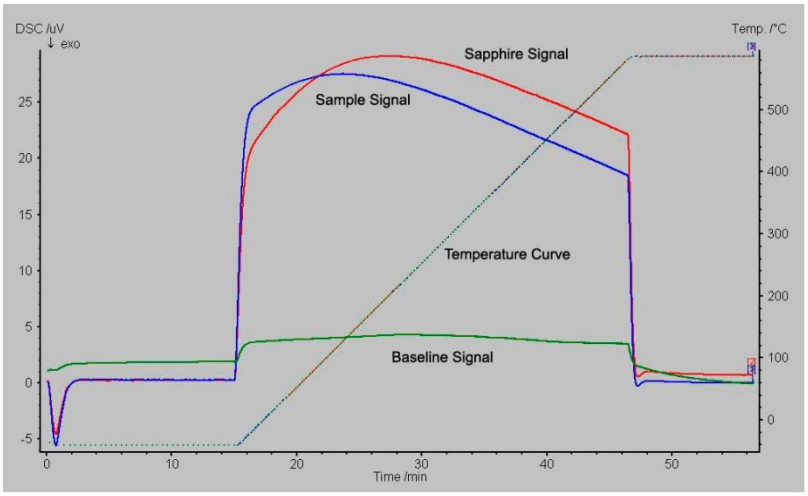


**Fig. 2.6.1.** DSC data from an actual measurement.

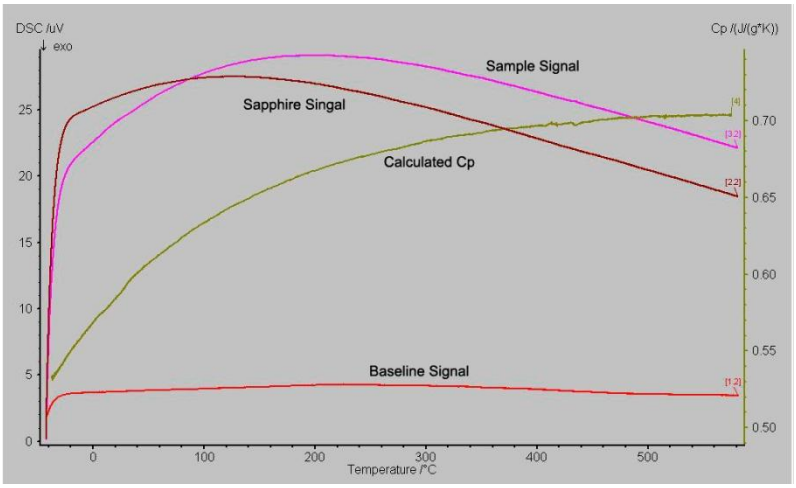


**Fig. 2.6.2.** Cp calculation of typical SiGe sample.

In traditional SiGe alloys, since only around 0.5% percent P is added, there is no deviation of the $C_p$ value with or without P doping. However, for our nano approach, more than 2 percent P is added. Thus it is necessary to examine whether there is a deviation of $C_p$ value with or without such large amount P doping. Fig. 2.6.3 shows the $C_P$ measurement results of nano samples with three different SiGe compositions. For comparison, the calculated $C_p$ values of these three compositions are included [22]. Clearly, experimental data

are within 2% percent deviation of the theoretical calculations, which confirm that P doping doesn't have any large effect on the $C_p$ value of nano SiGe sample. This, along with the fact that $C_p$ results from laser flash system shows a large deviation even on the samples with a similar composition. Therefore, theoretical $C_p$ data is utilized for all SiGe nano samples, especially P-doped samples.

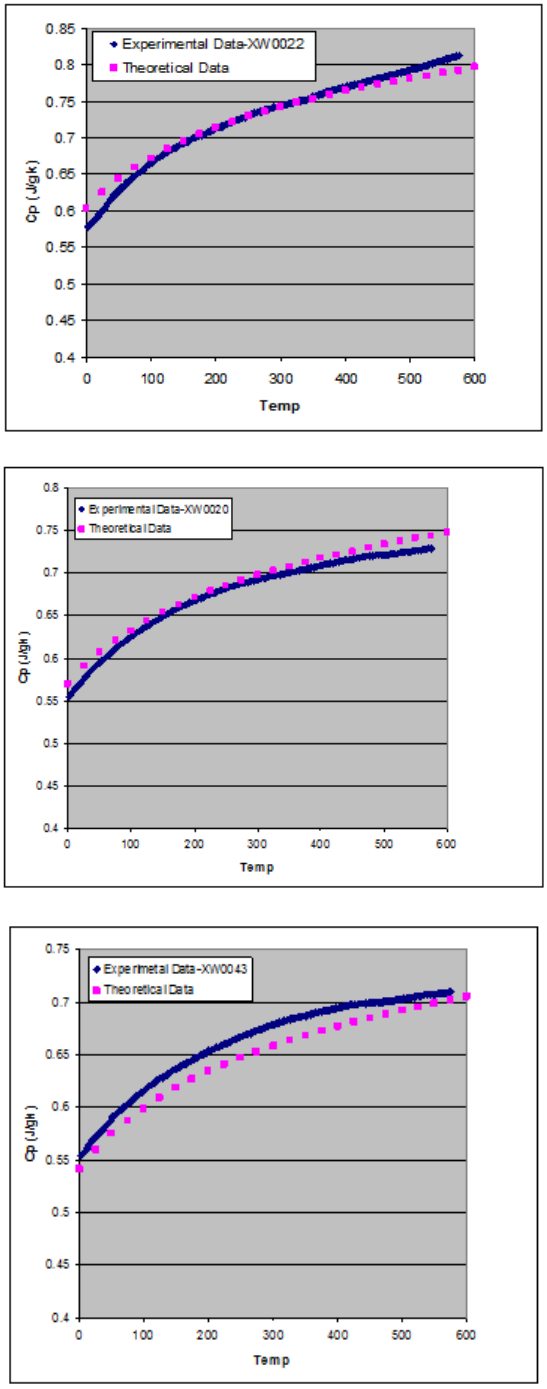


**Fig. 2.6.3.** Comparison between experimental $C_p$ data and theoretical $C_P$ data for three SiGe nano samples of $Si_{90}Ge_{10}P_{2.5}$ (Top one), $Si_{85}Ge_{15}P_3$ (middle one), and $Si_{80}Ge_{20}P_2$ (Bottom one).

## 2.7. References


1. T. C. Harman, *J. Appl. Phys.* **29**, 1373 (1958).
2. N. Z. Lupu, N. M. Tallan, D. S. Tannhauser, *Rev. Sci. Instrum,* **38**, 1658 (1967).
3. T. M. Tritt and V. M. Bowning, *Semiconductors and Semimetals* Academic Press, San Diego, CA, **69**, 25, (2001).
4. S. M. Sze, *Physics of Semiconductor Devices,* Wiley Inter-Science, 1981.
5. *CRC Handbook of Thermoelectrics,* edited by D. M. Rowe, CRC Press, Boca Raton, FL, 1995, 157.
6. R. Sundaresan and F. H. Forces, *J. Metals,* **39**, 22, (1987).
7. G. K. Williamson, W. H. Hall, *Acta Metal.* **1**, 23 (1953).
8. D. M. Rowe and R. W. Bunce, *J. Phys. E.* **4**, 902 (1971).
9. V. V. Batavin, V. S. Pantuev and V. I. Prilipko, *Measurement Techniques*, **17**, 1753 (1974).
10. T. Harman, M.P. Walsh, B.E. LaForge, and G.W. Turner, "*Nanostructured Thermoelectrics Materials*," Journal of Electronic Materials, 34, L19 (2005).
11. C. A. Kukkonen, P. F. Maldague, *Phys. Rev. B*, **19**, 2394 (1979).
12. T. Krylova, V. Mochan, *J. Tech. Phys.*, **25**, 2119(1955).
13. L. J. Van der Pauw, *Philips Technical Review*, **20**, 220 (1958).
14. W. J. Parker, R. J. Jenkin, C. P. Butler, and G. L. Abbott, *J. Appl. Phys.*, **32**, 167 (1967).

15. F. Righini and A. Cezarliyan, *High Temp-High Press.*, **5**, 481 (1973).

16. R. E. Taylor, and K. D. Maglic, in Compendium of Thermophysical Property Measurement Method, Vol. 1, Plenium Press, NY, 305 (1984).

17. R. Taylor, in First European Conference on Thermpelectrics, Peter Peregrenius, London, 107 (1897).

18. K. C. Chou, J. H. Hu, *J. of. Metallurgical and Materials Transactions B*, **22**, 1073 (1991).

19. L. Kehoe, P. V. Kelly, G. M. Oconnor, M. Oreilly, G. M. Crean, *IEEE Transactions on Components, Packaging, and Manufacturing Technology*, **18**, 773 (1995).

20. M. J. O'Neill, *Anal. Chem.*, **36**, 1238 (1964).

21. DSC 200 F3 manual from Nestch inc. (2006).

22. L. P. Filippov, *J. of. Engineering Physics and Thermophysics*, **32**, 378, (1977).

# Chapter 3

# Preparation and Thermoelectric Properties of nanostructured n-SiGe Materials

This chapter discusses the experimental procedure and characterization of as-made SiGe alloys. Our sample preparation technique includes high energy ball milling and a hot press of the resulting powder into a solid sample. Measurement results of nanostructure bulk SiGe alloy will also be presented in detail. In addition, a brief introduction of SiGe materials will be provided and its properties will be included. Precipitation of phosphorus in SiGe and isotropic thermoelectric properties are discussed in this chapter as well.

## 3.1. Introduction

Silicon and Germanium are the most common semiconductor materials used in industry. Both elements are in the same carbon group. Although they are less active than carbon, they very rarely occur as pure free elements in nature. Silicon is more widely distributed in dusts as various forms of silicon dioxide or silicates. Germanium is contained in a few minerals, such as germanite, briartite, and renierite [1].

Silicon has many industrial uses. Elemental silicon is the principal component of most semiconductor devices, such as integrated circuits of memory chips. Silicon has a larger band gap, possesses a higher working temperature and is less costly than Germanium. Therefore Silicon instead of Germanium is more widely used in semiconductors. Moreover, its native oxide is easily grown on a surface and forms a better insulator layer than other

materials. Amorphous silicon is used in production of low-cost, large-area electronics in applications such as LCDs, and large-area, low-cost thin-film solar cells [2]. Germanium's major end applications are in fiber-optics systems and infrared optics [3]. In addition, Germanium substrates can be used to grow gallium arsenide solar cells since the two have very similar lattice constants [4].

It is well known that the transistor density of integrated circuits doubles every 24 months, as predicted by Moore's law [5]. By 2050, the size of the transistor, which is the building block for circuit devices, will shrink into the nanometer range. Thus, various nanostructures of silicon or germanium are fabricated and their properties are investigated for understanding fundamental concepts about the role of dimensionality and size and potential applications in electronic or optic fields [6]. Nanostructured materials have lots of special characteristics, which do not exist in bulk counterparts. For example, silicon nanoparticles can emit visible light with different wavelengths according to the diameter of the particles. Conversely, bulk silicon has no photo spectrum in the visible range because of its large band gap [7]. Moreover, ballistic electrical transport can be realized when the size of nanowires is less than the critical value, i.e. mean free path of electrons or holes. When this occurs, there is almost no joule heating generated when current passes by. The prototype for transistors based on silicon nanowires can be found in literature [8].

In the thermoelectric, elemental silicon and germanium are not good candidates because of their high thermal conductivity. However, in 1962, the discovery that thermal

conductivity of silicon-germanium alloys was much lower than predicted by linear interpolation spurred interest in thermoelectric applications [9]. The lattice thermal conductivity of silicon and germanium at 300K is 113 and 63 W/m*K, respectively, while $Si_{70}Ge_{30}$ has a value of only about 10 W/m*K. Therefore, in the 1960s, the thermoelectric properties of SiGe alloys were studied as a function of composition, carrier concentration, and temperature using heavily-doped zone-leveled materials [10]. Later on, those alloys were prepared by using more economically efficient powder metallurgical techniques for commercial applications. Since 1976, those alloys were first used in space in the SNAP-10A nuclear reactor and have been the exclusive choice for radioisotope thermoelectric generators (RTGs) launched by the U.S.A to provide reliable electrical power. Primary considerations for space power applications are reliability and high operating temperature, taking advantage of the temperature dependence of radiator heat rejection rates, or high carrot efficiency. In addition to their attractive thermoelectric and physical properties, SiGe devices can operate at temperatures up to about 1300 K without significant degradation [11].

The main advantage of SiGe alloys as thermoelectric materials is their lower thermal conductivity. Consequently, various efforts to improve their thermoelectric performance, especially thermal conductivity of SiGe alloys have been made. For example, many new forms of SiGe materials have been produced, such as amorphous SiGe, and SiGe superlattices, etc [12-13]. In 1993, Hicks and Dresselhaus proposed a possible enhancement in ZT through the use of quantum well supperlattices and quantum wires. Reduced

dimensionality enhances the density of states by quantum confinement, leading to a higher Seebeck coefficient without a decrease in electrical conductivity [14]. In addition, nano grain boundaries scatter more phonons and obtain lower thermal conductivity. Since then, various nanostructured SiGe materials have been produced and studied extensively, particularly on SiGe/Si supperlattice forms and more recently on Si nanowires [15-17]. Although nano SiGe materials can enhance thermoelectric performance, significant challenges exist in fabricating those structures at low cost. The anisotropic nature of most nano materials, especially in supperlattice form, makes their thermal conductivity performance unpredictable. However, experimental and theoretical studies show that periodic structures are not needed for lower thermal conductivity. The increased number of boundaries is the critical factor for thermal conductivity reduction [18]. In our lab, we use a very simple and cost-effective method to produce bulk alloys with various random nano grains. This creates numerous scattering centers, leading to better thermoelectric performance. This technique had already been experimentally proven with BiTe/BiSe systems [19]. In this chapter, the technique which is used to produce the nano SiGe alloy samples is explained in details. The thermoelectric properties of these nano samples in comparison with current RTG reference samples are discussed as well.

## 3.2. Preparation Method of SiGe Alloys

The vast majority of modern thermoelectric semiconductors are solid solution or chemical compounds. In order to understand the process of preparing these materials, a good knowledge of solid-liquid equilibrium phase diagrams is required. Fig. 3.2.1 shows the phase diagram of a silicon germanium alloy. As we can see, although silicon and germanium are completely miscible in both liquid and solid states, a large separation exists between the liquidus and the solidus. A gap of more than 50 degree C exists between the liquidus and the solidus for $Si_{80}Ge_{20}$, which complicates the preparation of homogeneous solids because of alloy segregation. Usually there are three methods to produce SiGe bulk alloy as discussed in the following sections. The technical processes for producing SiGe thin films or super lattices can be found in the review paper [20].

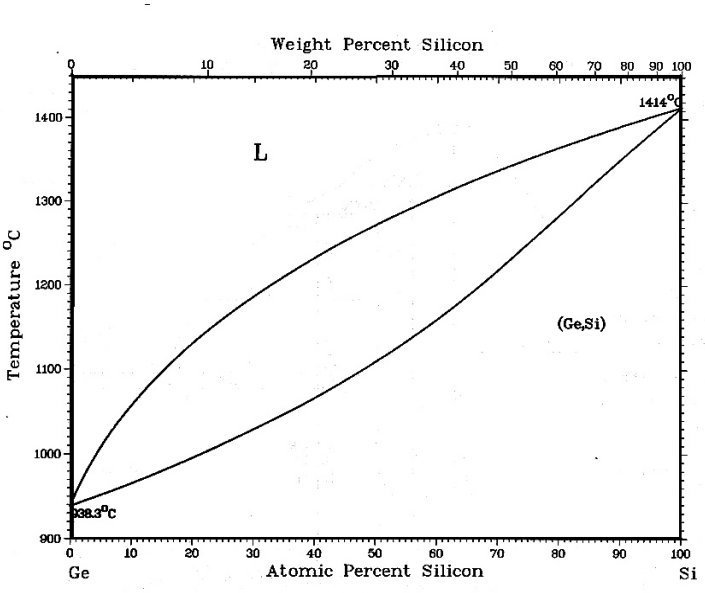


**Fig. 3.2.1.** Phase diagram of SiGe alloy.

### 3.2.1. Melting method

The preparation of chemical compounds or solid solutions from a melt begins with melting the elemental constituents together, a process referred to as synthesis or alloying [21]. It is essential to use high-grade elements of high purity in order to prevent contamination. A radio frequency furnace needs to be cleaned by standard semiconductor cleaning procedure. In addition, SiGe tends to form oxides on its surface, so the whole process has to be operated in argon-protected environment, and all oxides are required to be etched away before putting it into the furnace. Also large pieces are used in order to minimize the surface area of SiGe.

After cleaning, the large pieces (10 to 20 mm) of silicon and germanium (mass ratio of Si to Ge depends on the composition of SiGe), together with the dopant, boron for p-type and phosphorus for n-type materials, are placed into an open quartz crucible. The crucible is inserted into a graphite susceptor in the furnace chamber, and the chamber is vacuum pumped to remove resident oxygen. After purging of the chamber by argon, a slight overpressure of argon is established (1.1 atm), the temperature is raised to around 1300 degree C within 2 or 3 hours (exact operational temperature value depends on the composition of the alloy). Eddy currents develop an intensive stirring motion to help the homogenization of the melt. After this, the melt is cast inside the chamber into the water-cooled copper mold, resulting in high fine-grained ingots. Although the bulk atomic ratio of Si to Ge shows reasonable agreement with nominal composition; these materials need to be further processed for the homogeneous ingot preparation because of alloy segregation.

There are many processes which can be used to obtain homogeneous alloys, such as, bridge method, gradient freeze, Czochralski method, and zone melting [22]. The most common way is zone leveling, which was used for the first space application of SiGe thermo-elements in the SNAP-10A nuclear reactor. The procedure is described as following. A charge bar is prepared from any convenient method (e.g., melting, powder metallurgy) with the desired final composition. A zone bar is similarly prepared with a composition to have a freezing point at the same temperature as the melting point of the charge bar, and the resulting liquid zone caused to transfer the length of the charge bar. As the liquid zone moves to the right, the charge bar is consumed at the leading edge of the liquid zone and a homogeneous ingot of SiGe freezes out of the trailing edge. To prevent supercooling, a low growth rate is preferred, typically 0.5 mm/h.

### 3.2.2. Powder Metallurgy Technique

Powder metallurgy is broadly defined as the process whereby powders are compacted at any desired temperature and then sintered at elevated temperatures to form a dense body with a well-defined, coherent grain structure. If the compaction occurs at elevated temperature, it is commonly known as hot-pressing. Today, powder metallurgical methods are generally preferred for production of significant quantities of SiGe, primarily because large, good-quality samples can be prepared from powders in a single day. Also, relatively large variations of preparation conditions can be tolerated while still producing satisfactory

thermoelectric properties. Hot-pressed SiGe has been used in RTGs for many years. The preparation procedure is shown in the following paragraphs.

Typically, a 4 to 1 atomic ratio of Si and Ge is melted in fused silica crucibles under vacuum together with a desired doping agent (P for n-type and B for p-type). The melt is cast into a water-cooled copper mold and mechanically pulverized to -80 mesh powder. Occasionally, ball milling is used to further reduce the size of the grains to improve the strength and homogeneity of the final compact. After that, the powders are placed in dies and molds are made from an alloy of titanum, zirconium, and molybdebum, lightly coated with graphite to reduce friction during ejection. Pressure-sintering is performed under 180 Mpa of pressure, applied after reaching 1513 K. Pressure released after 30 min when the compact is ejected from the die and allowed to cool in air.

### 3.2.3 Mechanical Alloying

Mechanical alloying (MA) was first developed to produce oxide dispersion-strengthened alloys. Mechanical alloying is a high-energy ball mill technique used to produce alloyed powder through solid-state reactions. MA occurs basically through a repeated process of fracture and cold welding of powder particles trapped between grinding balls, elemental powders are alloyed through a sequence of collision events inside a high energy ball mill. Although the average temperature inside ball milling jar is normally below 100 degree C, the localized heat generated by collisions of the balls with the materials can

raise the temperature of the alloy, which provide a driving force for inter-diffusion of the components along atomically clean fracture surfaces. Davis and Koch first demonstrated the application of MA to the brittle system of SiGe [23]. Later, actual preparation of n-type or p-type SiGe was accomplished by Cook [24].

In practice, for both n-type and p-type alloys, weighed portions of the constituents in the form of +20 mesh chunks were sealed in a steel vial with steel balls. After the mixture was milled continuously for some time (exact required time is determined by the rotation speed of the ball mill machine), X-ray diffraction patterns showed a heavily cold-worked, single-phase alloyed powder with a diamond cubic structure. After a vacuum hot pressing, a dense disc compact sample was obtained. The density of the hot-pressed SiGe alloys was greater than 99% of theoretical density. X-ray diffraction analysis indicated the formation of a homogeneous crystalline, single-phase alloy.

Mechanical alloying is a common method used in the preparation of SiGe thermoelectric materials. Compared to other methods, mechanical alloying removes the problem of volatilization of dopants such as phosphorus. Also the process reduces the problem of inhomogeneous SiGe alloys that arises from dendrite segregation caused by the wide separation of the solidus and liquidus in the SiGe phase diagram. In addition, it is much easier to add nanometer-sized inclusions to act as phonon scattering points during mechanical alloying process compared to other processes, like zone leveling.

## 3.3 Our Experimental Approach

As we presented in the first chapter, our group has developed an approach based on random nanostructures, which can provide numerous amount of grain boundaries similar to those of supperlattices to significantly reduce thermal conductivity, leading to a high ZT. Fig. 3.3.1 and Fig. 3.3.2 show the schematic of our experimental approach for the SiGe system.

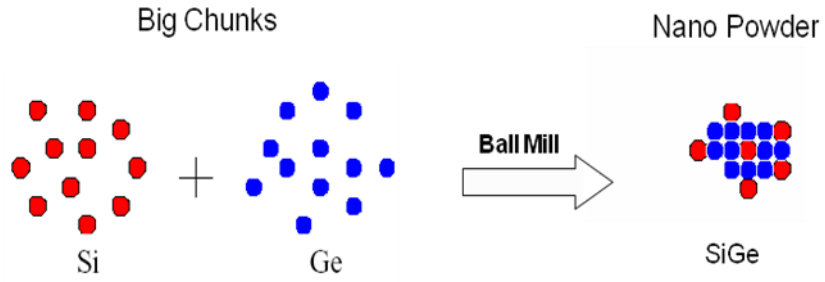


**Fig. 3.3.1.** A schematic of ball mill process.

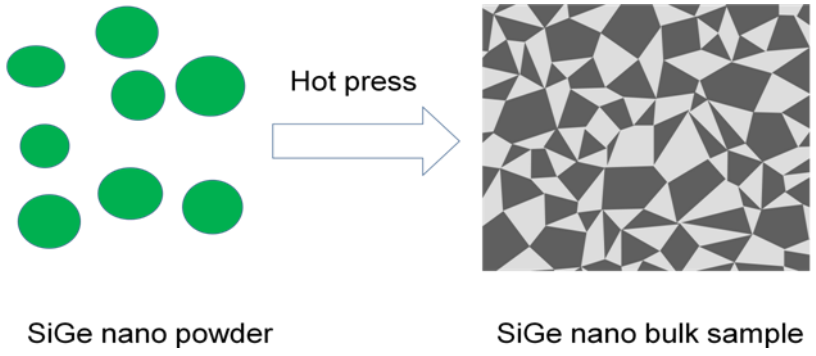


**Fig. 3.3.2.** A schematic of hot process.

### 3.3.1. Preparation of Alloyed SiGe Nanopowders

As shown in Fig.3.3.1, the first step is to produce SiGe alloy powders with nano size grain, which can be achieved by the mechanical alloying method. Compared to other alloying methods, mechanical alloying minimizes volatilization of the dopants, specifically, phosphorous because of its low melting temperature. In addition, this method provides an impurity and oxygen free environment since the loading process is operated inside a glove box and then mechanically sealed very well in the ball mill jar. Both Si and Ge are sensitive to oxygen and previous results have already shown that low oxygen alloys consistently had higher figure of merit [25]. Thus, commercial chunks of Si or Ge are used instead of Si or Ge micro-powder because of their small surface area.

In practice, about 6 grams each of Si and Ge chunks together with phosphorous powder were loaded into a stainless steel jar inside the glove box, the mass ratio of Si ,Ge and P are determined by the composition of the alloy we want to make. After loading, the jar was put into the ball milling machine and run for some time, usually from 20 to 100 hours. The exact amount of time was determined by the speed of the machine. In order to prevent the nanopowder from sticking to the wall of the jar, the compressed powder is loosen inside the glove box after each ball milling run. For the Glen planetary machine (600 rpm), typically the total ball mill time is 110 hours, while for the Spex 8000 machine (1080 rpm), 25 hours was enough to obtain alloyed powder. The actual equipments used for ball milling are shown in Fig. 3.3.3.


**Fig. 3.3.3.** Pictures of ball mill machines with low (left one) and high (right one) speed.

The purpose of ball milling is to obtain nano SiGe alloy powder, thus XRD is used to check the degree of alloying and the sizes of grains. Fig. 3.3.4 shows XRD spectrums of the nanopowders with 80:20 composition made from Glen mill or Spex machine. It is clear that two separated peaks appear in each corresponding (111), (110), (221) positions of single crystal Si or Ge when ball mill time is not long enough. For the Glen mill system, after 120 hrs, the two separate peaks merge into one peak, indicating that alloy formation. However, for the Spex machine, only 15 hrs are required to obtain a nearly alloyed powder. In addition, all the peaks are very broad, indicating the particles are small. By using the Williamson-Hall method [26], an average grain size of about 15nm is calculated, which is confirmed by TEM images, as shown in Fig. 3.3.5. From Fig.3.3.5a, we can see that the average particle size of the nanopowder is in the range of 30-200 nm. However, those particles are actually agglomerates of much smaller crystallites. Fig.3.3.5b shows the TEM image and selected area electron diffraction pattern (SAED) of one of those typical particles, which indicates that

the particles are actually composed of many small crystallites. It is also confirmed by HRTEM that the sizes of the small crystallites are in the range of 5-15 nm (Fig.3.3.5c), which is consistent with the results from XRD spectra. Moreover, EDS is applied to check the uniformity of the as-prepared SiGe powder in the micro- or nano- meter range, the result shows that the powder has a very uniform distribution of Si/Ge ratio, which is further confirmed by lattice parameters from XRD spectra calculation. A single value of 0.546 nm is obtained with the help of a Nelson-Riley extrapolation routine [27]. This differs from an ideal 80:20 SiGe alloy by 0.03%.

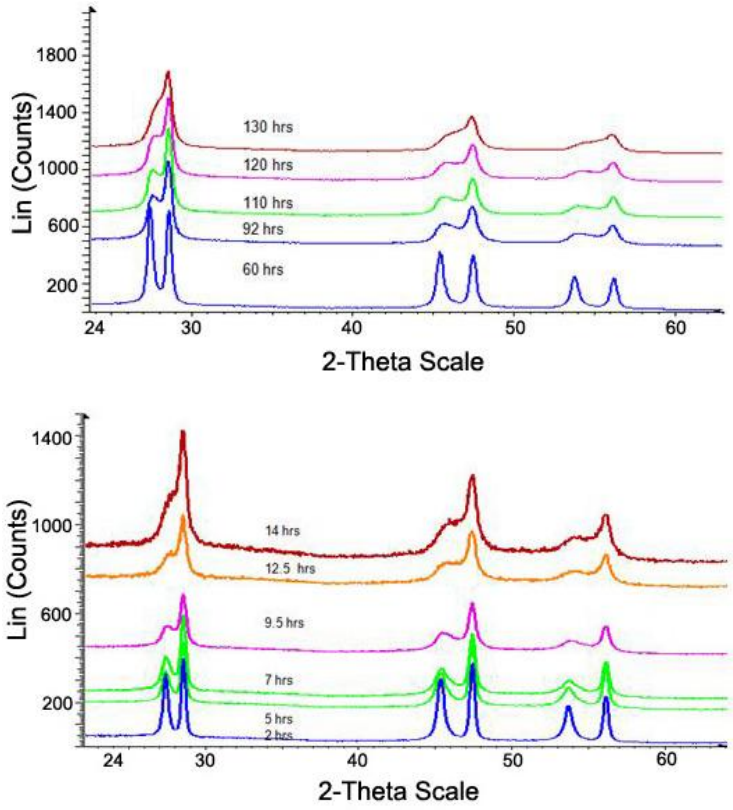


**Fig. 3.3.4.** Alloy process of $Si_{80}Ge_{20}P_2$ nano powder from Glen mill (up) and Spex (low).

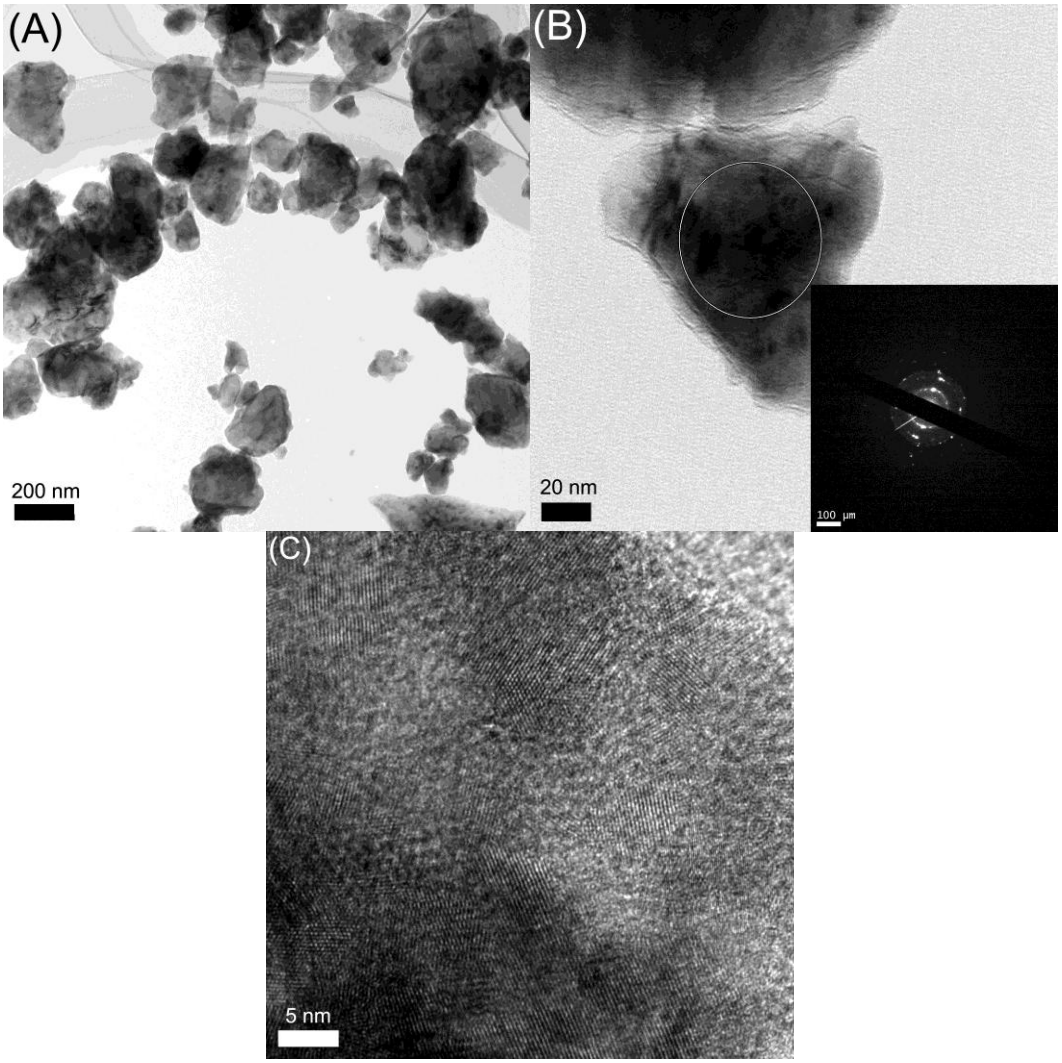


**Fig. 3.3.5.** TEM images with low- (A), medium- (B), and high- (C) magnifications of typical ball milled nanopowders.

### 3.3.2. Consolidation of SiGe Alloy Powders

After obtaining alloyed nano SiGe powder, the next step is to consolidate the as-prepared nanopowder into a bulk solid sample with a density close to 100% of the theoretical value, as shown in Fig. 3.3.6. The main challenge here is to maintain the nano

grains during the consolidation process, or at least minimize grain growth during densification. Here we chose a direct current hot press technique to compact the powders. There are two advantages to this consolidation process. First, the heating rate can be as high as 200-300 degree C per minute, which helps to prevent grain growth during the hot press. Second, since the whole compaction process only lasts less than 10 minutes, no vacuum or Argon environment is needed. This is a time saving process, each sample can be densified in a few minutes, which is very important for industrial application.

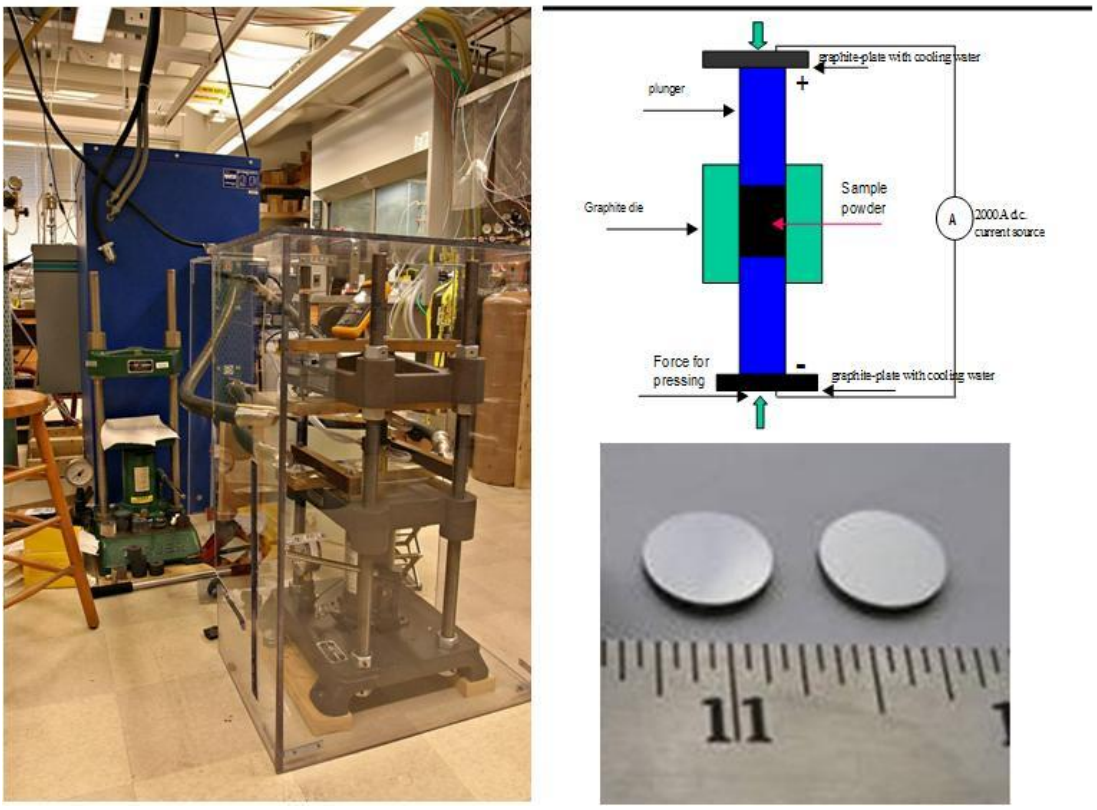


**Fig. 3.3.6.** A picture of our hot press equipment (left), a schematic of our hot press system (top right) and a picture of samples after hot press (bottom right).

Instead of buying expensive DC hot press equipment, we used a simple lab-made instrument, as shown in Fig.3.3.6. A commercial power supply is used to provide large DC current up to 2000 amps. That current then passes through the sample powder which is loaded into a graphite die and pressed by two graphite plungers. The joule heating and the plasma inside the powder help to quickly heat the sample powder to any desired temperature, namely, the solidus temperature of the material. Meanwhile, pressure is applied to help to obtain a high density sample. Also cooling water is installed to cool the two electrodes. In a typical experiment, about 1.6 grams of SiGe nanopowder was loaded into the graphite die. Then, starting at 200 A, high current was introduced with a rate of increase of 200 A per half minute until our desired temperature was reached. The powder was then held for 2 minutes to obtain a completely alloyed disc sample. During the process, by using a Carver Press, the pressure was kept at 100 Mpa at the beginning, followed by 150 Mpa when the temperature reached 750 degree C. After the hot press, the sample was extracted when the temperature dropped below 600 degree C in order to prevent dopant precipitation. Fast heating and cooling were used to maintain the nano future of the as-made powder. Pressure was applied to obtain high density. While loading powder in the Ar environment is utilized to prevent oxidation, which is essential for SiGe system since both elements are very sensitive to oxygen, when there is too much oxygen inside the powder, the electrical properties will be severely affected.

Although the solidus temperature for SiGe alloys is very high, for example, $Si_{80}Ge_{20}$

has the melting temperature of about 1350 degree C. the actual densification temperature is typically from 950 to 1100 degree C for $Si_{80}Ge_{20}$ composition, which is considerably lower than temperatures used during the hot pressing of conventional cast and comminuted SiGe alloy powders (1200 ℃). This indicates that sintering of ultra-fine grain powders occurs at a much lower temperature than with large grain materials. This may be related to the small surface energy of ultra-fine grains, or to the fact that the energy barrier of inter-diffusion is much lower in the presence of large amount of Phosphorus. Moreover, the samples with low Germanium compositions require higher press temperatures, as shown in Table 3.3.1. In addition, it is worth pointing out that SiGe sample is very sensitive to hot press temperature. When the temperature is below a certain value, the condensed sample density is too low to have a good electrical conductivity. When the press temperature is too high, the as-made sample exhibits some cracking near the surface, as shown in Table 3.3.2, which may be due to large local strain present during hot press. Even in the right temperature range, a small temperature difference can cause large differences in thermoelectric transportation properties, mainly due to porosity of the sample, which will be discussed in the next chapter. Here, for simplicity, theoretical densities of SiGe samples are just left as a linear interpolation of densities of Si, Ge and P.

Table 3.3.1 Hot press conditions for samples with different Si/Ge compositions

| Sample Composition | Ball mill Time (hrs) | Press conditions | Density ($g/cm^3$) | % density |
|---|---|---|---|---|
| Si90Ge10P2 | 25 | 1040, 2 min | 2.60 | 99.5 |
| Si84Ge16P2 | 25 | 1030, 2 min | 2.78 | 99.8 |
| Si80Ge20P2 | 25 | 1020, 2 min | 2.903 | 99.9 |
| Si75Ge25P2 | 25 | 1020, 2 min | 3.046 | 99.8 |

Table 3.3.2 Density of different $Si_{80}Ge_{20}P_2$ samples with different hot press temperatures

| Sample ID | Ball mill time (hrs) | Pressing Conditions | Density ($g/cm^3$) | % density |
|---|---|---|---|---|
| XW0069 | 30 | 990, 2 min. | 2.851 | 98.4 |
| XW0070 | 30 | 1000, 2 min. | 2.875 | 99.2 |
| XW0067 | 30 | 1020, 2 min. | 2.903 | 100.2 |
| XW0064 | 30 | 1030, 2 min. | 2.900 | 100.2 |
| XW0072 | 30 | 1040, 2 min | N/A | Broken |
| XW0074 | 30 | 1050, 2 min. | N/A | Broken |

After the die cooled to room temperature, a saw was used to cut out the disc sample without any damage to the sample. Direct injection failed in a SiGe system because of large

stress created by the thermal expansion difference between SiGe and graphite at high temperatures. After a disc sample of 12.8 mm diameter and 2-3 mm thickness (Fig. 3.3.6) was taken out, it was polished well for thermal conductivity measurement. It was then cut into a bar for the power factor measurement.

As discussed in first chapter, geometric error contributes about 5% error of properties measurement in some cases. In our thermoelectric property measurement, uniform dimensions in all directions are very important for accurate measurement. Fig. 3.3.7 shows a picture of our polishing system. A 2-inch long steel rod and a brass hub with a transition fit were designed. A sample is attached by glue on the top of the steel rod, and the hub guides a vertical position of the steel rod. 320 and 1200 sand paper are utilized to polish the surface. By using such a polishing system, normally, less than 1% error is obtained on the dimension uniformity of both disc and bar samples.

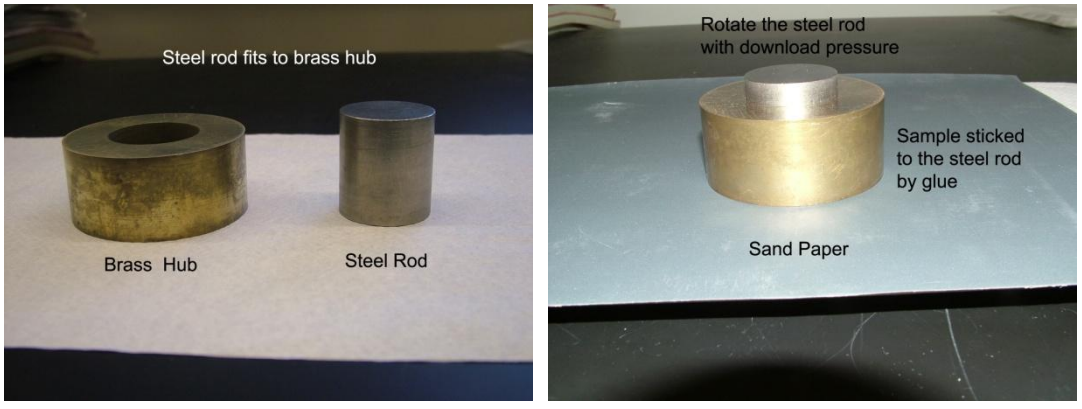


**Fig. 3.3.7.** Pictures of our polishing system.

### 3.3.3. Microstructures of As-pressed nano Samples.

The microstructures of the $Si_{80}Ge_{20}P_2$ samples were first investigated by XRD. Fig. 3.3.8 shows the XRD spectra of the as-prepared nano powder (bottom spectrum) and as-pressed dense bulk sample (top spectrum). It is clear that all the peaks of the as-prepared nanopowder show a weak shoulder on the left side, which can be attributed to the incomplete alloying during the ball milling. Calculation from the XRD spectra using the Williamson-Hall method, as described in the second chapter, results in an average grain size of 12 nm. Meanwhile, the as-pressed dense bulk sample show strong symmetrical peaks, indicating the formation of a homogeneous crystalline single-phase alloy after direct current hot press. Using the same calculation method, an average of 22 nm was obtained as the grain size for the hot pressed samples. It is important to point out that the grain size after hot press is not much larger than that before the hot press, which indicates that there was no significant grain growth during the hot press. However, the stress inside the as-pressed samples is much smaller than that of the as-prepared nanopowders, with the value being 10 times lower in the hot pressed samples, this smaller stress is understandable since hot pressing temperature is above 1000 degree C that anneals the stress built up in the nanopowders during the mechanical alloy process.

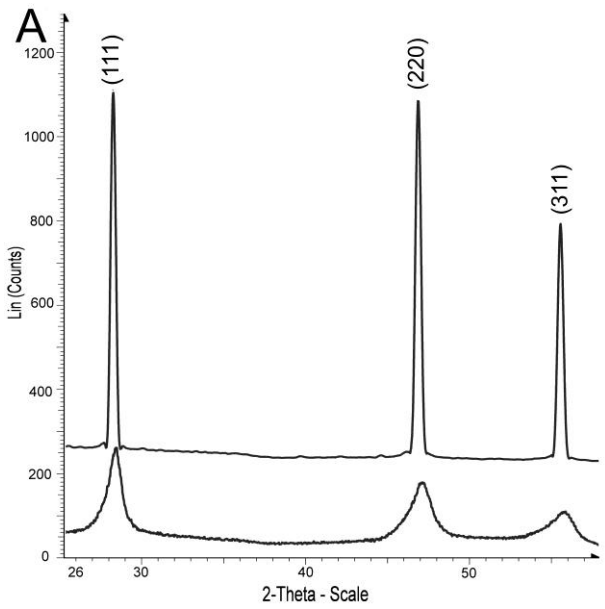


**Fig. 3.3.8.** XRD patterns of typical ball milled nanopowders and as-pressed sample.

The microstructures of as-pressed dense bulk samples are further investigated by TEM, as shown in Fig.3.3.9. Fig. 3.3.9a shows a low magnification TEM image of the as-pressed dense bulk samples. As we can see, the typical grain sizes are in the range of 10 – 20 nm, which comes close to the size (5 – 15 nm) observed in the TEM image (Fig. 3.3.5c) of the as-prepared powders. A HRTEM image (Fig. 3.3.9b) of the as-pressed samples showed that the adjacent grains have similar crystal structure but different crystalline orientations. We believe that these small grains with random crystalline orientations, as shown in Fig. 3.3.9b, help to slow down the phonon transport much more effectively than the larger grains in bulk SiGe materials. A similar phenomenon is observed in the case of SiGe superlattices [28]. The composition of as-pressed sample was examined by EDS, as shown in Fig. 3.3.10. The SiGe composition of the as-pressed sample is quite uniform from micro to nano range. Here, the

reason for why P concentration is less than 2% is that some of P was evaporated during TEM sample preparation and TEM observation since electron beam has enough energy to melt P (the melting point of P is less than 50 degree C).

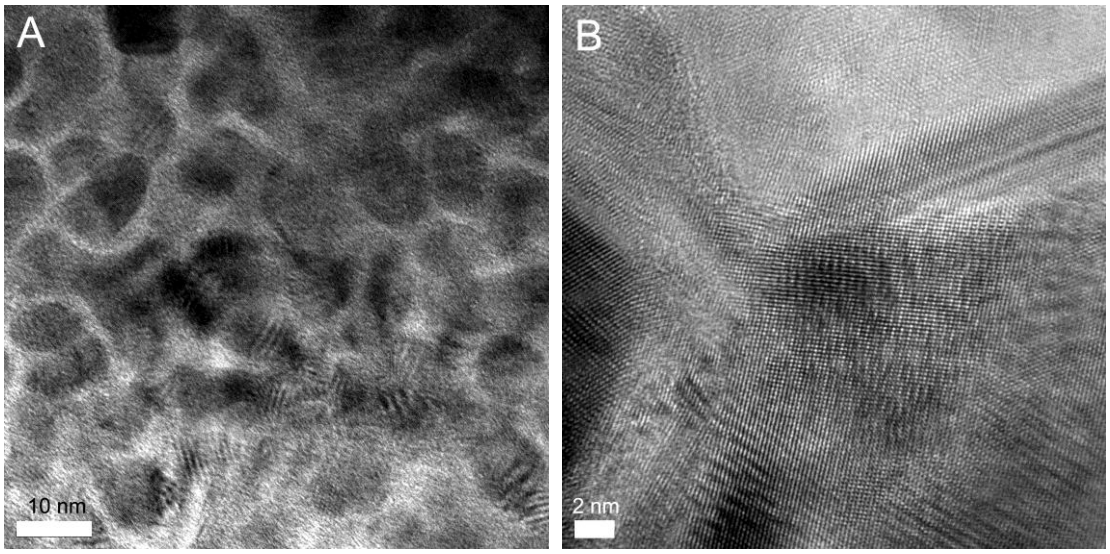


**Fig. 3.3.9.** TEM images with low- (A) and high- (B) magnifications of the as-pressed nanostructured samples.

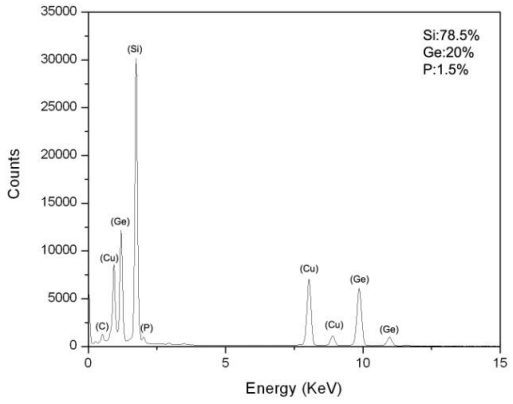


**Fig. 3.3.10.** Typical EDS of as-pressed sample.

### 3.4. Results and Discussion on the Best Samples with $Si_{80}Ge_{20}P_2$ Ratio

Silicon Germanium alloys have been the exclusive choice for radioisotope

thermoelectric generators (RTGs) launched by the U.S. since 1976. Most of these alloys have the composition of about 80% Si and 20% Ge because the material with such composition shows highest ZT, which is about 0.93 at 900 degree C. So we chose a starting composition of $Si_{80}Ge_{20}$. After the optimization of carrier concentration, ball mill and hot press condition, the best sample was shown to be 80% Si, 20% Ge and 2% P. Fig.3.4.1 Shows thermoelectric properties of $Si_{80}Ge_{20}P_2$ in comparison with the commercial state of the art SiGe materials for NASA space application.

As we explained in first chapter, the main advantage of using nano alloy powder for thermoelectric application comes from the fact that there is a large difference in the mean free path between electrons and phonons: about 5nm for electrons and 2-300 nm for phonons in highly-doped samples at room temperature. In addition, it is worth noting that the effective phonon mean free path is even larger since most heat is carried by long wavelength phonons. Thus, nanostuctures with appropriate dimensions can significantly reduce phonon thermal conductivity without creating too much penalty to electrical conductivity. Fig.3.4.1c shows the temperature-dependent thermal conductivity of typical $Si_{80}Ge_{20}P_2$ samples. The data from RTG reference with grain sizes of 1-10 micrometers is included for comparison. Here, the thermal conductivity was calculated as the product of the thermal diffusivity measurement by laser flash, with the volume mass density measured by the Archimedes technique, and the measured heat capacity that agrees with theoretical calculation within 2%. It is clearly shown in Fig.3.4.1c that the sample with nanostructures have a much lower thermal conductivity

than the reference RTG sample. From the electrical conductivity of both samples (Fig.3.4.1), the electrical contribution to the thermal conductivity can be estimated using the calculated Lorentz number (2.14 for high doped SiGe system at room temperature) and the Wiedemann-Franz law [27]. For reference RTG sample, $k_e$=0.77 W/m*k at room temperature with an electrical conductivity of $1.2*10^5$ S/m, whereas for a typical nanostructure dense bulk sample, $k_e$=0.55 W/m*k at room temperature for electrical conductivity of $0.85*10^5$ S/m. By subtracting the electronic contribution from the total thermal conductivity, the lattice thermal conductivity of nanostructure samples is 1.8 at room temperature, about 47% of the lattice part of the reference RTG sample this is mainly due to a strong boundary phonon scattering in the nanostructure samples. Theoretically the lattice thermal conductivity is still the dominant heat transport mechanism at high temperatures up to 1000 degree C. Therefore, additional point inclusion particles may be helpful to further decrease the thermal conductivity. Some preliminary results on those experiments will be summarized in next chapter.

Before the creation of nanostructured materials, it was believed that the lower limit to the thermal conductivity was set by the value obtained by an alloy, as termed the “alloy limit”, for example, the alloy limit for SiGe is 4 W/m*k. The possible mechanism of why nanocomposites can further reduce thermal conductivity is explained as follows. Phonons in a material have very broad spectrum, and phonons with different wavelength contribute to the total thermal conductivity. The alloying most likely scatters short wavelength phonons

while having less effect on mid- to long-wavelength phonons, similar to Rayleigh scattering. Thus, in traditional SiGe alloy, mid- to long-wavelength phonons are still able to transport heat, and actually a substantial fraction of the heat in Si system is carried via mid- to long-wavelength phonons [29]. As a result, by creating grains with a larger characteristic length than that of an impurity atom, grain interface scattering mechanism is introduced to further reduce thermal conductivity to the value lower than the alloy limit.

Figure 3.4.1a shows electrical properties of $Si_{80}Ge_{20}P_2$ in comparison with the commercial state of the art SiGe materials for NASA space application. From Fig. 3.4.1a, it is clearly seen that the electrical conductivity of our nanostructure sample is lower than that of the RTG reference in the low temperature region, mainly because electrons were scattered more at the boundaries of the nanograins below 300 degree C in spite of a similar electron carrier concentration (~$2.3*10^{20}$ $cm^{-3}$). Thus a lower mobility was measured in the nanostructure sample, leading to lower electrical conductivity of around 25 $cm^2/Vs$. However, at the high temperature region above 750 degree C, the difference of the electrical conductivities on both types of samples is very small since intrinsic phonon scattering dominated both the bulk and nanostructure samples.

In regard to Seebeck coefficient, as shown in Fig. 3.4.1c, there is no significant difference at low or high temperature regions, mainly due to the fact that the Seebeck coefficient depends more on the carrier concentration instead of the carrier mobility. And although we add 2% P into SiGe matrix, three times the P concentration of the RTG reference

sample, the solubility of P in Si or Ge is limited to 0.5 to 1% at all temperatures up to 900 degree C. Thus the actual amount of P acting as dopant is normally less than 1%. All other remaining P most likely are located around the grain boundary area because of low surface energy. From EDS (Fig. 3.4.2), the actual P concentration inside grain is about 0.7%, which is equal to $2.3*10^{20}$ $cm^{-3}$, which is similar to the value of RTG reference sample.

Figure 3.4.3 shows the ZT as a function of temperature for the nanostructure samples and the RTG reference. For the nanostructure sample, the ZT value shows a maximum of about 1.3 at 900 degree C, which is about 40% higher than that of the RTG reference. The significant improvement in ZT is mainly attributed to the thermal conductivity reduction. As we mentioned before, this reduction of the thermal conductivity is strongly correlated to the nanostructure features in our sample. In comparison, a previous study on n-type SiGe with grain size down to 1 micrometer has a thermal conductivity of about 72% of its bulk counterpart, but an electrical conductivity 68% of that of its bulk counterpart, leading to no improvement in ZT [30]. Our results show that by reducing grain size into nanostructures. ZT improvement can be achieved by reducing thermal conductivity more than electrical conductivity. And if we can further decrease the grain size, it should be possible to obtain even lower thermal conductivity. However, sizes of nanoparticles from mechanical alloying method is usually limited to 20-30 nm [31]. If a new technique is developed to produce SiGe alloy particles less than 10 nm, then we believe even higher ZT can be obtained since at that size range quantum effects will help to improve both the

electrical conductivity and the Seebeck coefficient.

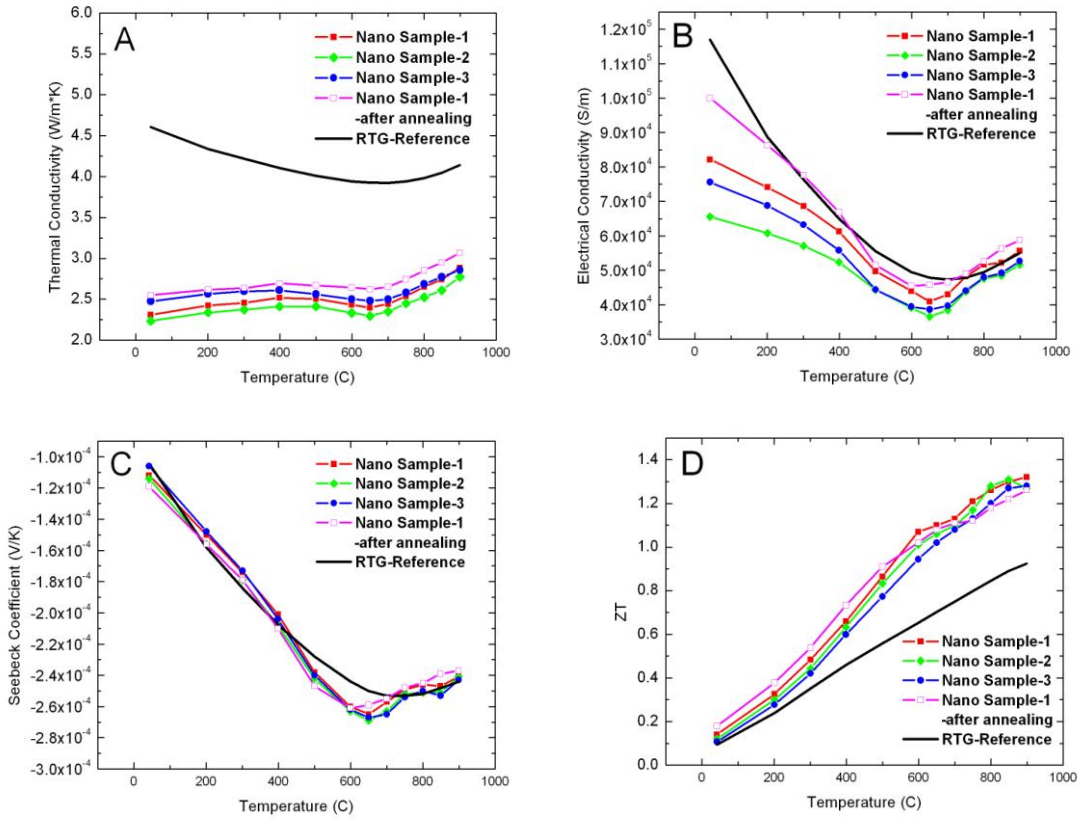


**Fig. 3.4.1.** Temperature dependence of thermal conductivity (A), electrical conductivity (B), Seebeck coefficient (C), and dimensionless ZT (D) on both as-pressed nanostructured samples (filled symbols) and RTG reference sample (solid line), and the open squares are for the sample after annealing at 1050°C for 2 days in air.

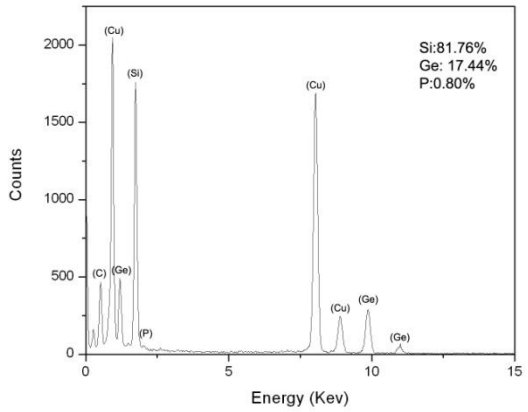


**Fig. 3.4.2.** Typical EDS of one individual grain.

Thermal stability of the nanostructure samples is a serious concern for thermoelectric materials since the thermoelectric devices are required to operate at high temperatures for many years. A thermal stability test was carried out by annealing the nanostructure samples at 1050 degree C for 2 days in air and no significant property degradation was found (shown as the open squares in Fig. 3.4.1). From both the XRD and TEM studies of samples, we also did not find obvious differences in structure and grain size distribution. The possible reason for no grain growth during the extended annealing at high temperature is probably because that all grains have similar size and with random crystalline directions so that the driving force for grain growth is low.

Direct measurement of energy conversion efficiency is difficult at this high temperature. Here, we present only a brief discussion on the potential efficiency that can be realized with the reported ZT. We have calculated the maximum theoretical efficiency of thermoelectric generators based on the measured temperature dependent experimental data.

Fig. 3.4.3 shows the calculated efficiency as a function of the cold-side temperature at different hot-side temperatures. For comparison, also shown in the figure are the results assuming temperature-independent properties with ZT=1 for a hot-side temperature at 1000 degree C. These efficiency values suggest potential applications in solar thermal to electricity energy conversion and waste recovery, in addition to radioisotope applications.

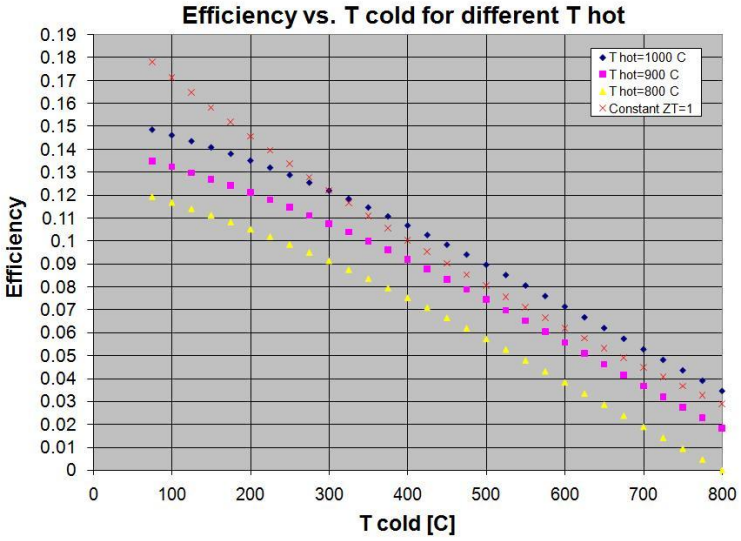


**Fig. 3.4.3.** Theoretical power generator efficiency vs. T cold for different T hot.

## 3.5. Precipitation of Phosphorus in SiGe nano Samples

Generally, phosphorus atoms diffuse via self-interstitial in SiGe, even though many other dopants diffuse primarily via vacancies [32]. The high energy ball milling creates a high density of defects (both point defects and dislocations) inside the material, especially around grain boundaries. At the core of those dislocations, dangling bonds exist and they tend to form stable covalent bonds by capturing charge carriers. Therefore it is possible that a small impurity such as P might reside in the dislocation area around grain boundaries. In

addition, when more P than the solubility limit is added into SiGe alloy, some of the excess P atoms are trapped at the grain boundaries since phosphorus-vacancy complexes are likely to form around grain boundaries during ball milling. However, as the temperature increases, thermal energy may activate those P-v complexes. Thus, more P atoms begin to diffuse into SiGe matrix, leading to high electrical conductivity. When the temperature drops, excess P atoms might be trapped around grain boundaries again, leading to low electrical conductivity.

In order to understand the above P behaviors in nano SiGe alloys, an in-situ experiment was carried out in a ZEM-3 unit since a new feature of ZEM-3 equipment allows researchers to measure electrical conductivity and Seebeck coefficient as the temperature decreases. The results of one typical $Si_{80}Ge_{20}P_2$ sample are shown in Fig. 3.5.1, the red line represents the electrical conductivity as a function of temperature when the chamber is heating up, while the blue one shows the electrical conductivity as a function of temperature when the chamber is cooling down. Clearly, the electrical conductivity during cool down period is lower than that during heating period, indicating the precipitation of P during cooling. Hall measurement results also confirm that carrier concentration dropped about 10% percent during cooling while hall mobility is maintained, as shown in Fig. 3.5.2 and Fig. 3.5.3. However, these precipitated P atoms can be activated again through a reset process, as we can see from the pink curve in Fig. 3.5.1. In addition, precipitation happens only below 600 degree C, as shown in Fig. 3.5.4. There is no indication of P precipitation when the nano samples are kept above 600 degree C. one possible explanation is that when the temperature

is above 650 degree C, intrinsic carriers start to dominate the electrical transport.

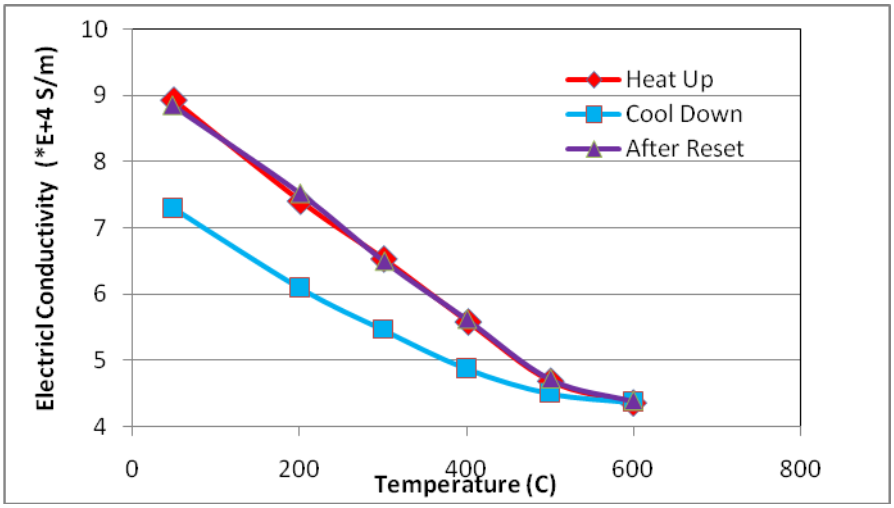


**Fig. 3.5.1.** Electrical Conductivity of typical SiGe nano sample below 600 degree C during heating and cooling period and after reset.

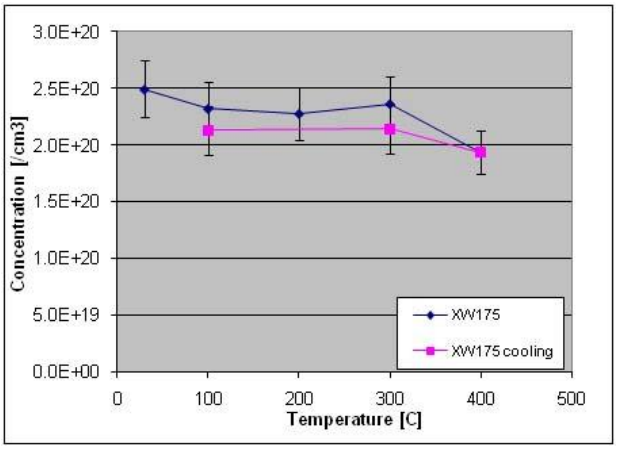


**Fig. 3.5.2.** Temperature dependence of carrier concentration in a typical nano SiGe sample.

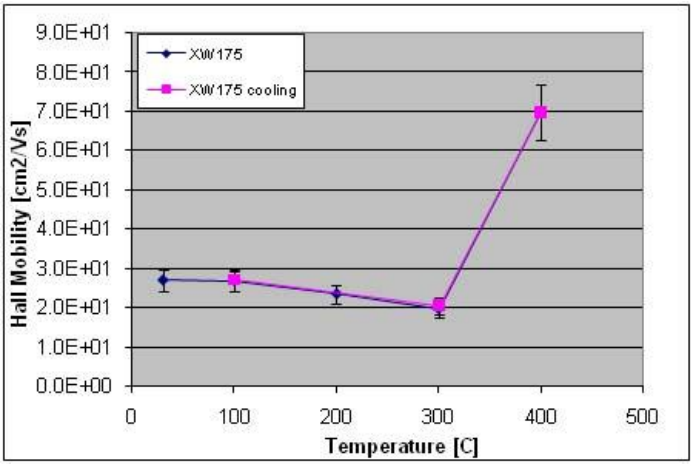


**Fig. 3.5.3.** Temperature dependence of hall mobility in a typical nano SiGe sample.

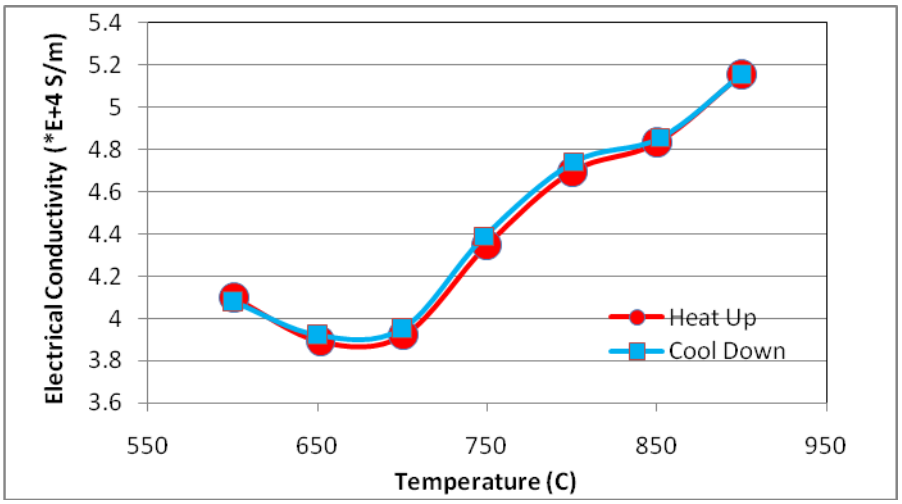


**Fig. 3.5.4.** Electrical conductivity of typical SiGe nano samples above 600 degree C during heating and cooling period.

## 3.6. Isotropic Thermoelectric Properties of nano SiGe Samples

The SiGe alloy has the same diamond crystal structure as Si, and consequently, theoretically their transport properties should be isotropic. However, since we applied a constant force on the as-made SiGe powder during hot press, an examination of thermoelectric property dependency on crystallographic direction is needed to be carried out, as described by following.

Since the size of our regular die is limited and the minimum length of the sample for electrical conductivity is 12nm, a much large die is needed to examine the isotropic thermoelectric properties of the SiGe alloy, which has a length of about 75 mm and an inner diameter of about 25 mm. Thus around 25 gram of SiGe alloy powder was put into a larger die. After the hot press, cylinder-like discs were obtained and cut both along and perpendicular to the press direction and were then measured. The results are shown in Fig. 3.6.1. As we can see from the figure, the difference for both electrical conductivity and Seebeck coefficient are within 5% at all temperature ranges, leading to similar power factors for samples under different directions. Regarding thermal conductivity, both samples at 0 or 90 degree C agree within 6%. The results confirmed that our fabrication technique has the ability to grow nano SiGe alloys with isotropic thermoelectric properties, although further experiments are needed to optimize the ball mill and press conditions when the large die is used and a large amount of SiGe nano powder is loaded.

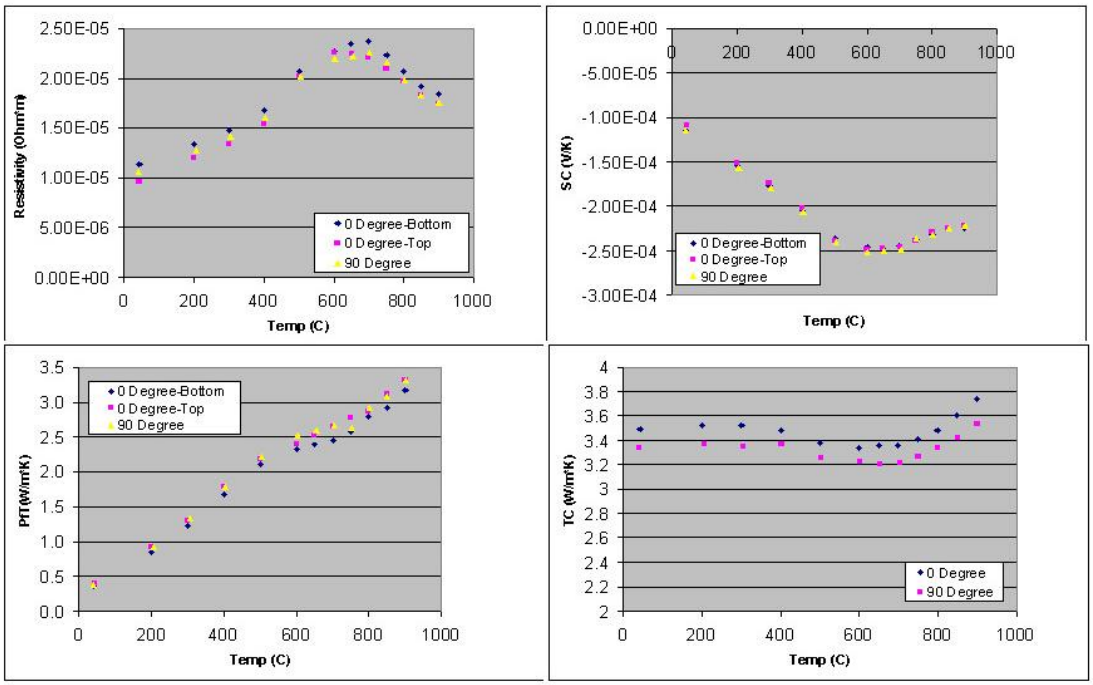


**Fig. 3.6.1.** Thermoelectric properties of SiGe samples cut from 0 or 90 degree direction.

## 3.7. Summary

In conclusion, a cost-effective and mass-producible experimental process, based on the nano approach, has been demonstrated to produce dense bulk SiGe alloyed nanostructured materials with high thermoelectric properties. The experimental process included two steps. First, mechanical alloying was used to produce alloyed SiGe nanopowder. XRD spectrum results indicated that alloyed powder was formed after 25 hour (Spex 8000) or 110 hours (Glen mill) of ball milling. TEM observation confirmed that nano SiGe polycrystalline particles appeared after ball milling. Second, a direct current hot press technique was used to compact the nanopowder into bulk dense alloy. TEM results showed that typical grain sizes were in the range of 10-20 nm (Fig. 3.3.9 A). HRTEM result showed that the adjacent grains have similar crystal structure but different crystalline orientations. A maximum ZT value of 1.3 at 900 degree C has been observed on the nano sample with the composition of $Si_{80}Ge_{20}P_2$ (Fig. 3.4.1), which is about 40% high than that of currently used RTG samples (0.9). Since the size of nanograins is still much larger than the mean free path of electrons in the SiGe system (5 nm), the power factor of the nano samples has similar value as the RTG reference sample especially in high temperature region. However, compared to commercial SiGe ingots with grains of micron size, nanotructured samples shows much lower thermal conductivity (about 40% lower) because of a large reduction of lattice thermal conductivity. The lattice thermal conductivity reduction is mainly due to enhanced phonon scattering at the increased boundaries of the nanograins.

## 3.8. References


1. C. Winkler, *Berichte der deutschen chemischen Gesellschaft,* **19**, 210 (1886).
2. M. Shima, M. Isomura, H. Haku, M. Tanka, K. Wakisaka, *Sanyo Technical Review,* **29**, 9 (1997).
3. J. Campos, P. Corredera, A. Pons, A. Corrons, *Fiber-Optic Metrology,* **1504**, 66, (1957).
4. A. S. Cooper, *Acta Cryst.*, **15**, 578 (1962).
5. G. Moore, Electronics, **38**, 8 (1965).
6. Y. Zheng, C. Rivas, R. Lake, K. Alam, T. B. Boykin, and G. Klimeck, *Transactions on electron devices*, **52**, 1097 (2005).
7. L. Y. Chen, W. H. Chen, and F. C. N. Hong, *Appl. Phys. Lett*., **86**, 193506 (2005).
8. Y. Cui, Z. H. Zhong, D. L. Wang, W. U. Wang, and C. M. Liber, *Nano. Lett.*, 3, 149 (2003).
9. B. Abeles, D. S. Beers, G. D. Cody, and J. P. Dismukes, Phys. Rev., **12**5, 44 (1962).
10. C. Wood, *Rept. Prog. Phys.*, **5**1, 459 (1988).
11. J. P. Fleurial, 5th workshop on SiGe, ITC, Waltham, 11 (1989).
12. S. M. Lee, "*The Fabrication and Thermoelectric Properties of Amorphous Si-Ge-Au bulk samples" MRS Fall, Symposium. G* (2001).
13. M.-S. Jeng, R.G. Rang and G. Chen, "*Monte Carlo Simulation of Thermoelectric Properties of Nanocomposites,*" ICT05, June 19, Clemson, (2005).

14. L. D. Hicks, M. S. Dresselhaus, *Physical Review* B, **47**, 12727 (1993).

15. D. Vashaee, A. Shakouri, *Journal of Appl. Phys.* **101**, 53719 (2007).

16. A. I. Hochbaum, R. K. Chen, R. D. Delgado, W. J. Liang, E. C. Garnett, M. Najarian, A. Majumdar, and P. D. Yang, *Nature*, **451,** 163 (2008).

17. A. I. Boukai, Y. Bunimovich, J. T. Kheli, J. K. Yu, W. A. Goddard, and J. R. Heath, *Nature*, **451**, 168 (2008) .

18. G. Chen, *Phys. Rev. B*, **57**, 14958 (1998).

19. B. Poudel, *et al.*, *Science*, 320, 634 (2008).

20. Y. Ezzahri, G. Zeng, K. Fukutani, Z. Bian, A. Shakouri, *Microelectrionics*, **39**, 981 (2008).

21. A. Borshchevsky, J. P. Fleurial, J. W. Vandersande, and C. Wood, *In Proc. 7th Symp. Space Power Syst.*, Albuquerque, **229,** (1990).

22. T. Caillat, M. Carle, D. Perrin, H. Scherrer, and S. Scherrer, *J. Phys. Chem. Solids*, **53,** 227 (1992).

23. R. M. Davis, and C. C. Koch, *Scr. Metall.*, **21**, 305 (1987).

24. B. A. Cook, B. J. Beaudry, J. L. Harringa, and W. J. Barnett, *Proc. Intersociety Energy Conversion Engineering Conference*, Vol. **2**, New York, 693 (1989).

25. *CRC Handbook of Thermoelectrics,* edited by D. M. Rowe, CRC Press, Boca Raton, FL, 1995, 127.

26. G. K. Williamson, W. H. Hall, *Acta Metal.*, **1**, 23 (1953).

27. J. B. Nelson, and D. P. Riley, *Proc. Phys. Soc*., **57**,160 (1945).

28. T. B. Tasciuc, *et al.*, *Superlattices and Microstructures*, **28**, 749 (2000).

29. A. J. Minnich, M. S. Dresselhaus, Z. F. Ren, and G. Chen, *Energy Environ. Sci.*, online published (2009).

30. C. B. Vining, W. Laskow, J. O. Hanson, V. D. Beck, P. D. Gorsuch, *J. Mater. Chem.* **69**, 4333 (1990).

31. V. Svrcek, J. L. Rehspringer, E. Gaffet, A. Slaoui, and J. C. Muller, *J. Crystal. Growth.* **275**, 589 (2005).

32. C. Janke, R. Jones, S. Oberg, and P. R. Briddon, *Phys. Rev. B*, **77**, 195210 (2008).

# Chapter 4

# Optimization of Thermoelectric Properties on Nanostructured n-SiGe Materials

This chapter will discuss the detailed experimental data of many as-made SiGe nano samples with different compositions, different press conditions, and different inclusions. Since elemental Ge is about 10 times more expensive than elemental Si, the Ge composition needs to be well controlled in order to produce SiGe thermoelectric material at low cost with high ZT. Also, as described in the first chapter, especially for semiconductor thermoelectric materials, the carrier concentration needs to be optimized in order to obtain better device performance, i.e. high ZT [1-2]. In addition, press parameters should be well controlled in order to obtain dense samples without any mechanical cracks or other defects, as shown in the reference [3]. Samples with different densities have very different thermoelectric properties, and thus various samples with different densities, usually controlled through different press temperatures, were made to investigate the effect of porosity. Moreover, as we pointed out in the third chapter, point defects are very effective at scattering phonons with short wavelengths while grain boundaries tend to scatter phonons with mid- or long-wavelength. Thus, a few samples with different point inclusions were made and the measurement data is given in this chapter as well.

## 4.1. Germanium Composition Optimization

For a traditional SiGe alloy, Fig. 4.1.1 shows thermal conductivity as a function of Ge composition. As we can see from the figure, only a certain range of germanium provides relatively low thermal conductivity compared to pure Si and Germanium [4]. Based on this fact, along with the high cost of the Ge element (10 times more expensive than Si), a series of experiments from 10% Ge and 25% Ge were done to investigate the effect of germanium composition on the thermoelectric properties of the nanostructured SiGe alloy.

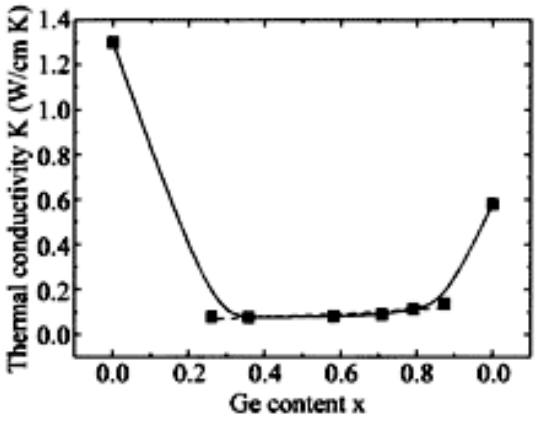


**Fig. 4.1.1.** The thermal conductivity of traditional SiGe alloy as a function of Ge content.

Figure 4.1.2A shows the thermal conductivity of samples with different germanium compositions as a function of temperature. Here, it is worth pointing out that all the samples had a similar density percentage (99-100%) compared to theoretical density since porosity plays a very critical role in thermoelectric properties, as described in the corresponding section. Form the figure, it is clear that 20% percent Germanium provided us with the lowest thermal conductivity, any other samples with different amount of germanium gave higher

thermal conductivity. This is different from bulk SiGe alloys as they show that the alloys with 20% to 80% percent germanium composition have very similar thermal conductivity. This may be related to the nano structure of our sample since most of the long-wavelength phonons were scattered by nano boundaries. Moreover, alloy scattering in SiGe system is very efficient at scattering phonons, which leads to a significant reduction of the lattice thermal conductivity as compared to pure bulk Si or Ge. With only a 10% Ge addition, the thermal conductivity dropped from above 100 W/m*k to around 5 W/m*k, indicating very strong alloy scattering. In addition, all samples showed an increase of thermal conductivity when the temperature reached 750 degree C, At that temperature, bipolar heat diffusion starts to play its role as in the case of bulk SiGe alloy sample [5].

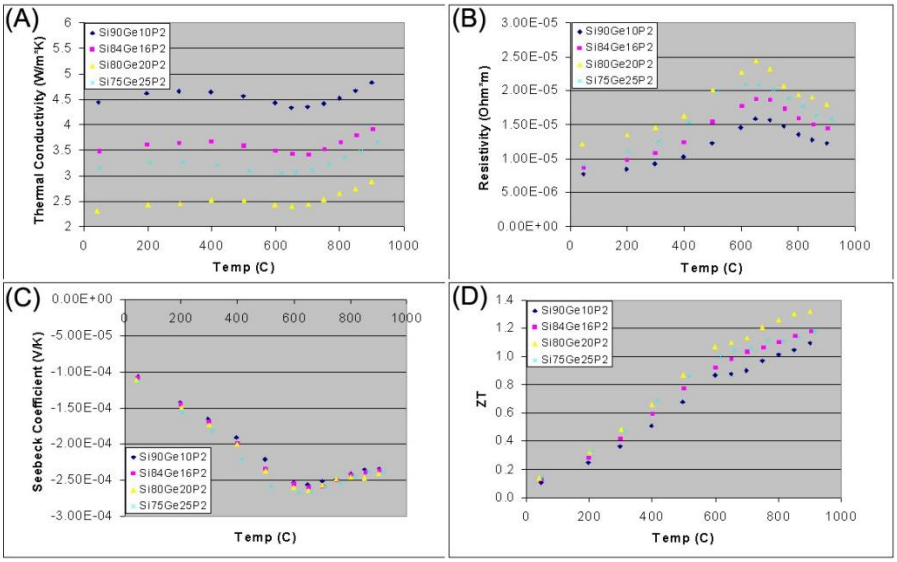


**Fig. 4.1.2.** Temperature dependence of thermal conductivity (A), resistivity (B), Seebeck coefficient (C), and dimensionless ZT (D) on nano SiGe samples with different Ge compositions.

Figure 4.1.2B shows the resistivity of samples with different germanium compositions as a function of temperature. It is obvious that the $Si_{80}Ge_{20}$ sample has the highest resistivity, mainly due to lower carrier concentration, as shown in Fig. 4.1.3. The different carrier concentration may be related to the Ge concentration of our sample since nano samples have hall mobility of about 30 $cm^2/Vs$ (Fig.4.1.4). This is slightly lower (10% percent) than that of samples with micron size grains [6], indicating more grain boundary scattering. In addition, all samples show a decrease of resistivity after 700 degree C, as at that temperature intrinsic carriers start to be activated [6].

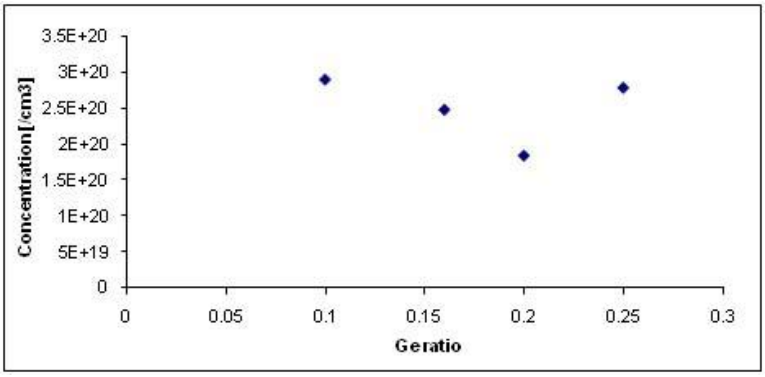


**Fig. 4.1.3.** Room temperature carrier concentration as a function of Ge ratio.

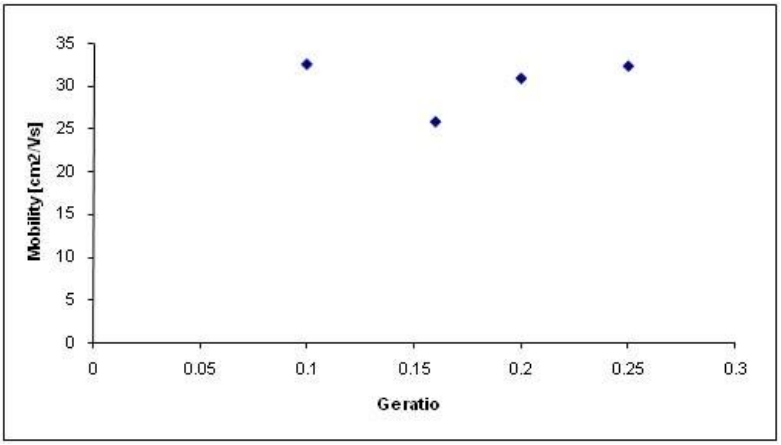


**Fig. 4.1.4.** Room temperature carrier mobility as a function of Ge ratio.

Figure 4.1.2C shows the Seebeck coefficients of the samples with different germanium compositions as a function of temperature. Unlike the thermal conductivity or resistivity figure, there is almost no difference (less than 3%) in the Seebeck coefficient of all samples especially in the low and high temperature regions. This is attributed to the fact that the Seebeck coefficient is mainly related to Fermi level or carrier concentration. Despite Ge ratios, all the SiGe samples have a carrier concentration of the same magnitude [7].

Combining the Seebeck coefficient and resistivity values with the thermal conductivity yields the figure of merit, as shown in Fig.4.1.2D. Since the $Si_{80}Ge_{20}$ sample's thermal conductivity is reduced more than its electrical conductivity, especially at high temperatures, it has the highest ZT values at all points. For example, at 900 degree C, $Si_{80}Ge_{20}$ has about 41% percent lower thermal conductivity than $Si_{90}Ge_{10}$ while electrical conductivity of $Si_{80}Ge_{20}$ is only 28% lower. This leads to a higher ZT Value of $Si_{80}Ge_{20}$ (20% percent) than that of $Si_{90}Ge_{10}$ after accounting for the small difference of 2% in Seebeck coefficient.

## 4.2. Phosphorus Composition Optimization

In the thermoelectric field, carrier concentration optimization is very important to obtain the best thermoelectric performance, as described in the first chapter. So a series of experiments with different P concentration in $Si_{80}Ge_{20}$ were carried out to find the best P composition from 1 to 5%. The results are shown in Fig. 4.2.1. When less than 1% P was

added, only low density samples (less than 85%) were obtained since P itself acts as a sintering agent [8].

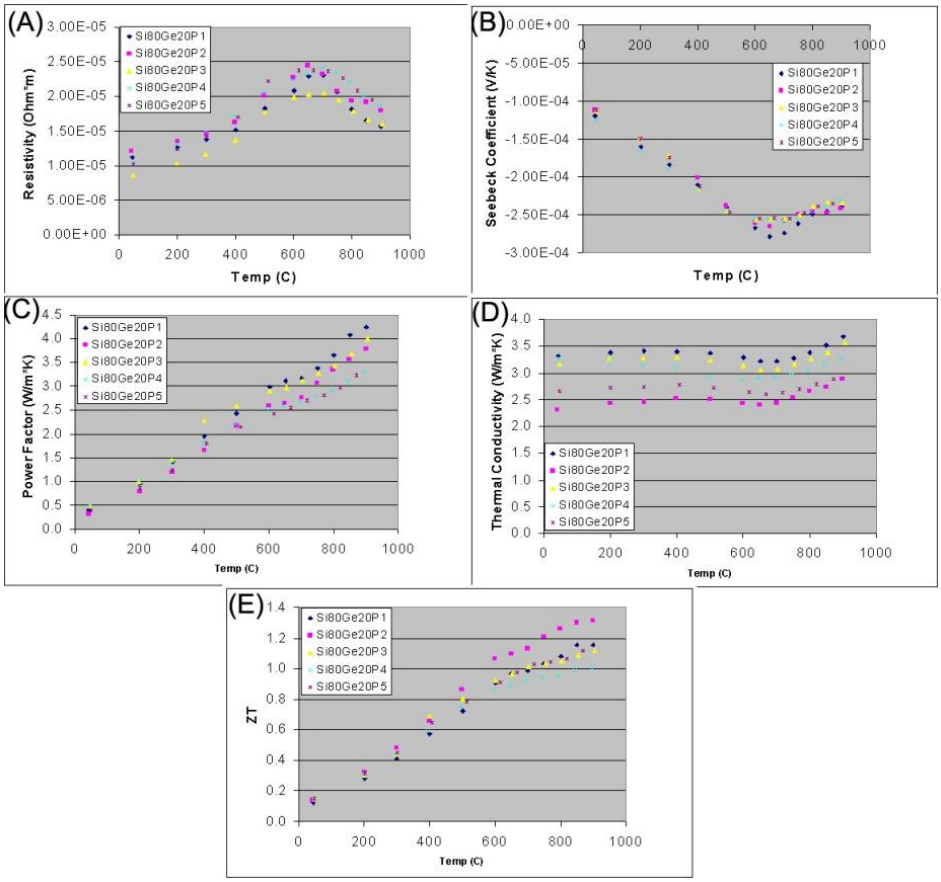


**Fig. 4.2.1.** Temperature dependence of resistivity (A), Seebeck coefficient (B), power factor (C), thermal conductivity (D), and dimensionless ZT (E) on nano $Si_{80}Ge_{20}$ samples with different P compositions.

Figure 4.2.1A shows the resistivity of the samples with different P compositions as a function of temperature. The sample with 3% P shows the lowest resistivity at all temperatures while the sample with 5% P shows highest resistivity at high temperatures. In order to further investigate the effect of P ratio on the electrical transport, a Hall

measurement was made. Fig. 4.2.2 shows the room temperature carrier concentration as a function of P ratio, it is obvious that the sample with 5% P has a significantly lower carrier concentration, leading to the highest resistivity. On the mobility side (Fig. 4.2.3), the sample with 3% P has the highest mobility value, leading to the lowest resistivity.

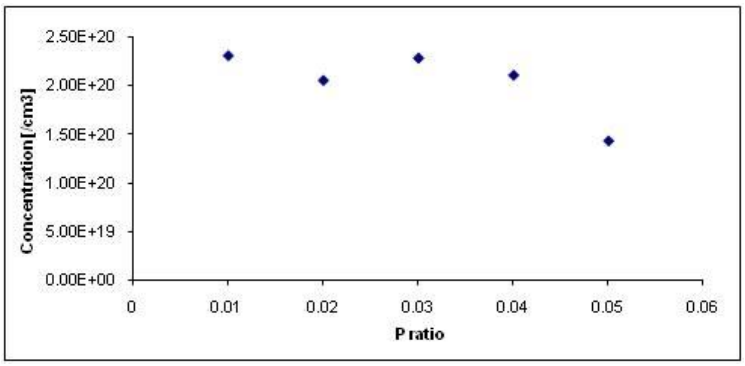


**Fig. 4.2.2.** Room temperature carrier concentration as a function of P ratio.

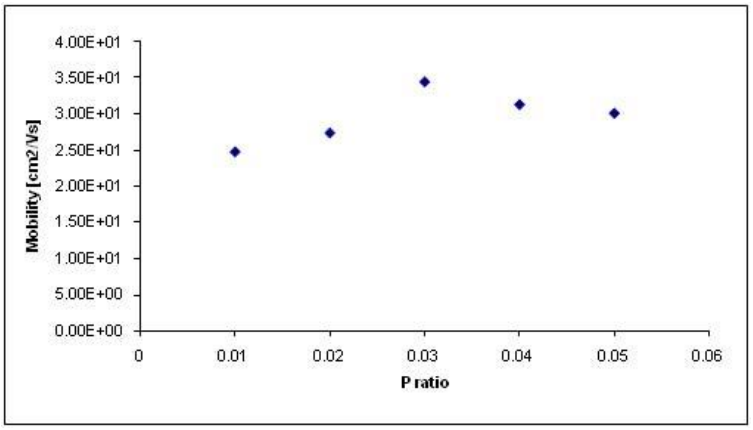


**Fig. 4.2.3.** Room temperature carrier mobility as a function of P ratio.

Seebeck coefficient results are shown in Fig.4.2.1B. At low and high temperatures, very small differences are observed, while in the middle temperature range the sample with 1% shows a higher value (10%) than others. Overall, in regard to the power factor, as shown

in Fig. 4.2.1C, the samples with 1% and 3% P show the highest values, around 3.4 from 500 to 900 degree C. The 2% P sample shows a moderate value of about 3.0 from 500 to 900 degree C while the sample with 4 or 5% have lowest value of about 2.8 at same temperature range, which is consistent with the resistivity results, when the resistivity is low, the power factor is high.

Figure 4.2.1D shows the thermal conductivity of samples with different P compositions as a function of temperature. The sample with 2% P shows the lowest value while others have higher values, especially 1% or 3% P doped samples. Combining this with the power factor data, the results of dimensionless figure of merit are shown in Fig.4.2.1E, the sample with 2% P shows a higher value than other samples, and has a value of about 15% higher than others from 600 to 900 degree C mainly due to its low thermal conductivity.

## 4.3. Ball Milling Time Effect

As we discussed in previous chapters, using the Spex machine, 14 hours ball milling was necessary to alloy Si and Ge. Here several samples of $Si_{80}Ge_{20}P_2$ with different ball mill times were made to determine the optimal ball milling time. The results are shown in Fig. 4.3.1.

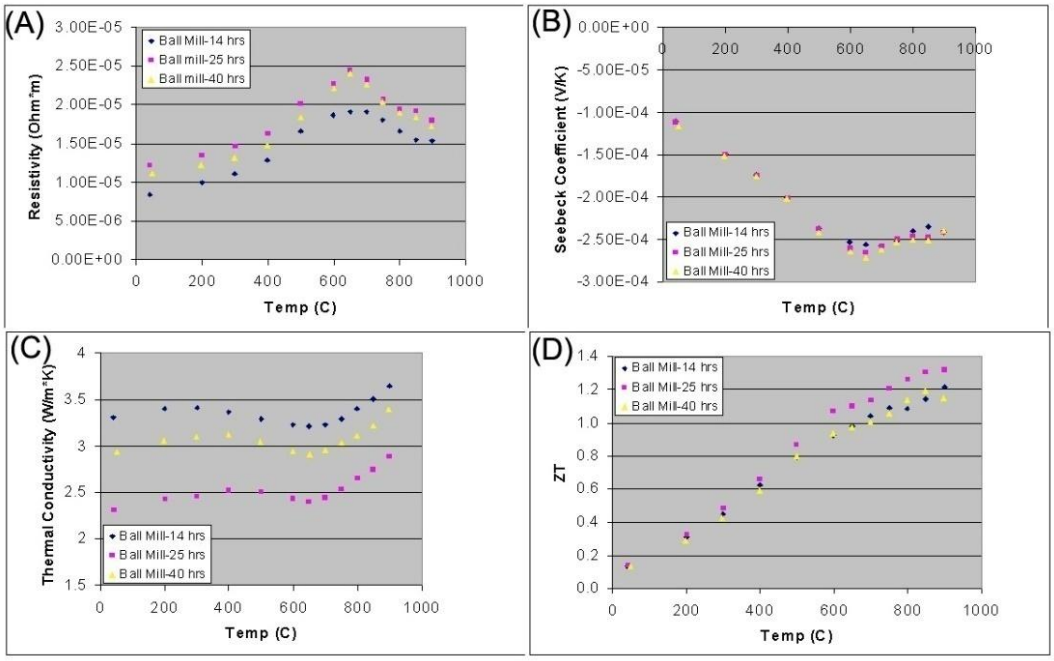


**Fig. 4.3.1.** Temperature dependence of resistivity (A), Seebeck coefficient (B), thermal conductivity (C), and dimensionless ZT (D) on nano SiGe samples with different ball mill time.

Regarding resistivity, the sample with shortest ball mill time has the lowest resistivity, which may be related to a higher mobility because of incomplete alloying. The 25 hrs and 40 hrs ball mill samples have very similar values, around 20% higher than that of the 14 hrs ball milling sample. From the XRD spectrum, after 25 hrs, only a single phase appears indicating alloy formation, which will significantly reduce the mobility, leading to a higher resistivity.

Figure 4.3.1B shows the Seebeck coefficient of the samples with different ball mill times as a function of temperature. Unlike the resistivity, for all three samples, the Seebeck

coefficients are within 5% percent, mainly because the doping level of those samples is same. Overall, a longer ball mill time provides a lower power factor.

Figure 4.3.1C shows the thermal conductivity of the samples with different ball milling times as a function of temperature. The sample with 14 hrs ball milling shows the highest value, which is about 3.5 W/m*K at all temperatures. This is 25% higher than the sample with 25 hrs ball milling because a better alloy quantity helps to scatter phonons to obtain lower thermal conductivity. The sample with 40 hrs shows a value of about 3.1 W/m*K. A possible explanation is that a long ball milling may help small crystallites merge into particles with larger diameters, thus a slightly higher thermal conductivity is observed.

The ZT of the samples with different ball mill times as a function of temperature is shown in Fig. 4.3.1D. Since the sample with 25 hrs has the lowest thermal conductivity, about 30% lower than that with 14 hrs ball milling, while the power factor is only 24% lower than the one with 14 hrs ball milling. The maximum ZT value of the sample with 25 hrs is the highest, about 1.3 at 900 degree C, while the other two samples have a maximum ZT of 1.2. The lower ZT of the sample with 14 hrs ball milling is mainly related to high thermal conductivity coming from incomplete alloying. However, the reason for a lower ZT for the sample with 40 hrs of ball milling is the increase of thermal conductivity, due to aggregation of small crystallites.

## 4.4. Porosity Effect

For SiGe alloys thermoelectric materials, there are lots of fabrication techniques, for example, zone-leveling, grinding and vacuum hot pressing method [9]. In all methods, samples with low densities (~80%) are obtained, and it is believed that the thermoelectric properties of low density samples are poor, especially the electrical conductivity [10-11]. However, those studies mainly focused on a large range of density, and no research work was done on the porous effect at around 100% of the theoretical density, which is the topic of this section.

The presence of porosity in a continuous solid material normally has a geometric effect when the size of those pores is in the micro or mm ranges. If the pore size is less than the phonon wavelength, pores will act as phonon scatters, reducing thermal conductivity [11]. However, electrons can be scattered at the grain-pore interfaces since potential barriers exist at the pore boundaries. Thus, the porosity or the density of the SiGe sample needs to be optimized for a better thermoelectric performance. Actually, when the sample density is measured by the Archimedes technique, it is very easy to identify whether the samples with pores have only geometric effects. When the mass in the water keeps increasing during the measurement, this indicates that water is gradually sinking into the pores of the sample, this type of sample usually only has geometric effect and its electrical conductivity is always much lower than that of the sample with high density.

Figure 4.4.1 shows the thermoelectric properties of $Si_{80}Ge_{20}P_1$ samples with

different densities as a function of temperature. As we can see from the figure, the samples with around 99% density show high ZT while sample swith 93% density show 20% lower ZT. This is mainly due to lower electrical conductivity (70% lower than high density sample at low temperature range and 45% lower than high density sample at high temperature range), although the thermal conductivity value of low density samples is about 25% lower than that of high density sample, which is consistent with the data in the reference [11].

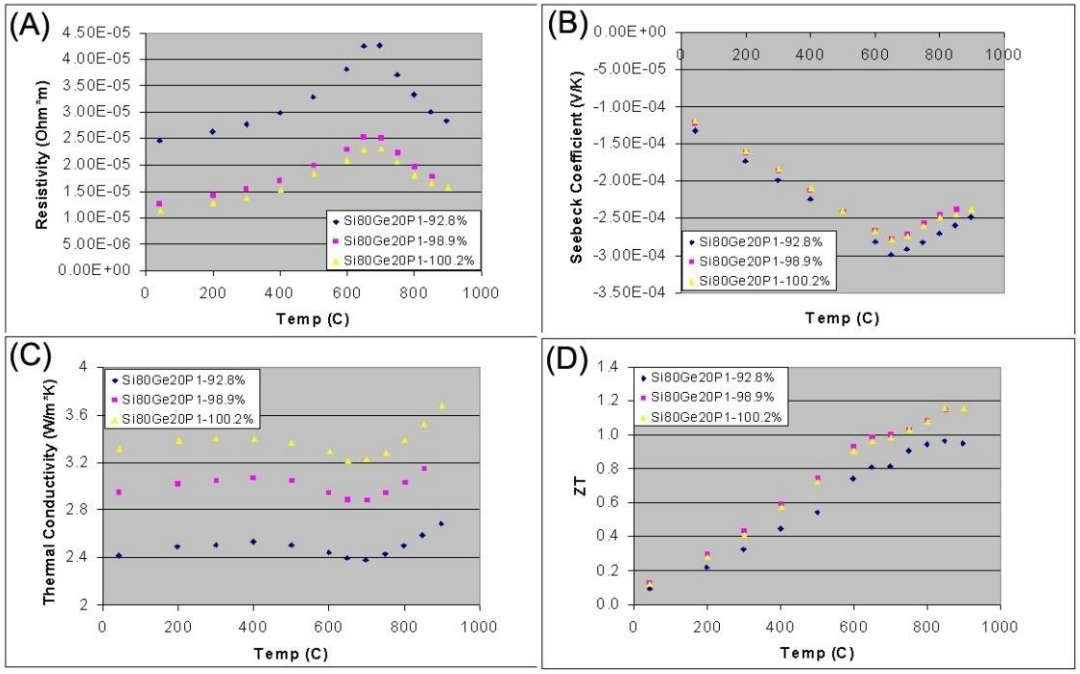


**Fig. 4.4.1.** Thermoelectric properties of nano $Si_{80}Ge_{20}P_1$ samples with different densities.

Figure 4.4.2 shows thermoelectric properties of $Si_{80}Ge_{20}P_2$ samples with different densities as a function of temperature. From the figure, it is clear that the electrical conductivity of the low density sample (95%) has dropped severely, one order of magnitude lower than the samples with above 99% density. However, Seebeck coefficients are similar

for all of the samples, since all samples have the same P concentration. Overall, although the 95% density sample shows about 25% lower thermal conductivity, the ZT value of that sample is very low, the maximum value is 0.65 at 800 degree C, which is about 50% lower than the sample with 99% density.

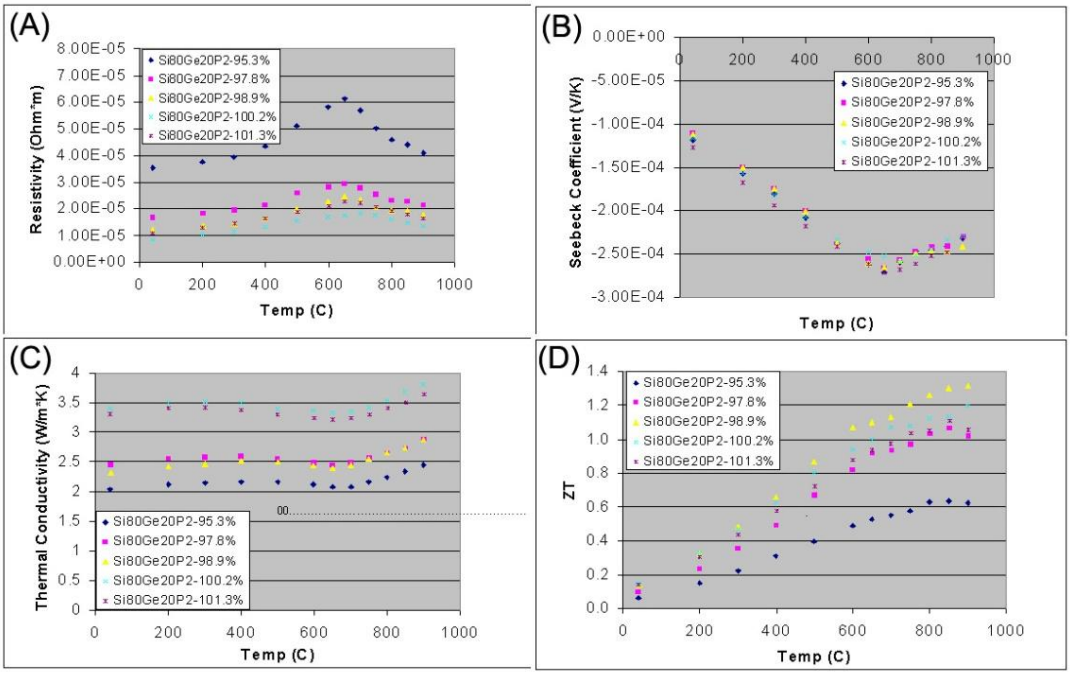


**Fig. 4.4.2.** Thermoelectric properties of nano $Si_{80}Ge_{20}P_2$ samples with different densities.

It is worth pointing out that a few pores may be helpful to reduce the thermal conductivity without too much loss of electron conductivity. As we can see from the Fig. 4.4.2, the sample with 99% density shows highest ZT in all temperature regions although its thermal and electrical conductivity are not the best. We believe this is related to the size effect of small pores. Pores are basically the same as grain boundaries, but may cause more scattering than typical grains since the two sides of the surface of the pore are totally

different, one side is the material, the other side is the void. When the sample density is very close to 100% of theoretical density, both pore density and the size of pores will be small enough to allow electrons to jump through the barrier, caused by the pore, and thus a small reduction of electrical conductivity is observed. However, even if the size of the pores is small, they are still effective in scattering phonons with short-wavelength since a phonon is just a vibration of atoms, whenever the phonons hit the boundaries of the pores, they will be scattered. However, more experiments are needed to classify this phenomena, for example, TEM investigation of the size of those pores and its size distribution, also a theoretical modeling is needed to explain the physics behind this effect.

## 4.5. Results on GaP-doped Samples

For SiGe alloys, P is the most commonly used element for n type doping [12]. However, there is a solubility limit for P in SiGe alloys, normally less than 0.5% at low temperature and 1% at high temperatures. Thus, various efforts are made to improve the solubility of P [13-14]. One proven method is to add GaP to enhance P solubility beyond the maximum equilibrium limit in SiGe alloys [15]. Experimentally, it has also been confirmed that thermoelectric properties can be enhanced by adding GaP into SiGe alloys with large grains produced by zone leveling, liquid phase epitaxy (LPE) and mechanical alloying (MA) [16-17]. It is very promising if we can apply the same technique to SiGe alloys with small grains to obtain even higher ZT. The results are shown in Fig. 4.5.1, for comparison, the data

of $Si_{80}Ge_{20}P_2$ under same hot press conditions is included.

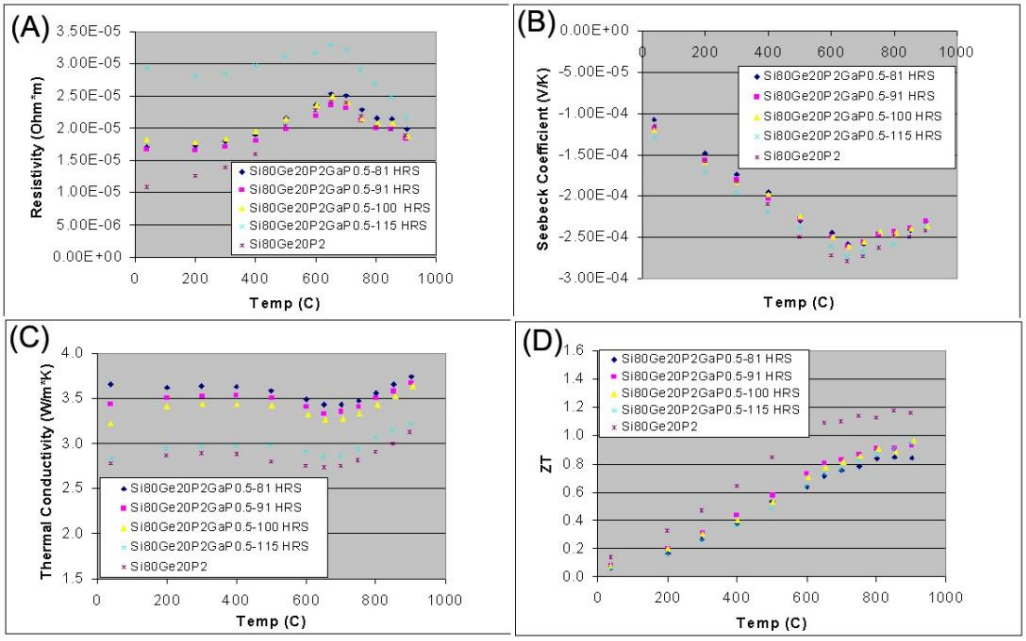


**Fig. 4.5.1.** Thermoelectric properties of nano $Si_{80}Ge_{20}P_2GaP_{0.5}$ samples with different ball mill time.

As we can see from Fig.4.5.1A, it is obvious that all GaP-doped samples have higher resistivity than only P-doped samples, no matter how long the GaP-doped powder is ball milled. This is quite different from the results of the samples from other preparation methods. For example, the vacuum hot pressed micro SiGe alloy sample shows about a 30% enhancement of electrical conductivity when the ratio of P/Ga is below 10 [19]. In addition, Hall measurement shows that the sample with GaP doping has an even lower carrier concentration. The carrier concentration of GaP doped samples is about $1.6*10^{20}$ $cm^{-3}$, on the same order of that of samples only doped with P ($1.9*10^{20}$ $cm^{-3}$). However, the mobility of

the GaP doped sample (20.75 $cm^2/Vs$) is much lower than that of the P doped sample, leading to a lower net electrical conductivity (30.8 $cm^2/Vs$). There are two possible explanations why GaP doping doesn't increase the carrier concentration and electrical conductivity. The first is due to the large amount of P in the nano SiGe sample, usually 2% or more, while in traditional SiGe alloy materials, only 0.5% P is introduced. Extra P in nanostructured samples may suppress the dissolving of P atoms into SiGe matrix even with the help of GaP. As a result, instead of enhancing P solubility, those GaP atoms actually act as impurity scattering centers, leading to a lower carrier mobility. Another possible explanation is related to the nano structure of our samples. Since nanostructured samples have much smaller grains compared to traditional SiGe alloys and P tends to form P-v structures around the grain boundaries because of low surface energy, those enhanced P-v structures may block the dissolving of P atoms around the grain boundaries into the grains.

## 4.6. Results on n-SiGe nano Samples with Different Inclusions

Both Si and Ge belong to the same carbon group in the periodic table, and they have the same diamond lattice structure, and their lattice constant is very close, where Si is 5.43095 A, Ge is 5.64613 A [18]. As a result, Si and Ge are completely miscible under any compositions, leading to very strong alloy scattering, as shown in the last chapter. However, because of the similarities between Si and Ge. They are not very effective at scattering phonons with extremely short wavelengths. Experimentally, our group has reported enhanced

ZT in the CoSb system by adding Yb into the nano CoSb powder [19]. Thus a few inclusions are added into our nano SiGe samples in order to obtain even lower thermal conductivity. In fact, commercial Si or other semiconductor nano particles was first tried as inclusions. However, the electrical conductivity of the SiGe alloy with commercial nanoparticles is too low to have good thermoelectric performance because commercial nano particles were always wrapped with some oxides or organic surfactant. Thus, chunk materials are chosen as inclusions since they can be ground into nano particles during ball milling.

### 4.6.1. Nanostructured SiGe Samples with Ytterbium Addition

1% Ytterbium (Yb) chunks were added into our best sample of $Si_{80}Ge_{20}P_2$ since the beginning of the ball milling. The results are shown in the following figures, as a comparison, the data for nano $Si_{80}Ge_{20}P_2$ sample is included too. It is clear that Yb doesn't have obvious effects on the electrical transport of nano $Si_{80}Ge_{20}P_2$ sample at any temperature. Regarding the Seebeck coefficient, there is no difference between the samples with or without Yb doping at low or high temperatures. However, surprisingly, the thermal conductivity of Yb-doped sample increased by 20%, compared to the sample without Yb-doping, leading to a maximum ZT value of 1.12 at 800 degree C. In addition, when more Yb (5% percents) is added, the thermal conductivity is still much higher (30% percents) than the sample without Yb doping, as shown in Fig.4 .6.1.1C. The Seebeck coefficient of the nano sample with 5% Yb doping is dramatically different than that of the sample without Yb doping, and has two

inflection points in the temperature up to 900 degree C while there is no inflection point for resistivity at any temperature. This may relate to the fact that Yb is insoluble in SiGe alloy, thus it could be possible that only nano Yb crystals exist in the sample instead of Yb atoms uniformly distributed in the SiGe matrix.

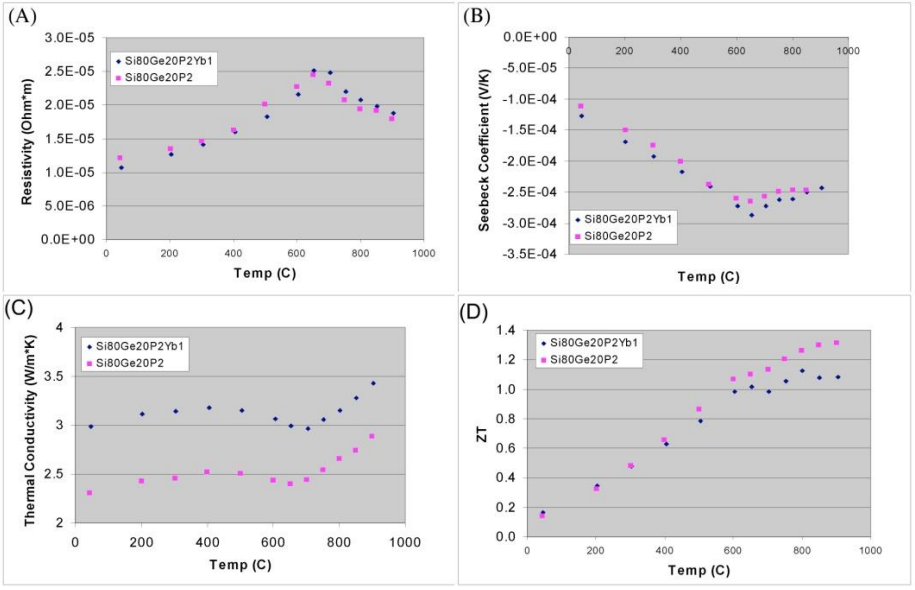


**Fig. 4.6.1.1** Thermoelectric properties of nano $Si_{80}Ge_{20}P_2$ samples with or without 1% Yb addition.

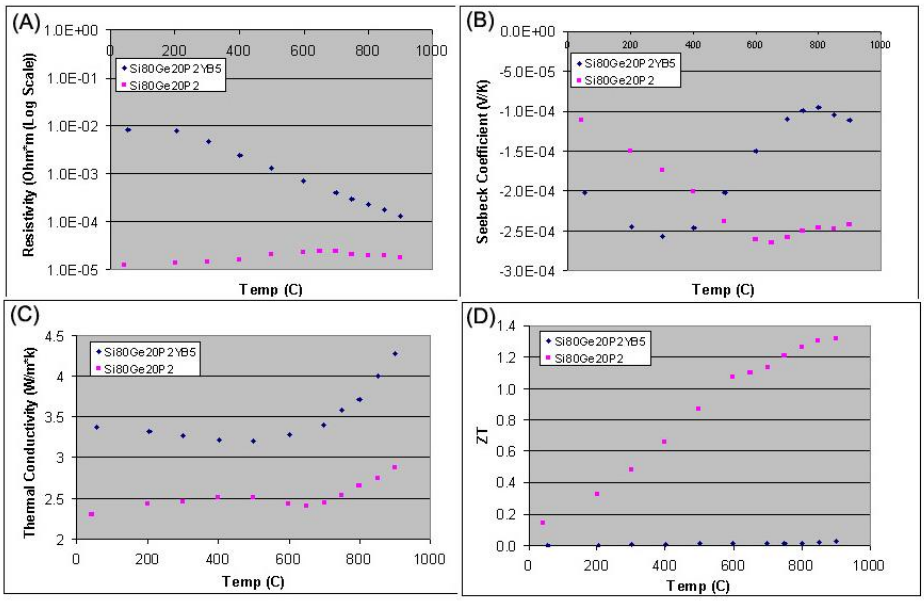


**Fig. 4.6.1.2.** Thermoelectric properties of nano $Si_{80}Ge_{20}P_2$ samples with or without 5% Yb addition.

### 4.6.2. Nanostructured SiGe Samples with Bismuth Addition

The second inclusion element we tried was Bismuth (Bi) since Bi is in the same column as P and has a large atomic weight. Fig. 4.6.2.1 shows the measurement results. The resistivity of the sample with Bi addition shows a higher value than that of the sample without Bi addition, with a larger difference at higher temperature. It is easily understood that Bi atoms steadily evaporate out of the sample during the measurement since there is no solubility of Bi in SiGe and the melting point for Bi is 217 degree C. In fact, the density of the as-measured sample dropped from 3.02 g/cm$^3$ to 2.91, indicating the Bi evaporation. Those evaporated Bi generates voids inside the atoms, which scatter carriers, leading to a lower carrier mobility and electrical conductivity. In regard to the Seebeck coefficient, there

is no difference between the samples with or without Bi addition, which further confirmed that the higher resistivity of Bi-doped sample mainly comes from the impurity scattering of those voids left over by evaporated Bi atoms. The thermal conductivity of Bi-doped samples is about 20% lower than that of the sample without Bi addition, mainly coming from impurity scattering of those voids as well. However, overall, the sample with Bi addition shows a slightly lower ZT value in the higher temperature region because of too much loss of electrical conductivity.

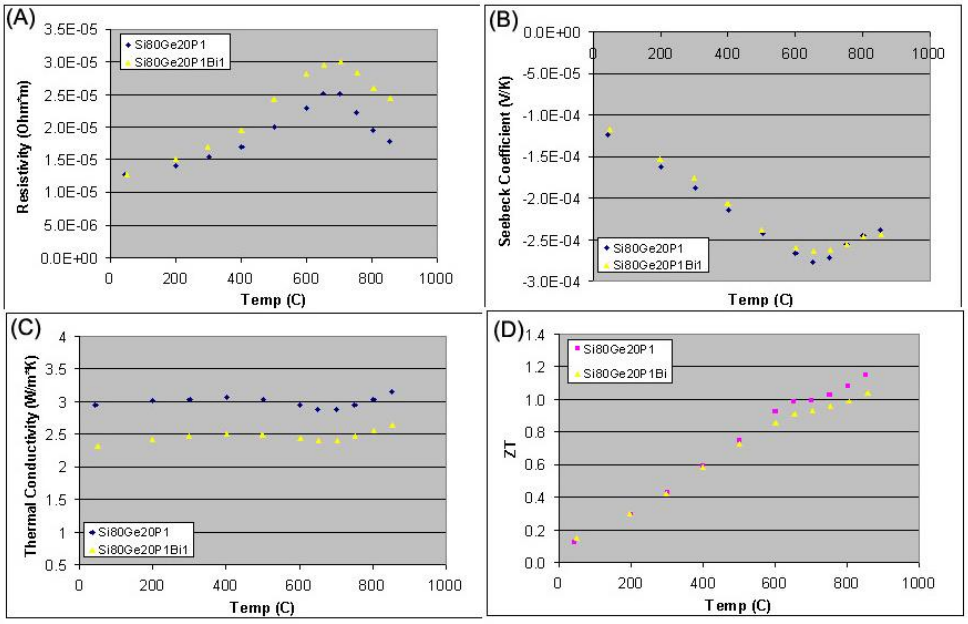


**Fig. 4.6.2.1.** Thermoelectric properties of nano $Si_{80}Ge_{20}P_1$ samples with or without 1% Bi addition.

### 4.6.3. Nanostructured SiGe Samples with Tellurium Addition

Tellurium (Te) chunk was added to our sample as well, and the results are shown in the following figures. Fig. 4.6.3.1 shows the thermoelectric properties of a $Si_{80}Ge_{20}P_1Te_1$

nanostructured sample. Compared to the sample without Te addition, the resistivity of the Te-doped sample is quite different from the sample without Te addition. It dopped progressively as the temperature was increased from room temperature up to 900 degrees C. However, the Seebeck coefficient is almost the same for both samples with or without the Te addition, which indicates that the high resistivity of the Te-doped sample is mainly due to the lower mobility from impurity scattering of Te. Regarding thermal conductivity, although the diffusivity of the sample with Te addition is lower than that of the sample without Te addition, the thermal conductivity of both samples are almost the same because of the high density of Te-doped sample. Overall, the ZT of Te doped $Si_{80}Ge_{20}P_1$ sample shows 15% percent lower value.

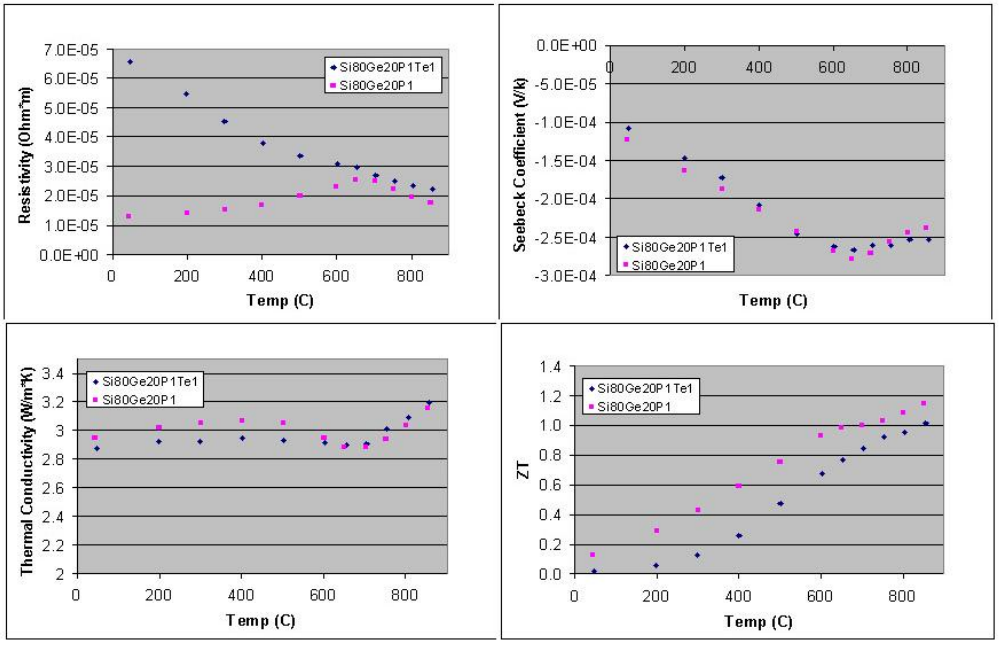


**Fig. 4.6.3.1.** Thermoelectric properties of nano $Si_{80}Ge_{20}P_1$ samples with or without 1% Te addition.

Fig. 4.6.3.2 shows the measurement results for the $Si_{80}Ge_{20}P_2Te_1$ sample. Unlike the Te doping on $Si_{80}Ge_{20}P_1$ composition, the resistivity of $Si_{80}Ge_{20}P_2Te_1$ has the same trend as that of $Si_{80}Ge_{20}P_2$, but higher values in the high temperature region. Seebeck coefficients for both samples are almost the same. Similar to the Te doped $Si_{80}Ge_{20}P_1$ sample, thermal conductivities of all the $Si_{80}Ge_{20}P_2$ samples with or without Te addition have almost same value. Overall, the ZT value of $Si_{80}Ge_{20}P_2Te_1$ sample is about 20% lower than that of $Si_{80}Ge_{20}P_2$ sample at high temperature region, mainly due to higher resistivity.

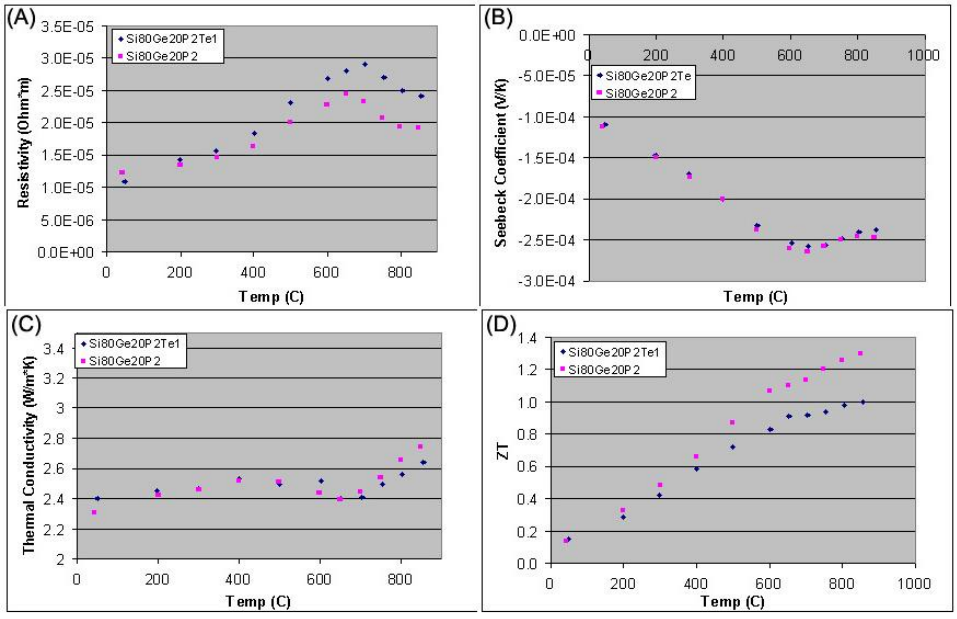


**Fig. 4.6.3.2.** Thermoelectric properties of nano $Si_{80}Ge_{20}P_2$ samples with or without 1% Te addition.

### 4.6.4. Nanostructured SiGe Samples with Sulfur Addition

Since voids can be created by evaporating out a material with a low melting point, 1% S was added into $Si_{80}Ge_{20}P_1$ alloy in order to obtain lower thermal conductivity without too much loss of electrical conductivity. The results are shown in Fig. 4.6.4.1. As we expected, the thermal conductivity of S-doped sample is about 20% lower than that of the sample without S doping. However, the resistivity is almost the same for both types of samples at temperatures up to 700 degree C, and a litter bit higher (15%) for S-doped sample at temperatures higher than 700 degree C, due to the impurity scattering of the voids from evaporated S atoms. In addition, it looks as if both samples have a similar carrier concentration since they have almost the same Seebeck coefficient at all temperatures and have 1% P doping. In conclusion, the S-doped sample show a slightly higher ZT value (2%) than that of the samples without S doping. However, some voids are visible to the naked eye, thus it could be possible to obtain even higher ZT if we could have nano voids inside the SiGe matrix.

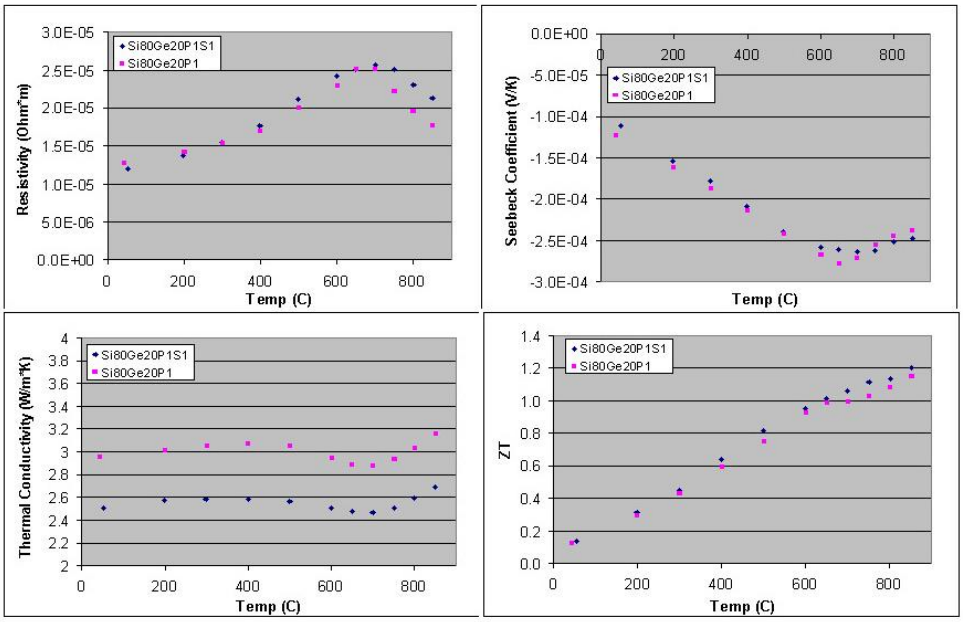


**Fig. 4.6.4.1.** Thermoelectric properties of nano $Si_{80}Ge_{20}P_1$ samples with or without 1% S addition.

### 4.6.5. Nanostructured SiGe Samples with $Mn_3P_2$ Addition

MnSi and the higher manganese silicides are of some interest to thermoelectrics recently since they have ZT values of up to 0.8-0.9 in the middle temperature range (500-700 degrees C) because of their low thermal conductivity [20]. Thus, $Mn_3P_2$ chunks were added into $Si_{80}Ge_{20}$ material as a doping material. During hot press, $Mn_3P_2$ decomposes into Mn and P because of the high operational temperature (1030 degree C). The decomposed P will act as doping agent, and we hope that Mn atoms will further reduce the thermal conductivity. Fig. 4.6.5.1 shows the results. As we expected, $Mn_3P_2$ did decompose into Mn and P since the resistivity of $Mn_3P_2$-doped sample has similar values at temperatures up to 700 degrees C. In

the high temperature region, the resistivity of $Mn_3P_2$ doped sample is much higher than that of the sample without $Mn_3P_2$ addition, which may be due to the impurity scattering of Mn atoms. However, despite its low electrical conductivity, the thermal conductivity of $Mn_3P_2$-doped sample is much higher than that of the sample without $Mn_3P_2$ addition, leading to lower ZT value at all temperatures.

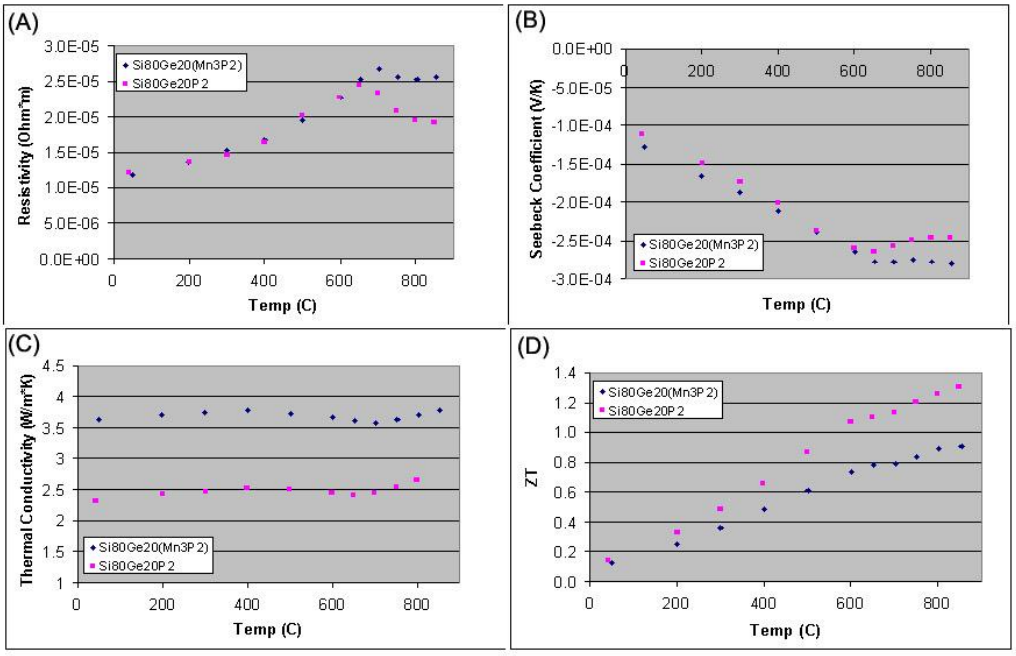


**Fig. 4.6.5.1.** Thermoelectric properties of nano $Si_{80}Ge_{20}P_2$ samples with or without 1% $Mn_3P_2$ addition.

## 4.7. Summary

In summary, numerous nanostructured n-type SiGe alloy samples were made to optimize the thermoelectric properties. This includes Germanium ratio, Phosphorus composition (carrier concentration), and press condition. Results showed that the $Si_{80}Ge_{20}P_2$ sample with 25 hrs ball milling time has the highest ZT value, mainly due to its lower thermal conductivity. In addition, several samples of $Si_{80}Ge_{20}P_2$ with different densities, controlled by press temperature, were made. The results suggested that pores on the order of nanometers may help to reduce thermal conductivity further while maintaining the power factor, leading to a higher ZT value.

As suggested by the literature, GaP powder was added to our best sample in an attempt to further enhance the power factor. However, the results showed that GaP-doped $Si_{80}Ge_{20}P_2$ nano samples actually have lower electrical conductivity than the one without GaP doping. Instead of increasing the carrier concentration, hall measurement showed lower carrier concentration for GaP-doped nano sample. The carrier mobility of GaP-doped sample is also much lower than that without GaP doping. This is quite different from GaP-doped SiGe alloy samples with the grains of micron size. This maybe because Extra P in nanostructured samples may suppress the dissolving of P atoms into SiGe matrix even with the help of GaP.

Finally, different inclusions, such as, Yb, Bi, Te, S, $Mn_3P_2$, were added into SiGe nano samples in order to enhance the scattering of the phonons with short-wavelength.

However, the thermal conductivity of the inclusion samples was higher than that of the samples without these additions. A possible explanation is that these materials are insolvable in SiGe systems, making it difficult to form nano inclusions, which are important for the scattering of short-wavelength phonons. For the samples with Bi and S doping, the thermal conductivity was lower than that of the sample without Bi or S addition, mainly due to the pore's formation from the evaporation of those materials. Overall, the samples with S addition shows a slightly higher ZT value than that of the samples without S addition. However, some pores are in the rage of millimeter, thus it could be possible to obtain even higher ZT if we could have nano pores inside the SiGe matrix.

## 4.8. Reference


1. J. M. Borrego, IEEE *Transactions on Electron Devices*, **2**, 364 (1962).
2. G. S. Nolas, J. Sharp, H. J. Goldsmid, *Thermoelectrics basic principles and new materials developements,* published by Springer (2001).
3. B. A. Cook, B. J. Beaudry, J. L. Harringa, and W. J. Barnet, *Proceedings of the Twenty-fourth Intersociety Energy Conversion Engineering Conference,* Washington, **2**, 693 (1989).
4. H. Stohr, W. Klemm, *Z. Anorg. Allgem. Chem.* **241**, 305 (1954).
5. A. J. Minnich, M. S. Dresselhaus, Z. F. Ren, and G. Chen, *Energy Environ. Sci.,* London, (2009).
6. P. Ashburn, *Electrical and Electronics Engineering, John Wiley&Sons, Ltd.* (1993).
7. *CRC Handbook of Thermoelectrics,* edited by D. M. Rowe, CRC Press, Boca Raton, FL, (1995).
8. D. Z. Wang, "thermoelectric-figure-of-merit enhancement of Si-Ge through nanocomposite concept", Ph.D thesis, Boston College, (2007).
9. R. Venkatasubramanian, E. Siivola, T. Colpitts, and B. O'Quinn, "*Thin-film Thermoelectric Devices with High Room-temperature Figures of Merit*," Nature, 413, 597 (2001).

10. H. Y. Lee, *et al.*, "Thermoelectric Properties of SiGe Nano-composites", International Conference on Thermoelectrics, (2005).

11. N. Savvides, and H. J. Goldsmid, *J. Phys. C: Solid St. Phys.*, **13**, 4657 (1980).

12. O. Mara, C. William, *Handbook of Semiconductor Silicon Technology*, 349 (1990).

13. S. H. Han, B. A. Cook, "Study of enhanced phosphorus activity in n-type $Si_{80}Ge_{20}$ as a function of the doping process", MRS Fall Meeting, (1996).

14. N. Savvides, and D. M. Rowe, J. Phys. D: Appl. Phys., **14**, 723 (1981).

15. J. W. Vandersande, C. Wood, and S. L. Draper, *Mat. Soc. Symp. Proc.*, **97**, 347 (1988).

16. R. G. Master, J. F. Nakahara, " Reecent investigation of SiGe/GaP thermoelectric materials at TTC and GE", *Energy Conversion Engineering Conference*, Washington, (1989).

17. O. Yamashita, J. Appl. Phys. **89**, 624 (2001).

18. E. Kasper, "Properties of Strained and Relaxed Silicon Germanium", *INSPEC*, London (1995).

19. J. Yang, *et.al.* "Unprecedented High Solubility of Yb in n-type Skutterudites $Yb_xCo_4Sb_{12}$ and Their Enhanced Thermoelectric Properties", Submitted to P. R. L. (2009).

20. T. Takeuchi, *Philosophical Magazine*, **86**, 1037 (2006).

# Chapter 5

# Synthesis of Freestanding ZnO Nanowires and its Photolumine--scence or Electroluminescence Properties

The semiconductor ZnO has gained substantial interest in the research community in part because of its large exciton binding energy. This could lead to lasing action based on exciton recombination even above room temperature. In past decades, many research studies on the photoluminescence of ZnO film or ZnO nanowires film were carried out. Here, we demonstrated the application of the light-emitting diode based on single ZnO nanowire.

## 5.1. Introduction

There has been a great deal of interest in ZnO semiconductor materials, as seen from a surge of a relevant number of publications [1-4]. The interest in ZnO is fueled and fanned by its prospects in optoelectronics applications due to its direct wide band gap. In particular, the high exciton binding energy (60 mev), which is 2.4 times that of the room-temperature thermal energy (25 mev), causes an enhancement of the radioactive transition rate in the ultraviolet part of the spectrum [5-6]. Although, some optoelectronic applications of ZnO overlap with that of GaN, another wide-gap semiconductor which is widely used for the production of green, blue-ultraviolet, and white light-emitting devices, ZnO has some

advantages over GaN. These include the availability of fairly high-quality ZnO bulk, leading to a lower cost for ZnO-base devices.

The ZnO bulk crystals have been grown by a number of methods, as has been reviewed recently [7]. High-quality ZnO films can be grown at relatively low temperatures. In addition, ZnO has high energy radiation stability and amenability to wet chemical etching. Several experiments confirmed that ZnO is very resistive to high-energy radiation, making it a very suitable candidate for space applications. ZnO is easily etched in all acids and alkalis, which provides an opportunity for fabrication of small-size devices.

ZnO also has some niche applications other than in the photoluminescence field, such as fabrication of transparent thin-film transistors. In this case, the protective covering preventing light exposure is eliminated since ZnO-based transistors are insensitive to visible light [8-10]. Also up to two charge carriers can be introduced by heavily doping into ZnO. By controlling the doping level, electrical properties can be changed from an insulator through n-type semiconductor to a metal while maintaining optical transparency. This makes it useful for transparent electrodes in flat-panel displays and solar cells. ZnO is also a promising candidate for spintronics applications, for example, Fe-, Co-, or Ni-alloyed ZnO was predicted to stabilize high-curie-temperature ferromagnetism [11-12].

Recently, one-dimensional semiconductor nanowires and nanorods have attracted increasing attention due to their physical properties arising from quantum confinement (such as electronic quantum transport and enhanced radioactive recombination of carriers).

Nanowires have promising potential in extensive applications and are the fundamental building blocks for fabricating short-wavelength nanolasers, field-effect transistors, and field emitters [13-14]. Many nanowires made of materials such as Si, C, InP, GaAs, GaN, ZnO, and $In_2O_3$ have been fabricated for different applications using a catalyst-assisted vapor-liquid-solid growth method. Among these materials ZnO is considered to be the most promising due to its large exciton binding energy, high electromechanical coupling constant, and resistivity to harsh environment. Therefore, one dimensional ZnO structures attracted so much attention and a large number of publications have appeared lately reporting synthesis of these nanowires and their electrical or optical properties [15-16].

One advantage for 1D structure is that the electronic and optical properties can be tailored by altering the growth conditions, as well as by appropriate post-growth treatment [17]. For example, as-made ZnO nanowires grown on sapphire substrates exhibit a prominent near-bad-edge UV peak, whereas nanowires grown on graphite flakes exhibit broad sub-bandgap luminescence [17]. In addition, a single ZnO nanowire can form a resonant cavity with two naturally faceted hexagonal end faces acting as reflecting mirrors [5]. On the device fabrication side, a powerful hybrid approach for engineering the optical properties of ZnO by means of lithographic techniques has been reported recently. However, electrical injection into nanowires still remains a technical challenge. In this chapter, we address this issue by constructing the first Zinc oxide single-nanowire light-emitting diode.

## 5.2. Growth mechanisms of ZnO nanowires.

All vapor phase growths of ZnO nanostructures follow two basic growth mechanisms. One is called the vapor liquid solid (VLS) method. Another is the vapor solid (VS) method [18-19].

The schematic of vapor solid liquid (VLS) growth mechanism is shown in Fig. 5.2.1, which was first developed for the growth of single crystal silicon whiskers by Wager and Ellis [20]. In this method, a catalyst is required to assist the growth of nanowires (usually gold for ZnO nanowire growth). When the furnace temperature reaches the eutectic point of the catalyst and ZnO, the source material in its gas phase is absorbed into a liquid droplet of a catalyst to form a liquid alloy. The liquid alloy clusters serve as a preferential site for absorption and supersaturation of the reactant to form 1D nanowires. The growth occurs as long as the catalyst remains liquid and there is a continuous source of the gas supply. Observation of the catalyst particles at the end of the nanostructures is generally considered to be proof of VLS growth.

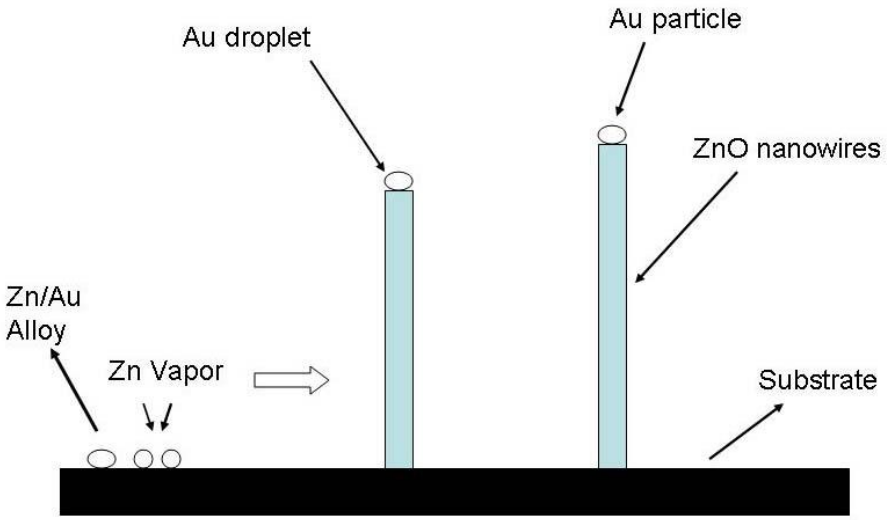


**Fig. 5.2.1.** Schematic diagram of VLS mechanism.

Fig. 5.2.2 shows a schematic of VS growth of ZnO nanowires without the presence of any catalyst. In the high temperature region, Zn and Zn sub-oxides droplets produced during the vapor phase reaction, then those droplets will be carried to low temperature via inherent gas. In the low temperature region (lower than the boiling point of Zn), Zn-sub-oxide vapor condenses and acts as ideal nuclei of ZnO nanowires. In our project, VL growth mechanism is chosen since there is no catalyst particle at the end of the nanowires. Moreover, the ZnO nanowires from VL growth mechanism have very long length of around 7 micros, which is very important for the device fabrication afterward.

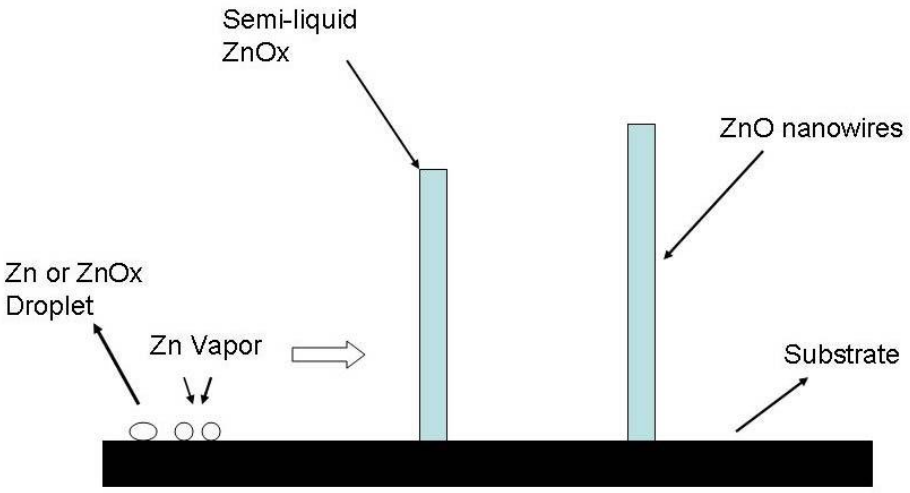


**Fig. 5.2.2.** Schematic diagram of VS growth mechanism.

## 5.3. Experimental Set Up

ZnO itself has a very high melting temperature, and is consequently hard to evaporate. At the same time, Zn evaporates easily because of its low melting point. But neither of them are good candidates as a source material since Zn powder has a tendency to evaporate very quickly, leading to very short growth time. In our experiments, we adopted a mixture of ZnO and graphite powder as source materials to assist in the evaporation of ZnO powder. The experimental set-up is illustrated in Fig. 5.3.1.

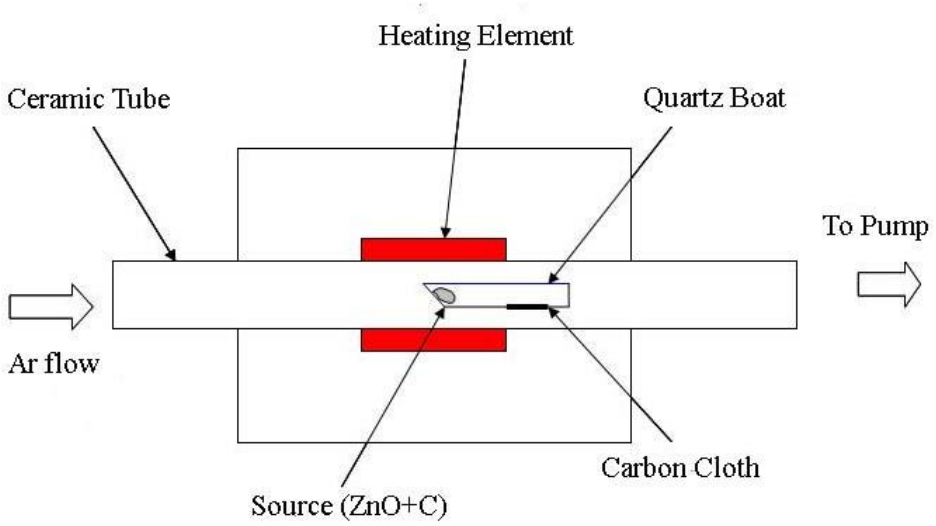


**Fig. 5.3.1.** Schematic diagram of high temperature furnace.

In a real experiment, a mixture of ZnO and graphite was heated at high temperature to reduce ZnO powder to Zn and ZnO suboxide vapor. Carbon cloth were spread uniformly about 2-3 cm from the source along the direction of gas flow (Argon with the flow rate of 50 sccm) in order to collect the nanowires. Normally the boat was positioned in such a way that the source was at 1000-1100 degree C and the carbon cloth at 650-750 degree C. After 30 minutes' growth, the color of carbon cloth changed from black to grey, indicating ZnO nanowires formation onto carbon cloth. The entire boat was covered by a quartz plate to prevent ZnO vapor loss while a small opening was left to facilitate airflow into the assembly. And the whole assembly is inserted into the edge area of the high-temperature horizontal ceramic tube furnace where a steep temperature curve is established. To maintain the desired pressure of around 2 Torr, one end of the furnace tube was attached to a rotary vacuum pump while the other end was close by a silicone stopper connected to an adjustable needle valve.

The source temperature was ramped from room temperature to around 1100 degree C at a rate of about 50 degree C/min. Vapor produced from the heated source condensed and deposited on the carbon cloth because of the temperature gradient and the pumping direction. The structures of as-made ZnO nanowires were analyzed by XRD, SEM, and TEM.

The advantage of using carbon cloth instead of conventional Si substrate is to achieve ZnO nanowires in freestanding form simply by oxidizing the as-made sample at a high temperature. At a temperature higher than 500 degree C, the carbon cloth is oxidized while no chemical change occurs to ZnO since ZnO has a very high (1975 degree C) melting point. In addition, the density of the nanowires can be controlled by the position of carbon cloth related to source area. Here the temperature of about 750 degree C is applied to collect low density nanowires in order to easily spread them in single wires without tangling. When the wire density is high, they tend to tangle with each other, which make it very difficult to build a single nanowire LED device.

## 5.4. Characterization of ZnO Nanowires on Carbon Cloth

Our group has used a carbon cloth as substrate on which ZnO nanowires were grown because of its superior field emission characteristic [21]. Carbon cloth is a woven textile material consisting of carbon fibers oriented in two directions. It was found that ZnO

nanostructures grow easily on a micro-curvature surface. And for samples located at different temperature zones, the morphologies and wires densities are different. When the carbon cloth temperature is around 750 degrees C, a low density ZnO nanowires is observed. If the sample temperature is around 700 degrees C, a high density of ZnO nanowires appears. When the temperature is below a certain point (650 degrees C), only nanoclusters or very short nanorods are observed.

Scanning electron microscopy (SEM) usually produces images down to a length scale on the order of 10 nm and provides valuable information regarding the structural arrangement, and spatial distribution of an assembly of nano-scale features on a substrate. In addition, it can be used to study the morphological and geometrical features of nanostructures. Fig. 5.4.1 shows the SEM images of the ZnO nanowires on carbon cloth under different temperature zones.

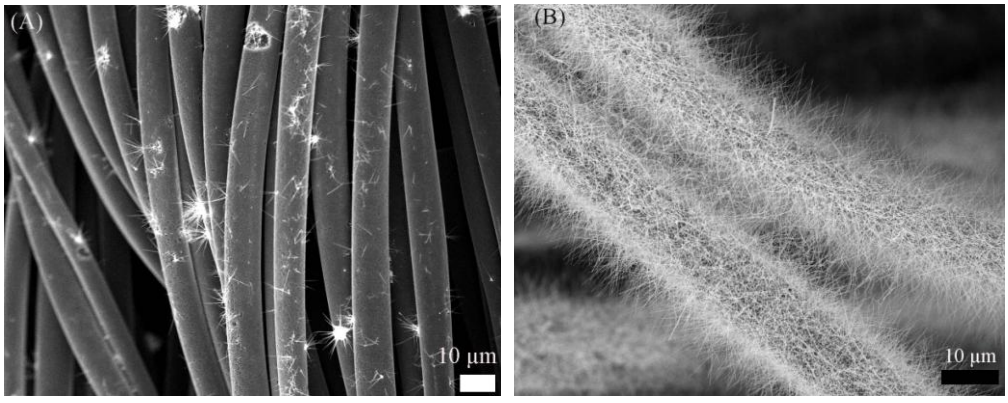

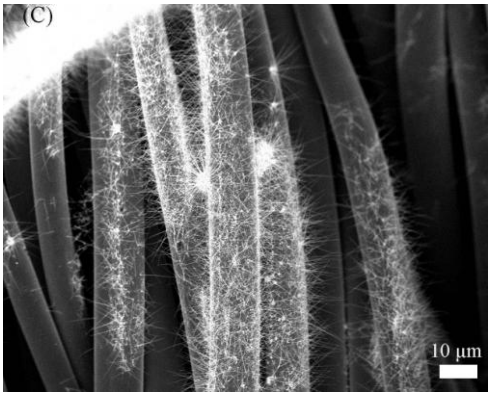


**Fig. 5.4.1.** SEM pictures of ZnO nanowires grown on carbon cloth under different temperature zones of 650 degree C (A), 700 degree C (B), and 750 degree C (C).

The crystallinity of the as-made ZnO nanowires grown on carbon cloth was studied by using XRD, as shown in Fig. 5.4.2. The spectrum matches well the bulk ZnO with wurizite hexagonal structure, with unit cell constants of a= 3.248 A and c= 5.206 A.

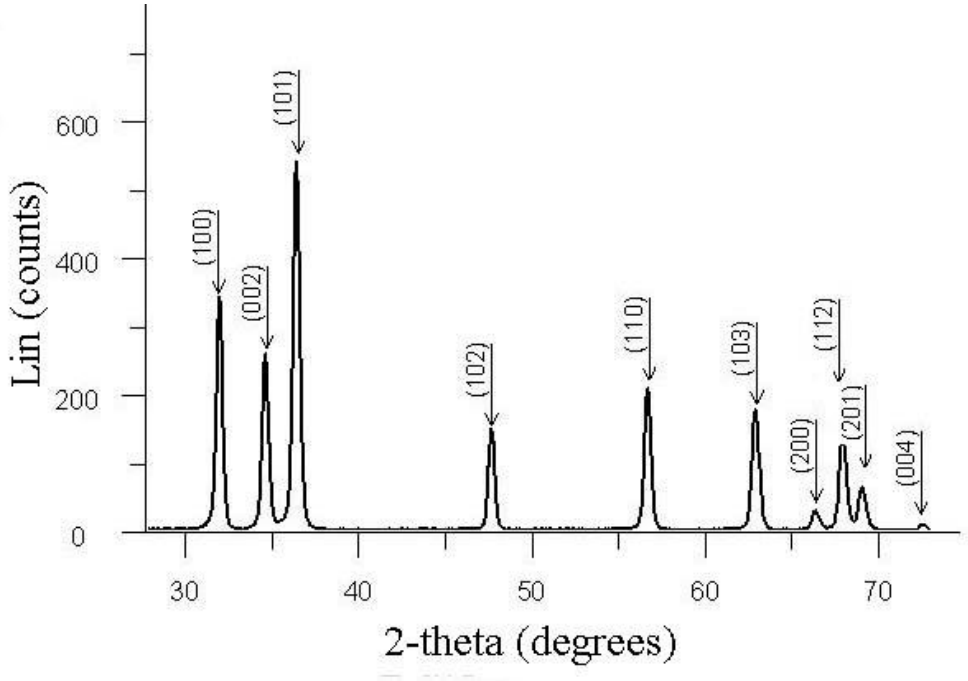


**Fig. 5.4.2.** XRD spectrum of ZnO nanowires.

TEM and HRTEM are powerful imaging tools that are used to study nanostructure at the atomic level. They usually provide more detailed images of the geometrical features than those seen in SEM images. TEM micrographs also yield information regarding the crystal structure, crystal quantity, and crystal orientation. Fig. 5.4.3 shows the TEM images of the ZnO nanowires grown on carbon cloth. From Fig. 5.2.3A, it is clear that the diameters of ZnO nanowires are about 40-50 nm with the length of about 10 microns. Selected area electron diffraction pattern (SAED) indicates that as grown ZnO nanowires have a very good crystallinity. In the TEM image with high magnification, it was found that the wire growth direction is (001), which is c-axis of ZnO materials.

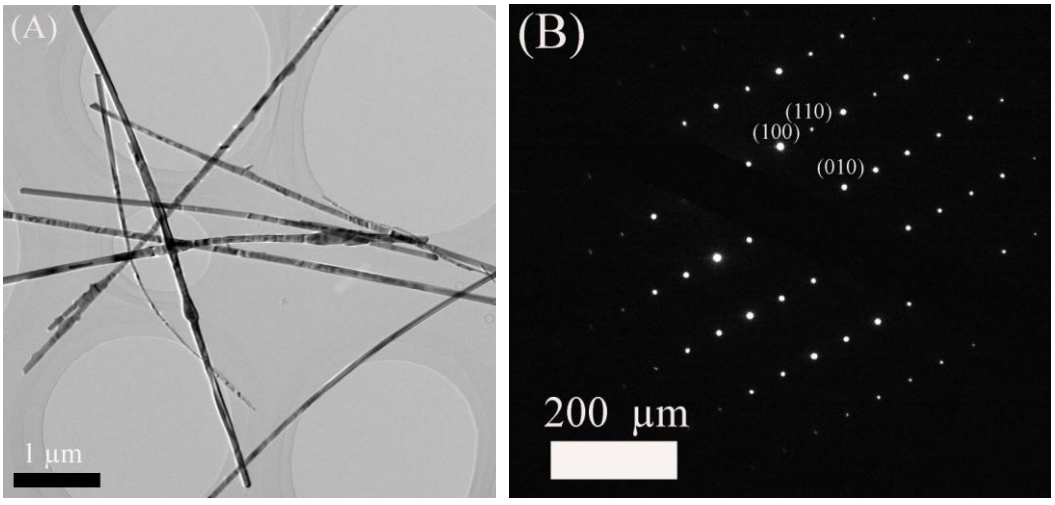

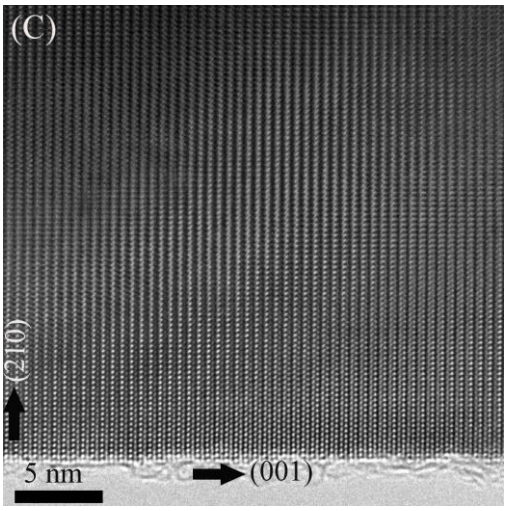


**Fig. 5.4.3.** TEM images of ZnO nanowires on carbon cloth, A) low magnification, B) SAED pattern, C) high magnification.

## 5.5. LED Device Fabrication

ZnO nanowires dissolved in ethanol are first dispersed (Fig. 5.5.1a) on a heavily P-doped Si substrate (resistivity is 0.001 ohm-cm), followed by a spin-coating of a thin film (~120 nm) of PMMA on the substrate [22]. The key step involves patterning the PMMA in a manner such that it is cross-linked on both sides of the nanowire while leaving the top unexposed (Fig. 5.5.1b and Fig. 5.5.1c). This is achieved with the electron beam of a dual beam Focused Ion Beam (FIB) system, which allows direct imaging and writing. After e-beam writing, unexposed PMMA is removed with acetone. Fig. 5.5.2a is a scanning electron microscope (SEM) image of a patterned ZnO nanowire before metal deposition,. In the image, it clearly shows the gap opened in the cross-linked PMMA revealing the top surface of the

nanowire. Following an $O_2$ plasma cleaning step to remove any organic residue on the exposed surface of the nanowire, Ti/Au is deposited with an electron beam evaporator to form the top contact (Fig. 5.5.1d). A total of over ten devices were fabricated and tested. It was noticed that in the majority of the devices a rapid thermal annealing step (~300 ˚C for 60 s in He-H) increased the electroluminescence intensity and the forward current.

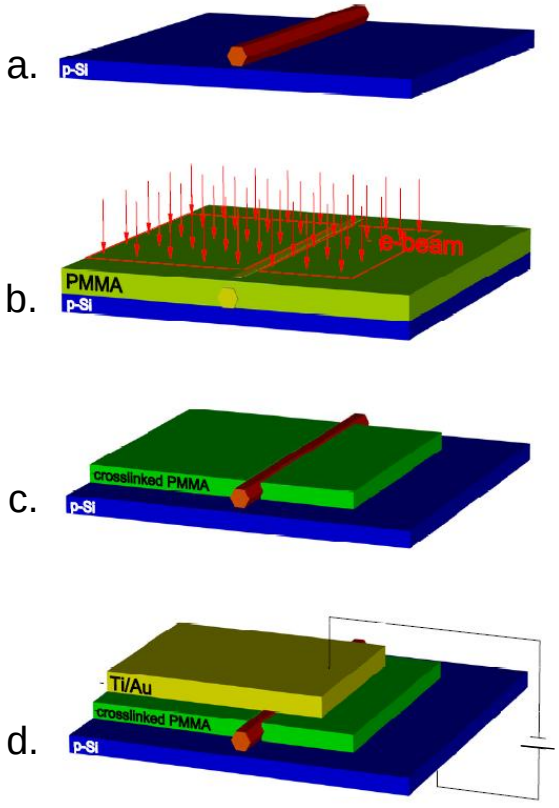


**Fig. 5.5.1.** Schematic description of the procedure to fabricate a metallic contact on the top surface of a single nanowire. (a) ZnO nanowires are dispersed on a p-Si substrate. (b) A PMMA thin film (~120 nm) is spin-coated on the substrate. The wire is located and imaged

with the SEM of the Focused Ion Beam (FIB) system. The pattern for e-beam exposure is defined directly on the SEM image (red outline), and subsequently written. The dose is ~10 $mC/cm^2$, which is 15 to 20 times higher than the dose for positive exposure. (c) The unexposed and partially exposed PMMA is removed by immersing the sample in acetone for 5 minutes, then washed with IPA and dry cleaned with nitrogen air. Because PMMA shrinks when crosslinked, the thickness of the film reduces to ~90nm. (d) Ti/Au is deposited with an electron beam evaporator to form the top metallization.

Fig. 5.5.2b and 2c show SEM images of a typical finished device (device A). An opening in the center of the top metallic contact was included to maximize the amount of light emission collected. Fig. 5.5.2d shows an optical image of the device when the substrate is biased positively with respect to the metallic contact (forward bias). The figure clearly shows that light emission originates from scattered spots along the nanowire (one in the middle opening, one at the left end of the nanowire, and two less intense spots on the right side, as indicated by the arrows) and not uniformly from the entire body. This observation emphasizes the waveguiding properties of these nanowires. We believe that the emission from the center opening and the two spots on the right side of the nanowire are due to local nonuniformities.

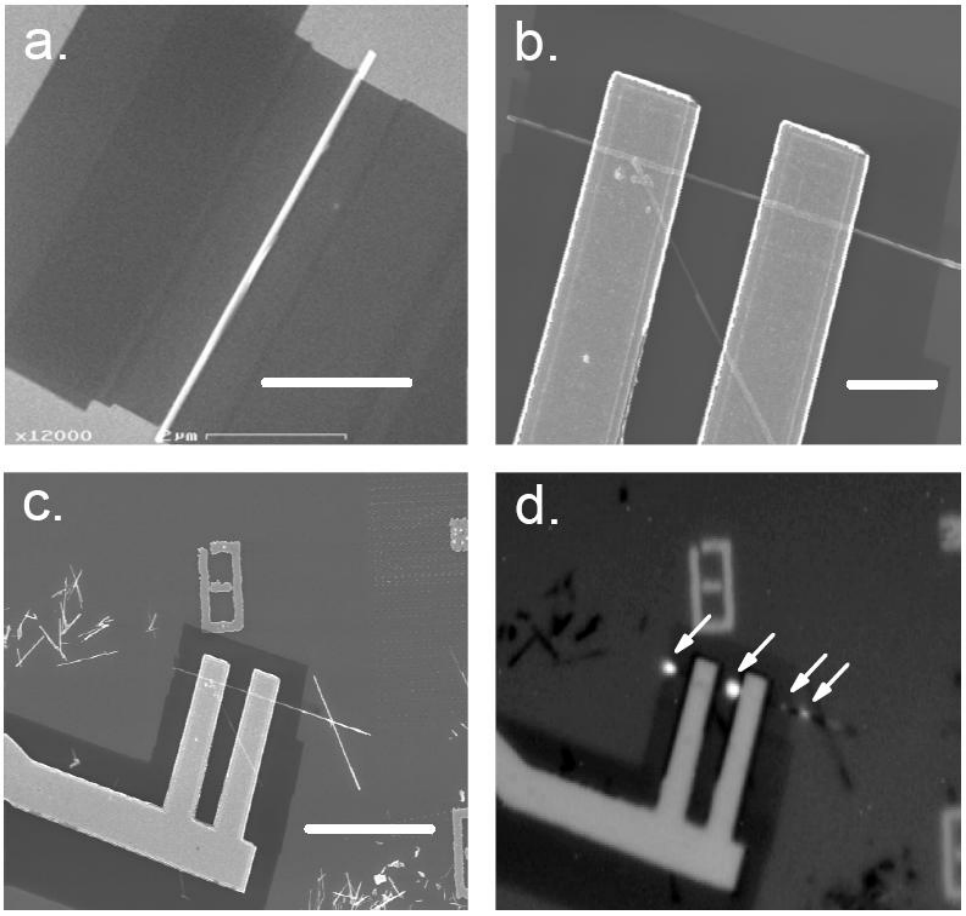


**Fig. 5.5.2.** SEM and optical images of a single ZnO nanowire LED. (a) SEM image of a finished pattern on a ZnO nanowire before metal deposition (schematic shown in Figure 1(c)). Light gray: p-Si substrate; dark: crosslinked PMMA; white: ZnO nanowire. Scale bar is 2 μm. (b) SEM image of a typical finished device. The top Ti/Au metallic contact (~50 nm Ti and ~120 nm Au) intercepts the wire with two prongs, leaving three open sections for light emission. The exposed top nanowire surface is visible. Scale bar is 2 μm. (c) Zoomed-out SEM image of (b). The less dark area is the p-Si substrate, and darkest one is the crosslinked PMMA.

A stray ZnO nanowire intercepts the device on the right side. Scale bar is 10 μm. (d) Grayscale optical image of the device when a positive voltage (7V) is applied to the substrate electrode with respect to the metallic contact. The light emission comes from four spots, indicated by the arrows.

## 5.6. Luminescence Properties of ZnO Nanowires Light-emitting Diode

The single-nanowire electroluminescence (EL) spectrum was measured using a setup consisting of a microscope objective and a single-grating spectrometer equipped with a thermoelectrically cooled CCD camera. The photoluminescence (PL) spectrum was measured with the same setup and a He-Cd laser (325 nm) as the excitation source.

Figure 5.6.1a shows the current versus voltage (*I*-*V*) characteristics for the same device shown in Fig. 5.5.2b-d (device A), as well as two other devices (device B and device C). The three devices show reasonable PN junction characteristics. Fig. 5.6.1b shows the measured light intensity versus current for three devices. These two figures illustrate the reasonable reproducibility of the electrical and optical characteristics within the nanowire variability. The observed differences could be due to the different contact areas. In particular, the measured luminescence will be strongly dependent on the out-coupling efficiency, which will be affected by nonuniformities along the nanowire length (Fig. 5.5.2). No significant variations in the current and emission intensity under a constant bias voltage were observed after several hours of continuous operation.

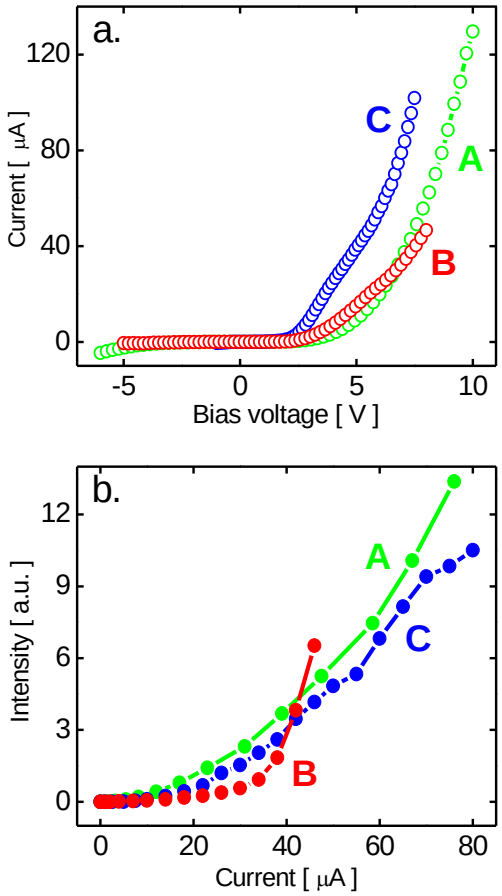


**Fig. 5.6.1.** Current versus voltage and light intensity versus current characteristics of three finished devices. Device A corresponds to the device shown in Fig.5.5.2b-d. The approximate contact areas are ~0.27 $\mu m^2$, ~0.16 $\mu m^2$, and ~0.15 $\mu m^2$ for devices A, B, and C, respectively. Left: Current versus voltage characteristics at room temperature, in ambient air. Positive voltage corresponds to the voltage of the p-Si substrate with respect to the top metallic contact. (b) Light intensity versus current for forward bias. Light was collected directly above the sample using a microscope objective with 50x magnification.

Figure 5.6.2 shows the EL for the devices shown in Fig.5.5.2 (devices A-C), at different voltages, as well as the PL of an isolated nanowire. The PL is centered at 556 nm, and has a full-width at half-maximum (FWHM) of ~170 nm. The EL of all devices displays the same general features, extending from 350 nm to beyond 850 nm. The weak luminescence centered at ~380 nm has been attributed to excitonic recombination [23-24]. The broad sub-bandgap emission in the PL and EL spectra is believed to be due to defects and surface states [17]. The spectral characteristics are reproducible across different devices, and all three devices exhibit an enhancement of the short wavelength emission with increasing bias voltage.

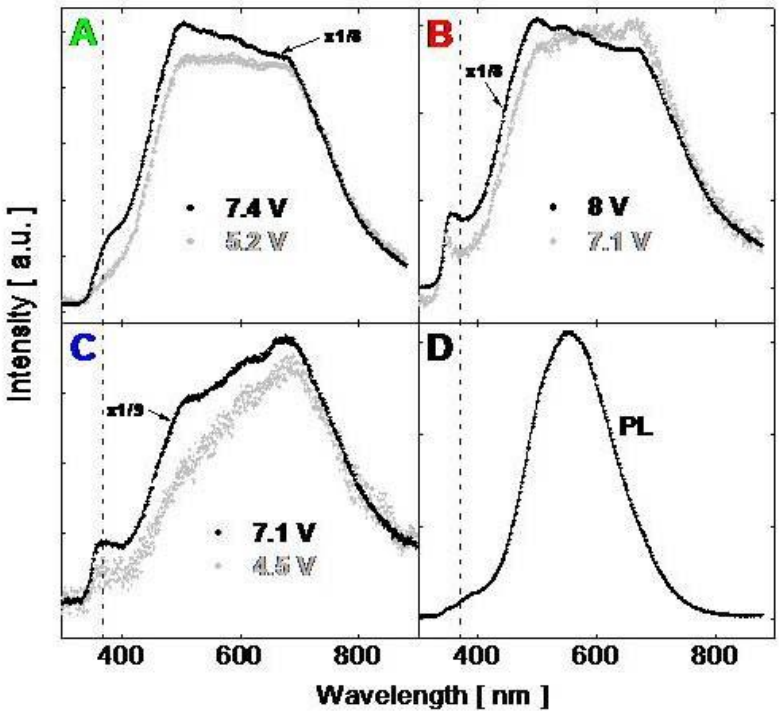


**Fig. 5.6.2.** Photoluminescence and electroluminescence spectra of ZnO nanowires at room temperature, in ambient air. (A), (B), and (C) show the electroluminescence of three different

devices (corresponding to devices A, B, and C, respectively, as shown in Fig.5.5.2) as a function of bias voltage. The dashed line indicates the wavelength of band edge emission in bulk ZnO (370 nm). (A) Electroluminescence spectrum of the single ZnO nanowire LED device (device A) shown in Figure 2(b-d) at 5.2 V (gray), and 7.4 V (black). (B) Electroluminescence spectrum of a single ZnO nanowire LED (device B) at 7.1 V (gray) and 8 V (black). (C) Electroluminescence spectrum of a single ZnO nanowire LED (device C) at 4.5 V (gray) and 7.1 V (black). (D) Photoluminescence of a typical single ZnO nanowire.

This device structure can be identified as a p-i-n junction. Oxygen molecules adsorb on the nanowire surface as negatively charged ions by capturing free electrons from the n-type ZnO. With a nanowire radius comparable with the depletion layer thickness, the nanostructures can be assumed to be completely depleted. The dominant mechanism of electroluminescence is the recombination of electron and holes injected from the top metallic contact and the bottom substrate electrode, respectively. We should note, however, that under reverse bias we also have observed light emission, which we believe is due to impact ionization.

We should also note that from the staggered band lineup at the ZnO/Si interface that was inferred in recent work this configuration is not ideal for an optimum device. The valence band discontinuity of ~2.5 ev strongly suppresses hole injection from the silicon substrate [25]. This problem could be addressed by using alternate substrate with band gaps

larger than that of ZnO, such as p-type GaN.

## 5.7. Persistent Photoconductivity in ZnO Nanowires

Under ultraviolet (UV) illumination, the induced photocurrents are observed to persist both in air and in vacuum. Once the photoresponse reaches a maximum, it typically persists forever, as long as good vacuum is maintained. However, when vacuum is broken and air is in, the photocurrent quickly decays into the typical air photoresponse values. The above phenomenon and its possible explanation will be described in this section.

Figure 5.7.1 shows the current-voltage (I-V) characteristics in the dark. An SEM image of a typical ZnO nanowire device is shown in the inset of Fig. 5.7.1. Devices were prepared on an oxidized Si wafer with 1 micron thick silicon dioxide insulating layer. Electrical contacts were defined by electron-beam lithography and lift-off. They consisted of 5 nm of titanium and 50 nm of gold deposited sequentially using thermal evaporation. To achieve ohmic contact, the device was then thermally treated for 10 min at 400 degree C. the linear I-V relations indicate the desired ohmic behavior of the contacts. The observed dark currents were low both in air and in vacuum.

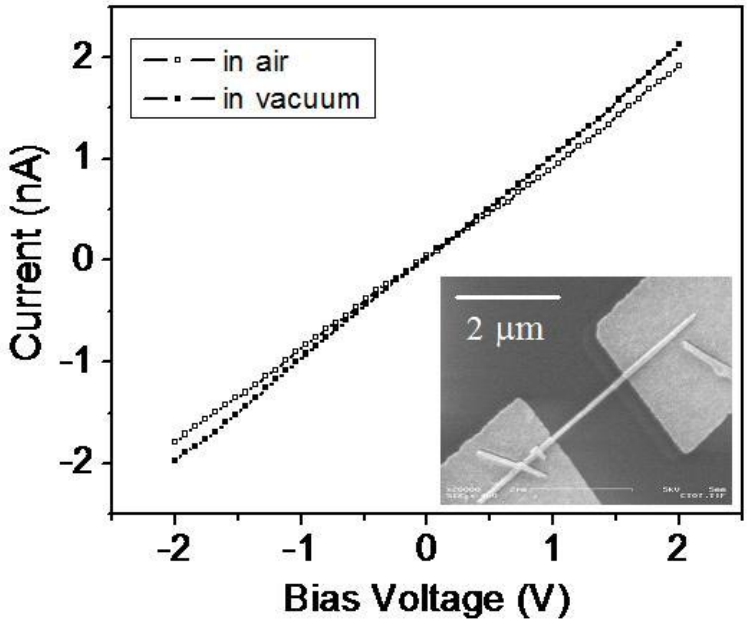


**Fig. 5.7.1.** Dark current versus voltage of the ZnO nanowire in air (unfilled squares) and in vacuum (filled squares).

Photoconductivity measurements were carried out in an optical cryostat at room temperature. A Mercury lamp was used as the UV light source. A band-pass filter was used to obtain monochromatic radiation with a wavelength of around 313 nm. The measurements were performed in air and in vacuum of less than $10^{-5}$ torr.

Figure 5.7.2 shows the time response of the photocurrent in air. Upon exposure to UV light, the photocurrent rises rapidly, reaching a steady state value in several minutes. However, when the UV light is turned off, the current decays slowly after a short rapid decay. The overall decay is not exponential, and slows down further over time. The current takes over 10 hours to fully restore its original dark value. The inset in Fig. 5.7.2 shows the photocurrent as a function of light intensity. The current is clearly not a linear function of the

intensity.

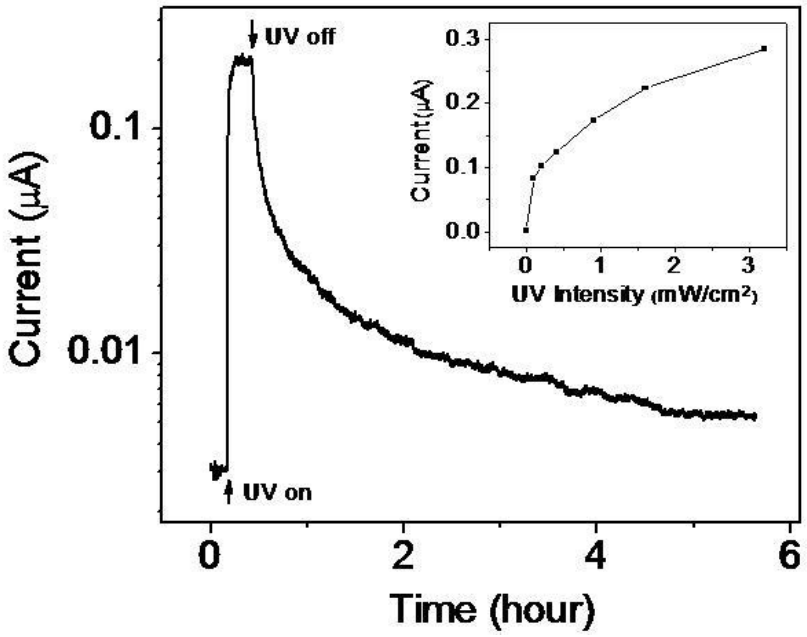


**Fig. 5.7.2.** Transient current of the ZnO nanowire in air. The intensity of the 313 nm UV light is ~1.3 mW/cm$^2$. Inset: steady state photocurrent versus light intensity in air. The bias voltage is 0.3 V.

Figure 5.7.3 shows the time response of the photocurrent in vacuum under three different UV intensities. Its response is quite different from that of the photocurrent in air. Upon exposure to UV illumination, a short rapid photocurrent increase is observed for all the three intensities, followed by a slow increase. Steady state is not reached even after 5 hours, although the photocurrents are already 20 times as large as those observed in air for the same intensity. When the light is turned off, the current shows almost no decay and it only drops about 5% in the first day.

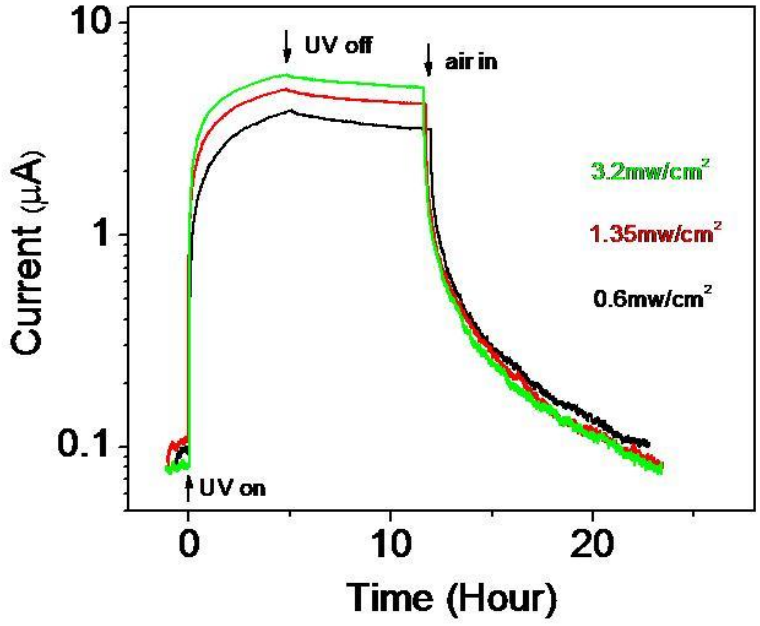


**Fig. 5.7.3.** Photoconductivity of single ZnO nanowire at three UV intensities in vacuum.

In order to find the origin of this persistent photoconductivity in ZnO nanowires, we first calculated the photocurrent contribution from photogeneration of electron-hole pairs. To obtain an upper limit for this contribution, we assumed that the incident light is fully absorbed. The electron density due to photo-excited free excitons (~ 60 meV binding energy) can be estimated as $n \approx \frac{p\tau}{Dh\nu}$, where $p$ is the UV light intensity, ν the frequency of the UV photon, $D$ the diameter of a nanowire, and $\tau$ the lifetime. Since ZnO is a direct bandgap semiconductor, the lifetime of photogenerated electron-hole pairs is shorter than 1 ns [15, 26]. For a UV intensity of 3.2 mW/cm$^2$, the generated electron density is about $7\times10^{11}$/cm$^3$, and the corresponding photocurrent at 0.3 V bias voltage is about $10^{-7}$ nA, assuming the electron mobility is ~ 20 cm$^2$/vs [27-28]. This contribution is six orders of magnitude less than the dark current we observed, therefore it is safe to neglect the electron-hole-pair component of

the photocurrent in our case of weak illumination.

Although there is no doping agent added during ZnO nanowire growth. It typically shows n-type conductivity, which is commonly thought to be related to oxygen vacancy, as described in references [29]. Oxygen vacancies are more likely to stay close to wire surfaces, serving as electron traps. However, in our case, those electrons traps are most likely related to oxygen adsorption.

The electron trapping associated with oxygen adsorption may be described by:

$$O_2(g) + e^- \rightarrow O_2^-(ad)$$

where $O_2(g)$ and $O_2^-(ad)$ indicate oxygen in its free and adsorbed states, respectively. The reverse process, desorption of oxygen from the surface requires a hole,

$$h^+ + O_2^-(ad) \rightarrow O_2(g)$$

The trapping of electrons gives the surface a negative charge, and creates a non-conducting depletion layer under the surface. A decrease of this depletion layer under UV illumination is the main source of the photoconductivity of Zn nanowires. In the dark, reducing the oxygen pressure has only a minor effect on the adsorbed oxygen. It is confirmed that there is only a minor change in conduction between operation in vacuum and in air prior to UV exposure, as shown in Fig. 5.7.1.

Figure 5.7.4 illustrates the depletion layer profile in a ZnO nanowire in the dark and under illumination. Compared to the photoconductivity of the ZnO nanowires under UV illumination, a rather low dark conductivity is observed. Therefore, we assume the wire is

almost entirely depleted in the dark. The observed green subbandgap luminescence, centered at ~2.15 eV, has been previously suggested to pin the surface Fermi level at ~1.15 eV below the conduction band (band bending potential, $\Phi$, is ~ 1.15 eV) [30]. Once UV light is turned on, oxygen molecules are desorbed, as photo-excited holes become available, leading to reduced surface potential $\Phi$ and a decrease of the corresponding depletion width until a steady state is reached. The change of surface potential and the corresponding depletion width are determined by means of interplay between oxygen adsorption and the net electron generation rate which is a function of the UV light intensity. However, because of the relatively high oxygen partial pressure in air, total elimination of the depletion region would require an extremely high illumination intensity. The maximum photocurrent should correspond to the native electron density *n*. This explains why the saturation value of the photocurrent increases sublinearly with the illumination intensity (Fig. 5.7.2).

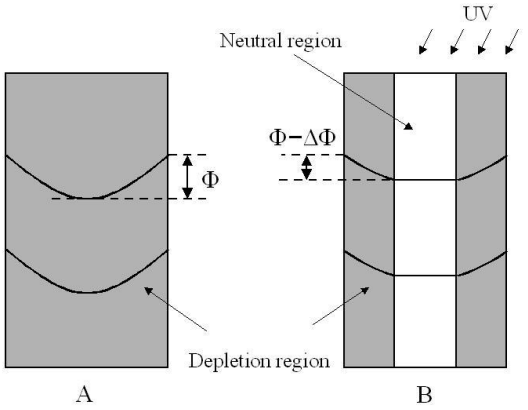


**Fig. 5.7.4.** Schematic of the depletion region in the dark (A) and under UV illumination (B).

As the illumination is turned off, adsorbed oxygen molecules trap electrons,

gradually bending the bands, raising a potential barrier and an internal field. This makes it difficult for further electrons to get trapped at the surface, thereby gradually making it more and more difficult for more oxygen to get adsorbed and so forth. This explains the persistence behavior of the photocurrent as observed in Fig. 5.7.2, and 5.7.3.

In air, the discharging of the oxygen-related surface states and the resulting desorption of oxygen, as well as the shrinking of the depletion layer, requires about 2-3 minutes, as indicated by the time the photocurrent takes to reach its steady state value. In vacuum, the steady state is different, as there is no equilibrium between desorbed and adsorbed oxygen. In vacuum, all oxygen is rapidly pumped, no oxygen can be re-adsorbed. As a result, the fully desorbed surface oxygen totally eliminates the contribution of the adsorbed oxygen to the depletion and band-bending. Indeed, an initial rapid rise of the photoconductivity in vacuum is observed (0.5 μA in the first 2-3 minutes). However, this rapid response is followed by a slower rise, as indicated in Fig. 5.7.3. We believed this slow response is related to tightly bound oxygen, or lattice oxygen in the wires.

The idea of lattice oxygen desorption in ZnO has already been suggested in order to explain the photoconductivity in whiskers [29]. Shapira and Lichtman (1974) used mass spectrometry and Auger electron spectroscopy to identify the species desorbed from ZnO, under the same conditions as in the form of $CO_2$. They suggested that surface hydrocarbons, commonly present on many solid surfaces, work in conjunction with the incident photo energy to release oxygen from the ZnO lattice, in a process that may be reversed by exposure

to gaseous oxygen in the dark [31]. And indeed, Carbothermal reduction is commonly used to enhance the decomposition of ZnO powders [32]. Therefore, it is likely that if a UV light is turned on, carbon may still enhance oxide decomposition. When carbon is present on the surface, a "carbo-optical" reaction may be responsible for the slow oxygen desorption process. Once those free electrons released from desorbed oxygen, as well as from the Zn-rich surface layer, they should remain free as long as the ZnO nanowire is maintained in good vacuum, leading to a persistent photoconductivity. The minor decay of photo current is most likely related to residual oxygen in our vacuum.

Finally, we shall now support our previous assumption of nearly total depletion. The maximum photocurrent we were able to achieve was $I_{ph} = S \cdot e\mu \cdot \Delta n \cdot E \approx 0.5\ \mu A$, where $S \approx 5 \cdot 10^{-11}\ cm^2$ is the typical cross-sectional area of our nanowires, *e* is the electron charge, and *E=1700 V/cm* the electric field. Assuming the mobility, $\mu \approx 20\ cm^2/Vs$, we get a carrier density of $\Delta n = 2 \cdot 10^{18}\ cm^{-3}$. The critical wire diameter $d_{crit}$, below which a nanowire will be completely depleted by surface states is

$$d_{crit} = \sqrt{\frac{16\varepsilon\varepsilon_0\phi}{e\Delta n}}$$

where ε is the dielectric constant of ZnO (ε ~8.5). Assuming $\phi = 1.15\ eV$, as previously suggested, we obtain $d_{crit} \approx 70nm$. This value is about the actual diameter of the ZnO nanowire. The nanowire is then likely to be totally depleted, in agreement with its low dark conductivity.

In conclusion, we studied photoconductivity of ZnO nanowires in vacuum and in air. Traps associated with adsorbed oxygen seem to deplete the ZnO material near its surface. In the case of nanowires, this is often a total depletion of the wire by the surface states. This oxygen-related depletion may be partially undone by exposure to UV in air, and totally undone by UV exposure in vacuum. UV exposure first removes loosely bound oxygen and in vacuum may further remove lattice oxygen with the assistance of carbon from surface hydrocarbons. This oxygen removal, however, is fully reversible upon exposure to oxygen in the dark, in a process that is somewhat reminiscent of breathing.

## 5.8. Summary

In a conclusion, free standing ZnO nanowires are successfully obtained by using carbon cloth as collecting substrate. The densities of as-grown nanowires can be controlled by the temperature of carbon cloth. New technique was applied to construct the first ZnO single-nanowire LED. The photoluminescence and electroluminescence spectra of typical ZnO nanowire exhibit an enhancement of the short wavelength emission with increasing bias voltage, indicating potential applications of ZnO nanowires in the LED field.

In addition, we studied photoconductivity of ZnO nanowires in vacuum and in air. Traps associated with adsorbed oxygen seem to deplete the ZnO material near its surface. In the case of nanowires, this is often a total depletion of the wire by surface states. This oxygen-related depletion may be partially undone by exposure to UV in air, and totally undone by UV exposure in vacuum. UV exposure first removes loosely bound oxygen and in vacuum may further remove lattice oxygen probably with the assistance of carbon from surface hydrocarbons. This oxygen removal, however, is fully reversible upon exposure to oxygen in the dark, in a process that is somewhat reminiscent of breathing.

## 5.9. References


1. Y. Huang, and C. M. Lieber, *Pure Appl. Chem.* **76**, 2051 (2004).

2. L. Samuelson, C. Thelander, M. T. Björk, M. Borgström, K. Deppert, K. A. Dick, A. E. Hansen, T. Mårtensson, N. Panev, A. I. Persson, W. Seifert, N. Sköld, M. W. Larsson, and L. R. Wallenberg, *Physica E*, **25**, 313 (2004).

3. H. Pettersson, J. Trägårdh, A. I. Persson, L. Landin, D. Hessman, and L. Samuelson, *Nano Lett*. **6**, 229 (2006).

4. C. J. Barrelet, J. M. Bao, M. Loncar, H. G. Park, F. Capasso, and C. M. Lieber, *Nano Lett*. **6**, 11 (2006).

5. H. Kind, H. Yan, B. Mester, M. Law, and P. D. Yang, *Adv. Mater.* **14**, 158 (2002).

6. M. H. Huang, S. Mao, H. Feick, H. Yan, Y. Wu, H. Kind, E. Weber, R. Russo, and P. D.Yang, *Science*, **292**, 1897 (2001).

7. D. C. Look, *Mater. Sci. Eng., B*, **80**, 381 (2001).

8. X. Duan, Y. Huang, R. Agarwal, and C. M. Lieber, *Nature*, **421**, 241 (2003).

9. R. Konenkamp, R. C. Word, and R. C. Schlegel, *Appl. Phys. Lett.,* **85**, 6004 (2004).

10. S. M. Sze, *Physics of Semiconductors Devices*, Wiley-Interscience, 2nd ed. (1981).

11. T. Dietl, H. Ohno, F. Matsukura, J. Cibert, and D. Ferrand, *Science*, **287**, 1019 (2000).

12. S. J. Pearton *et al.,* J. Phys.: Condens. Matter **16**, R209 (2004).

13. Z. W. Pan, Z. R. Dai, and Z. L. Wang, *Science*, **291**, 1947 (2001).

14. Z. L. Wang, *Mater. Today*, **7**, 26 (2004).

15. M. Huang, *et al. Science,* **292**, 1987 (2001).

16. X. Y. Kong, Y. Ding, R. Yang, and Z. L. Wang, *Science*, **303**, 1348 (2004).

17. D. M. Bagnall, Y. F. Chen, Z. Zhu, T. Yao, S. Koyama, M. Y. Shen, T. Goto, *Appl. Phys. Lett.* **1997**, *70*, 2230.

18. J. Y. Lao, J. Y. Huang, D. Z. Wang, Z. F. Ren, *Nano let.,* **3**, 235 (2003).

19. D. Banerjee, J. Y. Lao, D. Z. Wang, J. Y. Huang, D. Steeves, B. Kimball, Z. F. Ren, *Nanotechnology,* **16**, 2028 (2004).

20. R. S. Wanger, W. C. Ellis, *Appl. Phys. Lett.,* **4**, 89 (1964).

21. D. Banerjee, S. H. Jo, and Z. F. Ren, *Advanced Materials,* **16**, 2028 (2004).

22. J. M. Bao, M. A. Zimmler, F. Capasso, X. W. Wang, and Z. F. Ren, *Nano Lett.,* **6**, 1719 (2006).

23. A. C. F. Hoole, M. E. Welland, A. N. Broers, *Semicond. Sci. Technol.* **12**, 1166 (1997).

24. F. Oba, S. R. Nishitani, S. Isotani, H. Adachi, *Appl. Phys. Lett.*, **90**, 824 (2001).

25. S. H. Jo, D. Banerjee, Z. F. Ren, *Appl. Phys. Lett.*, **85**, 1407 (2004).

26. D. C. Reynolds, *et.al*, *J. Appl. Phys.* **88**, 2152 (2000).

27. Q. H. Li, Y. X. Liang, Q. Wan and T. H. Wang, *Appl. Phys. Lett.* **85**, 6389 (2004).

28. D. Y. Fan, D. W. Wang, P. C. Chang, W. Y. Tseng, J. G. Lu., *Appl. Phys. Lett.,* **85**, 5923 (2004).

29. R.J. Collins, D.G. Thomas, *Phys. Rev.* **112**, 388 (1958).

30. K. Vanheusden, W. L. Warren, C. H. Seager, D. R. Tallant and J. A. Voigt, *J. Appl. Phys.* **79**, 7983 (1996).

31. Y. Shapira, S. M. Cox, D. Lichtman., *Surf. Sci.* **54**, 43 (1976).

32. A. N. Korneev, E. S. Vorontso, *Zhurnal Fizicheskoi Khimi*i, **46**, 1551 (1972).

# Summary

In a conclusion, nanostructured n-type SiGe bulk alloy materials with high thermoelectric performance have been successfully obtained through the nano approach. This improved ZT can lead to new applications such as solar thermoelectric energy conversion and waste heat recovery especially in high temperature region.

There are two steps included in the fabrication of SiGe alloy bulk material. First, SiGe alloy nano powder was generated through high energy ball milling of elemental Si and Ge chunks together with phosphorus doping agent. Followed by direct current hot press, fully dense n-SiGe nanocomposite disc sample are obtained. TEM observation confirmed that nano grains with the size of around 20 nm were formed after hot press. These nano grains helped to scatter more phonons, leading to lower lattice thermal conductivity (from 4.5 W/m*K to 2.5 W/m*K at room temperature). Since the sizes of the nano grains are still larger than the electron mean free path of heavily doped SiGe alloy, the power factor of our nanostructured samples is maintained in the same level of commercial RTG samples. Overall, the maximum ZT value of our best sample is about 1.3 at 900 degree C, compared to 0.9 at the same temperature for the reference RTG SiGe materials.

The numerous nanostructured n-type SiGe alloy samples with different Si/Ge ratio, different doping level, different press conditions were successfully pressed in order to determine the optimal conditions of n-SiGe nano thermoelectric material. It was found that

$Si_{80}Ge_{20}P_2$ bulk sample with 25 hrs high energy ball milling shows highest ZT value, mainly due to lower thermal conductivity. In addition, different inclusions were added into SiGe bulk alloy materials to further reduce thermal conductivity. However, the results are not positive because it is difficult to find an appropriate element which is solvable in SiGe matrix. Moreover, for the samples with Bi or S addition, the thermal conductivity is lower than that of the sample without Bi or S addition, mainly due to the pore's formation from the evaporation of those materials. This leaded to little bit higher ZT value for the sample with S addition. And it may be possible to obtain even higher ZT value if we could have nano pores inside SiGe matrix since some pores of S doped SiGe nano samples are in the range of millimeter.

ZnO is a large band-gap semiconductor with several desirable properties for nanowires laser diodes and LEDs. Although, extensive studies have been made on photoluminescence and electroluminescence properties of ZnO nanowires system, many of them are carried out on large numbers of nanowires simultaneously by defining a metallic contact on a thin film of nanowires. In our project, we construct the first ZnO single-nanowire light-emitting diode (LED), which shows the potential of ZnO nanowires as an effective electroluminescence material. The freestanding ZnO nanowires are grown on carbon cloth, the densities of as-grown ZnO nanowires can be controlled by the temperature of the carbon cloth. Also, persistent photoconductivity was found in ZnO nanowires, which is mainly due to a total depletion of the wire by surface states caused by oxygen "breathing".